Scientific Drilling

Reports on Deep Earth Sampling and Monitoring
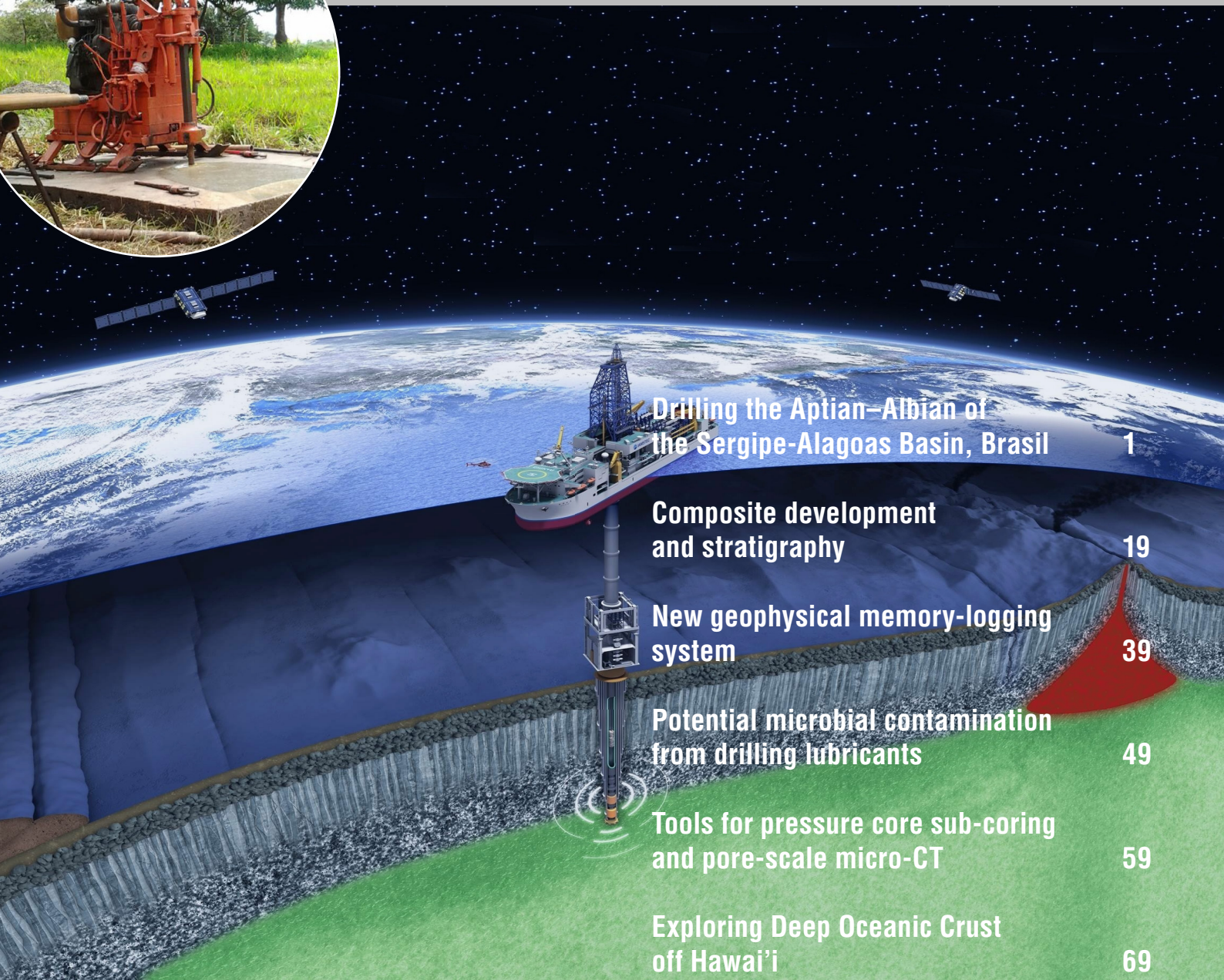
Editorial preface

Dear Reader,

For more than half a century, exploring the oceanic crust-mantle transition by drilling through the seafloor, the Moho, and into the uppermost mantle has been one of the most challenging missions of scientific drilling. A workshop report (**sd-2020-23**) in this volume of your ICDP-IODP program journal SCIENTIFIC DRILLING addresses this exciting moonshot vision, as discussed during an international workshop "Exploring Deep Oceanic Crust of Hawai'i". Scientists and engineers started to develop an IODP proposal to drill a 2.5 km-deep hole into oceanic crust with the drilling vessel Chikyu on the North Arch off Hawai'I as a pilot hole for such an endeavour.

However, such ambitious plans can only be realized with state of the art drilling, sampling, and logging technology and accordingly, this volume highlights new technical developments. A new cable-free, memory downhole logging system was developed, tested and commissioned for deployment by the drill string to minimize operational risks. Results from a comparison study between conventional cable-based downhole logging and this new approach are shown in **sd-2021-1**. The possibility of contaminant DNA introduced by greases and oils from drilling equipment was covered in **sd-2020-22**. Results indicate that contamination from greases and oils, albeit less prevalent compared to contamination during subsequent laboratory handling, was present. Therefore the authors recommend that future studies should monitor potential contamination from lubricants associated with drilling and sampling equipment. The pore space habits of gas hydrate in natural sediment matrices provide essential clues for understanding physical properties of hydrate-bearing strata, yet there are no tools available for direct visualization. **Sd-2020-16** presents a set of new devices, together with a protocol for operation, that enables the manipulation, transfer, cutting, sub-coring, and CT scanning at both, core and pore scale, of pressure cores while maintaining pressure and temperature controls.

Furthermore, two papers from this volume report on paleoclimate archives from southern mid-latitudes in Brazil and New Zealand. Continuous and high-resolution sediment sequences from the Southern Hemisphere are rare; most palaeoclimate reconstructions derive from sediments from the Northern Hemisphere. A drilling campaign in Eastern Brazil successfully collected Lower Cretaceous rocks from the Riachuelo Formation (**sd-2020-13**). Three holes cored the only known preserved carbonate shelf containing the Aptian–Albian transition in Brazil and most likely constitute a complete record of an Aptian–Albian sedimentary section of the South Atlantic Ocean. The results from this onshore drilling campaign will complement the International Ocean Discovery Program Expedition 388 (Equatorial Atlantic Gateway). From several deep maar lakes of the Auckland Volcanic Field of northern New Zealand containing continuous and well-laminated sediment sequences, the Onepoto Basin potentially holds the longest temporal lake sediment record spanning from Marine Isotope Stage 6 to the early Holocene. **Sd-2020-21** describes a paleolake sediment record from Onepoto maar and highlights its potential for the identification of climatically forced environmental changes from the Southern Hemisphere midlatitudes spanning the last two glacial cycles.

Enjoy reading!

Your Editors
Ulrich Harms, Thomas Wiersberg, Jan Behrmann, Tomoaki Morishita, and Will Sager

Cover figure: A conceptual image to drill a deep hole down to the upper mantle through the oceanic crust with the drilling research vessel Chikyu. At a workshop (**sd-2020-23**), a 2.5 km-deep hole on the North Arch off Hawai'i was discussed as a pilot hole for such a survey. Copyright © JAMSTEC.
Insert 1: Drilling rig used to retrieve the core from the Sergipe-Alagoas Basin (**sd-2020-13**).
Insert 2: Aerial photograph of the Onepoto domain study site (**sd-2020-21**). Aerial footage sourced from the LINZ Data Service licensed for reuse under the Creative Commons Attribution 4.0 New Zealand licence.

Contents

Science Reports

Progress Reports

Workshop Reports

Technical Developments

News & Views

Scientific Drilling
Open Access

Science Reports

Drilling the Aptian–Albian of the Sergipe–Alagoas Basin, Brazil: paleobiogeographic and paleoceanographic studies in the South Atlantic

Gerson Fauth[1], Mauro Daniel Rodrigues Bruno[1], Jorge Villegas-Martín[1], Jairo Francisco Savian[2],
Rodrigo do Monte Guerra[1], Guilherme Krahl[1], Francisco Henrique de Oliveira Lima[3],
Oscar Strohschoen Jr.[3], Raquel Gewehr de Mello[2], Fernando Marcanth Lopes[1],
Carolina Gonçalves Leandro[2], and Eduardo da Silva Aguiar[1]

[1]itt Oceaneon – Instituto Tecnológico de Paleoceanografia e Mudanças Climáticas, Unisinos University,
Av. Unisinos, 950, São Leopoldo, RS, 93022-750, Brazil
[2]Departamento de Geologia e Instituto de Geociências, Universidade Federal do Rio Grande do Sul,
Av. Bento Gonçalves, 9500, Porto Alegre, RS, 91501-970, Brazil
[3]PETROBRAS/CENPES/PDEP/BPA, Av. Horácio Macedo, 950, Cidade Universitária,
Ilha do Fundão, Rio de Janeiro, RJ, 21941-915, Brazil

Correspondence: Gerson Fauth (gersonf@unisinos.br)

Abstract. The Aptian–Albian interval is characterized by significant paleoclimatic, paleoceanographic, and paleogeographic changes, which in turn affected the distribution and evolution of marine ecosystems. Despite the importance of such studies, there have been few correlations between Aptian–Albian sections of the Tethys Sea and those of the South Atlantic Ocean. This interval, including the Aptian–Albian transition, is preserved in the deposits of the Riachuelo Formation (Sergipe–Alagoas Basin, Brazil) located in the South Atlantic Ocean; therefore, this location was chosen for drilling four new cores. The goals of this paper are as follows: (1) to explain the drilling operation carried out in the deposits of the Riachuelo Formation and the methods used; (2) to present a brief lithostratigraphic characterization of the holes and the paleomagnetic data of core SER-03; and (3) to describe the high potential of the cores recovered for additional investigation in the future. The lithostratigraphic units of the SER-01 core consist mainly of coarse- to fine-grained sandstone, shales, marls, and mudstones; the SER-02 core was excluded due to low recovery; the SER-03 core is mainly composed of fine-grained sediments (shale, marls, and packstone) and bears some ammonite shells; the lithology of core SER-04 is mainly sandstones. Magnetic susceptibility values (χlf and χhf) and frequency-dependent susceptibility (χfd) data suggest that the section is located within the Cretaceous Normal Superchron. Future studies on these cores integrating micropaleontological, paleoichnological, geochemical, stratigraphic, and paleomagnetic (e.g., relative intensity) data will allow for a better understanding of paleoceanographic and paleogeographic events related to the early evolution of the South Atlantic Ocean and how these events correlate to similar events in Tethyan sections.

1   Introduction

The Early Cretaceous was an important period in the history of the Earth, during which greenhouse conditions prevailed and oceanic gateways gradually opened, allowing for the wide dispersion of marine organisms. The Aptian–Albian interval is characterized by significant paleoclimatic, paleoceanographic, and paleogeographic changes. In addition, important perturbations in the global carbon cycle, the development of large igneous provinces (LIPs) such as the Kerguelen Plateau and Rajmahal Traps, and an increase of the global sea level have also been recognized (e.g., Leckie et al., 2002; Courtillot and Renne, 2003; Haq, 2014). These changes affected the distribution and evolution of marine ecosystems on a worldwide scale (e.g., Dias-Brito, 1987; Riccardi, 1991; Leckie et al., 2002; Browning and Watkins, 2008; Huber and Leckie, 2011; McAnena et al., 2013; Coccioni et al., 2014; Dummann et al., 2020). This interval contains multiple black shale horizons associated with oceanic anoxic events (OAEs) such as the Selli, 113/Jacob, Kilian, Urbino/Paquier, and Leenhardt events (e.g., Erbacher et al., 1999; Leckie et al., 2002; Browning and Watkins, 2008; Jenkyns, 2010; Coccioni et al., 2014; Sabatino et al., 2015, 2018; Bottini and Erba, 2018). In addition, the Aptian–Albian was one of the most recent prolonged periods of stable polarity in the magnetic field of the Earth, the so-called Cretaceous Normal Superchron (CNS), which occurred approximately from 121 to 83 Ma (Helsley and Steiner, 1968; Gee and Kent, 2007; He et al., 2008). Although the CNS has been extensively studied by paleomagnetic methods (e.g., Tarduno, 1990; Tarduno et al., 2001; Cronin et al., 2001; Granot et al., 2007, 2012; Biggin et al., 2008; Linder and Gilder, 2011), there is no consensus on the nature of this event. The global boundary stratotype section and point (GSSP) for the base of the Albian Stage has been formally defined in the Col de Pré-Guittard section, Vocontian Basin (VB), France, which contains deposits from the Tethys Sea (Petrizzo et al., 2016; Kennedy et al., 2017).

Micropaleontological, geochemical, and paleomagnetic studies in the GSSP section, as well as in other important sections, led to the establishment of different criteria for the identification and correlation of the Aptian–Albian boundary around the world (e.g., Herrle et al., 2004; Satolli et al., 2008; Petrizzo et al., 2012; Coccioni et al., 2012, 2014; Sabatino et al., 2015, 2018; Kennedy et al., 2017). For many years, discussions regarding the Aptian–Albian boundary were complicated mainly by the difficulty in correlating different sections of the Tethys Sea using ammonite zonal schemes and planktonic fossil groups (e.g., Kennedy et al., 2000, 2014; Huber and Leckie, 2011; Petrizzo et al., 2012; Ogg et al., 2016). Studies correlating sections of the Tethys Sea with those of other oceans such as the South Atlantic Ocean are very rare.

The Sergipe–Alagoas Basin includes the most complete marine Cretaceous sequences among all South Atlantic basins (Bengtson, 1983; Bengtson et al., 2018). It is known for its economic importance (oil and gas) and the diversity of its Cretaceous fauna and flora. The Lower Cretaceous marine sequence contains well-preserved Aptian–Albian strata in the Riachuelo Formation deposits, which have been extensively investigated using stratigraphic, paleontological, and geochemical data (e.g., Beurlen, 1968; Cainelli et al., 1987; Koutsoukos et al., 1991a, b; Koutsoukos and Bengtson, 1993; Bengtson et al., 2018). Multidisciplinary studies have demonstrated that the marine sequences in the basin represent "type-sections" of the full opening of the Equatorial Atlantic Gateway, considered as the last continental link between South America and Africa (Koutsoukos et al., 1991b; Feijó, 1996; Arai, 2014). In recent years, some studies have used different multiproxies (ichnofossils, microfossils and macrofossils, and sedimentological, geochemical, and paleomagnetic data) to identify the paleoenvironmental and paleoceanographic changes that took place during the Aptian–Albian interval in the South Atlantic (e.g., Koutsoukos et al., 1991a; Carvalho et al., 2016; Valle et al., 2019).

2   Scientific objectives

The most important objectives of drilling the Sergipe–Alagoas Basin are to understand the nature of the marine incursions during the Aptian–Albian interval and if there are possible correlations with paleoclimatic and paleoceanographic events on a global scale during this time interval (Fig. 1). It is also important to assess if a correlation exists between the biotic assemblages of the South Atlantic Ocean and Tethys Sea through a detailed study of a fresh, continuous drill core. These objectives will be pursued through (i) a detailed stratigraphy of the whole sections, (ii) organic and inorganic geochemistry of sedimentary rocks, (iii) study of microfossils, (iv) study of ichnofossils, (v) geochemistry (including stable isotopes) on microfossils, and (vi) paleomagnetic study on oriented core samples. Thus, from these data, we intend to evaluate three important questions about the Aptian–Albian interval, which are outlined in Sects. 2.1–2.3.

2.1   What is the impact of the establishment of oceanic gateways during the Aptian–Albian interval?

This is based on the composition of the microfossil (planktonic foraminifera, calcareous nannofossil, ostracods, palynology, and radiolarians) and macrofossil assemblages in the South Atlantic Ocean. These data could suggest a grade of provincialism or a direct relation with the biota assemblages identified in the Tethys Sea. During the Early Cretaceous, the physiographic barriers of the Rio Grande Rise–Walvis Ridge System (located in the southern region) and the Equatorial Atlantic Gateway (located in its northern region) may have restricted the development of a connection between the proto-South Atlantic and the surrounding oceans (Fig. 1), thereby interfering with the establishment of open marine conditions (e.g., Arthur and Natland, 1979; Rabinowitz and
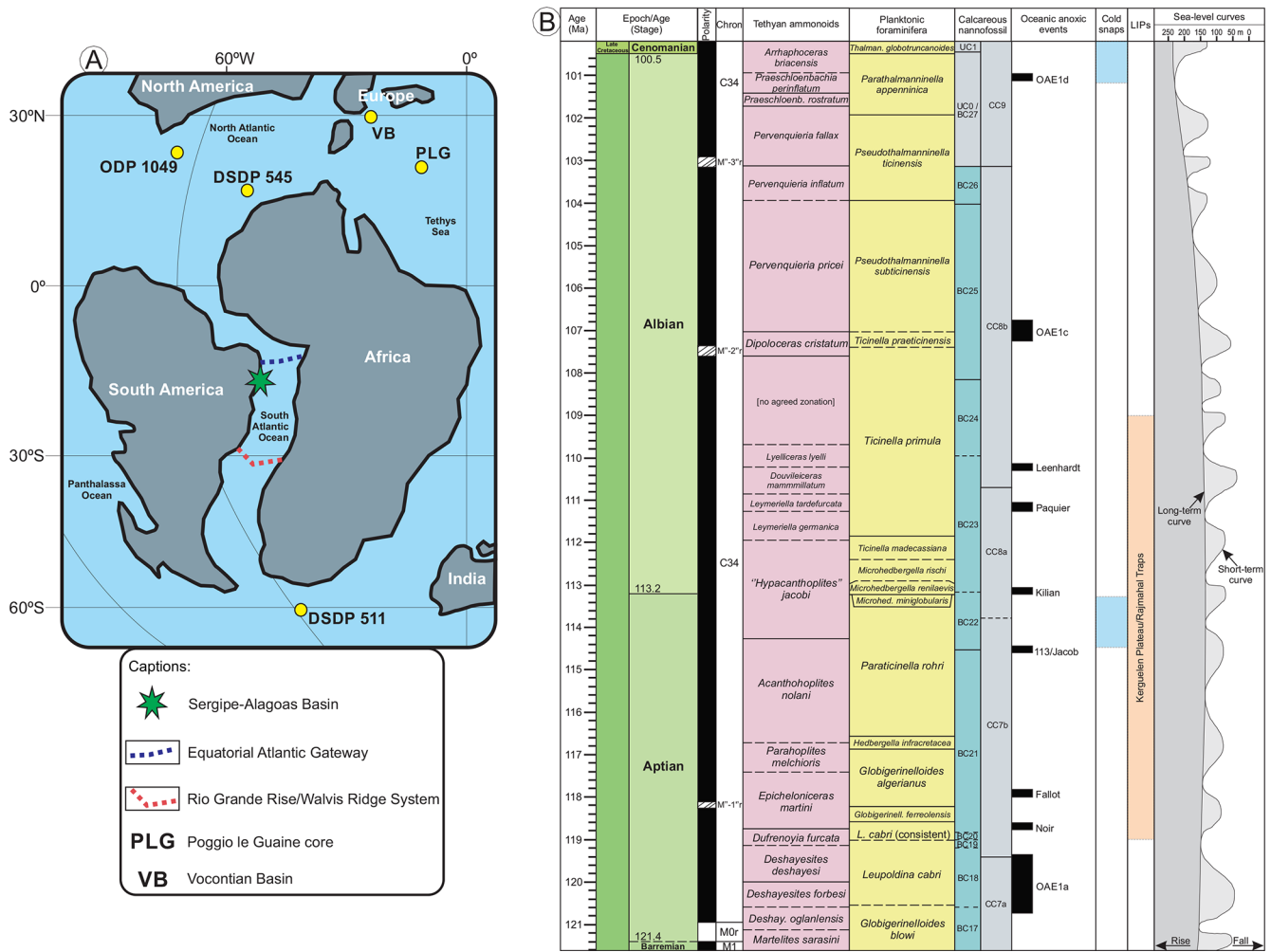
Figure 1. (a) Paleogeographic reconstruction at 112 Ma (modified after Hay et al., 1999) showing the location of the Sergipe–Alagoas Basin, the Equatorial Atlantic Gateway, the Rio Grande Rise–Walvis Ridge System, the Vocontian Basin (VB), the Poggio le Guaine (PLG) core, and the Deep Sea Drilling Project (DSDP) and Ocean Drilling Program (ODP) sites containing the Aptian–Albian boundary. **(b)** Stratigraphic chart of the drilled section with biostratigraphic zones for ammonoids, planktonic foraminifera, and calcareous nannofossil (Gale et al., 2020). For this interval, the main ocean anoxic events (Gale et al., 2020), cold snaps (Hu et al., 2012), large igneous provinces – LIPs (Courtillot and Renne, 2003), and sea level curves (Haq, 2014) are also shown.

Labrecque, 1979; Rand and Mabesoone, 1982; Sibuet et al., 1984; Dias-Brito, 1987; Azevedo, 2004; Torsvik et al., 2009; Arai, 2014; Silva et al., 2020).

During the late Aptian–Albian interval, the surface water connection between the South Atlantic and eastern Tethys (Central Atlantic segment) was fully formed, creating migration routes and physicochemical conditions in the water column that were ideal for the establishment of new marine biota (e.g., Dias-Brito, 1987; Riccardi, 1991; Feijó, 1996; Pérez-Díaz and Eagles, 2017). Fossil assemblages of the South Atlantic have shown a strong affinity to the Tethyan realm (e.g., Dias-Brito, 1987; Colin and Andreu, 1990; Koutsoukos, 1992; Arai, 2014; Silva et al., 2020; Bruno et al., 2020). However, South Atlantic ammonite fossils do not seem to show any affinity to the "Tethyan standard zonation"

(Bengtson et al., 2018). According to Michels et al. (2018), the South Atlantic Aptian–Albian palynologic assemblages show a high degree of provincialism as well, such as the *Dicheiropollis etruscus/Afropollis* Province, which can be observed in other marginal basins around Brazil and Africa and is mainly defined by a gymnosperm paleoflora strongly adapted to warm and dry local climate conditions.

2.2 Do the South Atlantic Ocean deposits record the Aptian–Albian climatic variations?

This is based on the capacity of an integrated analysis of the micropaleontological, ichnological, paleomagnetic, and stratigraphic data from the Riachuelo Formation for important paleoenvironments events in the South Atlantic Ocean

during the Aptian–Albian interval, such as the supposed cooling events (cold snaps) and the two previously recorded evolutionary phases and biota disturbances (Mutterlose et al., 2009; Huber and Leckie, 2011; McAnena et al., 2013). McAnena et al. (2013) expressed that cold snaps during greenhouse conditions could cause perturbations in the marine biotas and biogeochemical cycles. Although greenhouse conditions are widely accepted for the Aptian–Albian interval on a global scale, some studies using geochemical and micropaleontological data indicate that short-lived cooling events (cold snaps) also occurred (e.g., Pirrie et al., 1995, 2004; Erbacher et al., 1999; Clarke and Jenkyns, 1999; Herrle and Mutterlose, 2003; Mutterlose et al., 2009; Huber and Leckie, 2011; Jenkyns et al., 2012; McAnena et al., 2013; Bottini et al., 2015; Herrle et al., 2015).

Studies based on stable oxygen isotope analyses in bulk marine carbonates and belemnites (e.g., Pirrie et al., 1995, 2004; Clarke and Jenkyns, 1999; Föllmi, 2012; Jenkyns et al., 2012), TEX_{86} paleothermometry proxies (e.g., Jenkyns et al., 2012; McAnena et al., 2013; O'Brien et al., 2017), and calcareous nannofossil distributions (Herrle and Mutterlose, 2003; Mutterlose et al., 2009; Herrle et al., 2015; Bottini et al., 2015) have indicate a transition from a prolonged cooling period during the late Aptian to a significantly warmer period during the early Albian. Mutterlose et al. (2009) showed two possible cooling periods at low- and high-latitude sites using nannoplankton data in this interval. Both periods have been identified in the Northern and Southern hemispheres. Finally, Huber et al. (2011) correlated foraminifer biostratigraphy and chemostratigraphic data from the Aptian–Albian interval in the Blake Nose region (Ocean Drilling Program, ODP, sites 1049A and 1049C; Fig. 1), and they suggested cool sea surface temperatures and elevated salinity related to high evaporation rates, demonstrating a limited connection between the sedimentary basins of the proto-Atlantic Ocean (Central Atlantic Seaway or Tethys Sea).

2.3　What are the prospects for a multidisciplinary correlation between the Tethys Sea and the Sergipe–Alagoas Basin?

The idea is to integrate analyses of the micropaleontological, geochemical, and paleomagnetic data obtained from the Riachuelo Formation (Aptian–Albian interval, Sergipe–Alagoas Basin) to identify similar patterns and help clarify the relationship between the South Atlantic Ocean and the Tethys Sea, and to try identify the paleoclimatic, paleoceanographic, and evolutionary/distribution events of the marine biota in the Sergipe–Alagoas Basin as recorded in other Aptian–Albian reference sections (Vocontian Basin; Poggio le Guaine section, PLG; DSDP 511; DSDP 545; ODP 1049) (Fig. 1). In these sections, studies using micropaleontological and geochemical data as well as paleomagnetic signals have provided important information for the identification and characterization of the Aptian–Albian boundary and

some paleoclimatic inferences such as the OAE1b. For example, the first occurrence (FO) of the planktonic foraminifera *Microhedbergella renilaevis*, the last occurrence (LO) of the planktonic foraminifera *Paraticinella rohri* (= *Paraticinella eubejaouensis*), the FO of the calcareous nannofossils *Prediscosphaera columnata* (circular forms) and *Helicolithus trabeculatus*, and the geochemical correlation event (minimum value of 1 % negative δ^{13}C excursion) have demarked the Aptian–Albian boundary in the global boundary stratotype section and point (GSSP) of the Col de Pré-Guittard section from the Marnes Bleues Formation, Vocontian Basin, France (Petrizzo et al., 2016; Kennedy et al., 2017).

In addition, the late Aptian–Albian interval has been characterized by an important time in the evolution of planktonic foraminifera including extinction and speciation events and changes in shell architecture (e.g., Leckie et al., 2002; Huber and Leckie, 2011; Petrizzo et al., 2012). Thus, late Aptian foraminiferal assemblages showed larger, heavily ornamented species, whereas the Albian foraminiferal assemblages comprise small-sized species in different deep-sea sites in the Atlantic and Indian oceans (Huber and Leckie, 2011). Coccioni et al. (2014) used geochemical proxies, planktonic foraminifera, and calcareous nannofossils assemblages to characterize the PLG section that can be used to correlate OAE1b black shale horizons between different marine environments. They also demonstrated that the PLG section can be correlated with the Aptian–Albian deposits of the Vocontian Basin (Fig. 1). Later, Sabatino et al. (2015) developed a chemostratigraphic study for the same sites studied by Coccioni et al. (2014), suggesting an increase in surface water productivity and a reduction in bottom water ventilation during the OAE1b. Other data available for correlation are the presence of an isotopic standard curve (Herrle et al., 2004) and the identification of a geomagnetic event Superchron C34–Cretaceous Quiet Zone (Ogg et al., 2016) for the Aptian–Albian interval.

3　Geological background

The Sergipe–Alagoas Basin was originally described as a single basin by Schaller (1969). However, later stratigraphic revisions divided it into two sub-basins, Sergipe and Alagoas (Feijó, 1994; Campos Neto et al., 2007). It is an elongate continental-margin basin located in northeastern Brazil (9–11°30′ S, 37–35°30′ W), delimited by the Pernambuco–Paraíba Basin to the northeast (Maragogi high) and the Jacuípe Basin (Jacuípe high) to the southwest (Fig. 2). The onshore and offshore sedimentary sequences of the Sergipe–Alagoas Basin reflect distinct tectono-sedimentary phases of the Brazilian Equatorial Continental Margin (BECM), pre-rift, rift, post-rift, and drift. The onshore portion covers an area of approximately 13 000 km^2, whereas its offshore portion is around 40 000 km^2 (Feijó, 1994; Mohriak, 2003; Campos Neto et al., 2007; Antonietto et al., 2015). The structural

framework of the basin is characterized by large tilted fault blocks, forming structural highs and lows (e.g., Mohriak et al., 1998; Kellogg and Mohriak, 2001).

The stratigraphic evolution of the Sergipe–Alagoas Basin is similar to other South Atlantic marginal sedimentary basins, starting with continental sequences that gradually transition to marine ones (e.g., Asmus and Porto, 1972; Berggren and Hollister, 1974; Asmus, 1984; Kellogg and Mohriak, 2001; Milani et al., 2007; Mohriak et al., 2008; Mohriak and Fainstein, 2012). Sedimentary deposits related to the first marine incursions in the South Atlantic are characterized by extensive evaporitic and calcareous sequences developed during the Early Cretaceous, mainly characterized by sedimentary deposits of the Muribeca Formation (e.g., Asmus and Porto, 1972; Milani et al., 2007; Mohriak et al., 2008; Mohriak and Fainstein, 2012). The evolution from restricted marine to open marine conditions in the late Aptian–Albian interval in the Sergipe–Alagoas Basin correspond to the deposition of the sediments of the Riachuelo Formation occurring in the beginning of the drift phase (e.g., Koutsoukos et al., 1991b; Koutsoukos and Bengtson, 1993; Feijó, 1996).

The Riachuelo Formation is a 2800 m thick sedimentary package belonging to the Sergipe Group (Fig. 3). It is mainly characterized by mixed calcareous and siliciclastic sediments deposited in a shelf setting (e.g., Schaller, 1969; Cainelli et al., 1987; Koutsoukos and Bengtson, 1993; Campos Neto et al., 2007). The biota of this unit is mainly composed of ammonites, calcareous nannofossils, foraminifers, ostracods, dinoflagellates, gastropods, bivalves, and echinoids (e.g., Schaller, 1969; Koutsoukos, 1989; Antonietto et al., 2015; Bengtson et al., 2018). The unit was assigned to the Lower Cretaceous (upper Aptian–Albian interval) mainly based on the ammonite biozones (Schaller, 1969; Bengtson et al., 2018). The Riachuelo Formation is subdivided, from base to top, into the Angico, Maruim, and Taquari members (Fig. 3). The deposits of the Angico Member are located mainly on the edge of the basin and in lowered blocks. It represents delta fan deposits composed of mixed calcareous–siliciclastic sediments. The Maruim Member reflects areas that had a lower sedimentary input, and it is composed of grainstones and oolitic/oncolitic packstones deposited on a carbonate shelf. Finally, the Taquari Member represents the deposition of mudstones and wackestones in lagoons on the external shelf and on the slope (e.g., Schaller, 1969; Cainelli et al., 1987; Campos Neto et al., 2007). The goal of our work is the development of a high-resolution multiproxy study (microfossils, macrofossils, ichnofossils, sedimentological, geochemical, and paleomagnetic data) using cores of the Riachuelo Formation to contribute to the understanding of the impact of establishing gateways in the formation of the South Atlantic, the composition of the marine biota in the South Atlantic Ocean, possible correlation with the Tethyan realm biota or determination of endemism for the assemblages, and the recognition of global paleoclimatic and paleoceanographic events in the Sergipe–Alagoas Basin.

4 Drilling operations and sampling

The drilling campaigns (Table 1) started in August 2014 and were successfully completed in April 2015, but investigations on the core were not begun before the year 2019. The drilling was in the onshore section of the Sergipe–Alagoas Basin (Sergipe sub-basin) because the paleoenvironmental changes were more conspicuous in the onshore section of the unit, where the sedimentary deposits contain a diverse, abundant, and well-preserved marine macro- and microfossil assemblage (e.g., Manso and Souza-Lima, 2003; Hessel, 2004; Bengtson et al., 2018). Also, marine microfossils (mainly foraminifera) were present and have been considered a useful tool for understanding the paleoenvironmental evolution of the basin (Koutsoukos, 1989; Antonietto et al., 2015). The drill sites were located mainly in quarries close to outcrops with paleontological studies (Table 1 and Fig. 2) previously assigned to the Riachuelo Formation (Aptian–Albian interval). The drilling rig was oriented mainly perpendicular to the bedding or structural orientation of the lithological units on the ground. Several precautions were taken during the drilling project to preserve the original rock chemistry: (i) only lake water was used as drilling mud; (ii) a clean drilling rig was used, which was repeatedly washed, and the drilling site was kept clean of potential contaminants; and (iii) cores were packed in plastic boxes with polyfoam chips for transportation. The project comprised the drilling of approximately 200 m of rock per site with a minimum of 80 % recovery (Table 1) using a core drilling rig machine with 3.02 m long rods and a 50 mm diameter diamond drill (Fig. 4).

In total, four cores were obtained during the campaigns. Three of them (SER-01, SER-03, and SER-04) were drilled between the towns of Pacatuba, Laranjeiras, and Riachuelo, respectively (Table 1), and SER-02 was drilled in the rural area of the Siriri municipality (Fig. 2). The cores are curated at ambient room temperature at the Instituto Tecnológico de Paleoceanografia e Mudanças Climáticas (itt Oceaneon) of the Unisinos University, Brazil. This study includes the lithostratigraphic results of the SER-01, SER-03, and SER-04 cores as well as the paleomagnetic data of the SER-03 core (Table 1). Technical problems during the drilling operation prevented SER-01 from reaching the desired depth of 200 m, but the 174.7 m depth reached was considered satisfactory (Table 1). After core opening and initial lithologic description and fossil registration, the preliminary results were used to divide the section into distinct units (Fig. 5).

For paleomagnetic analyses, 2 cm thick slices were collected at a resolution of approximately 25 cm throughout core SER-03. Cubic samples (2 cm × 2 cm × 2 cm) were cut from the center of the slices, and the top and bottom of
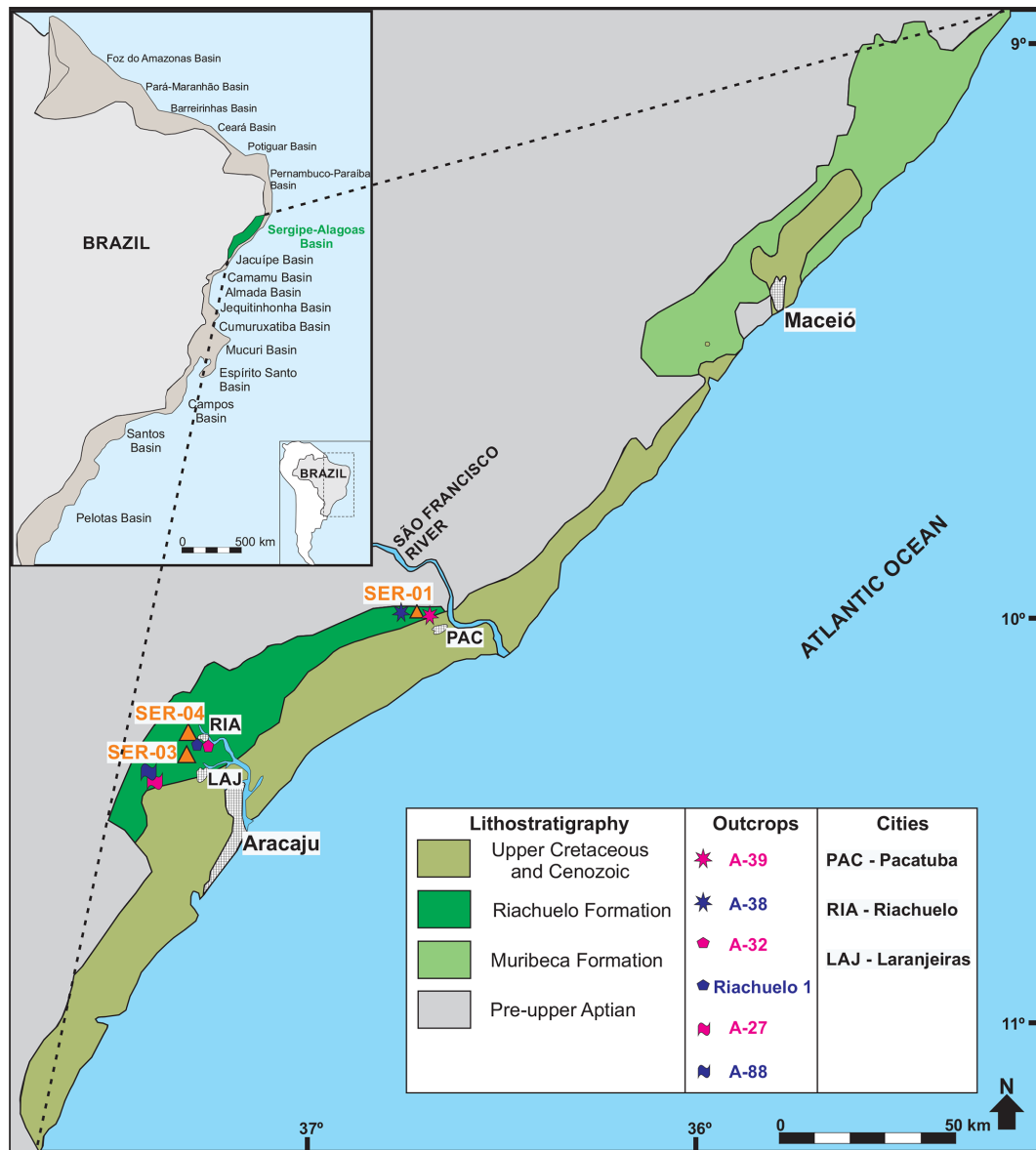
Figure 2. Sketch map of eastern Brazil with the lithostratigraphy of the Sergipe–Alagoas Basin (modified of Bengtson, 1983), locations of boreholes (SER-01, SER-03, and SER-04), key outcrops near the cores (see Table 1), and major cities.

each sample was identified. The mass of all samples was measured to normalize their mass according to magnetic parameters. Paleomagnetic susceptibility measurements were carried out at the Laboratório de Paleomagnetismo e Geomagnetismo (USPMag) of the Universidade de São Paulo. Magnetic susceptibility (χ) measurements were made with a MFK1-FA multifunction kappabridge (Dearing et al., 1996; Hrouda and Pokorný, 2012) at two operating frequencies (976 and 15 616 Hz) in a field of 200 A m^{-1}. To recognize the characteristic remnant magnetization (ChRM), stepwise alternating field (AF) demagnetization was used. A total of 368 samples from core SER-03 were measured after progressive AF treatment at 2, 4, 7, 10, 15, 20, 25, 30, 35, 40, 50, 60,

70, 80, 90, and 100 mT using a 2-G Enterprises cryogenic magnetometer (model u-channel 755R) housed in a magnetically shielded room. The components of ChRM directions were determined from the interpretation of vector end-point demagnetization diagrams (Zijderveld, 1967), and magnetic components were calculated using principal component analysis (Kirschvink, 1980) and analyzed using the Remasoft 3.0 paleomagnetic software package.

5   Results

The drilling campaigns managed to successfully collect Lower Cretaceous carbonate and siliciclastic sediments (on-
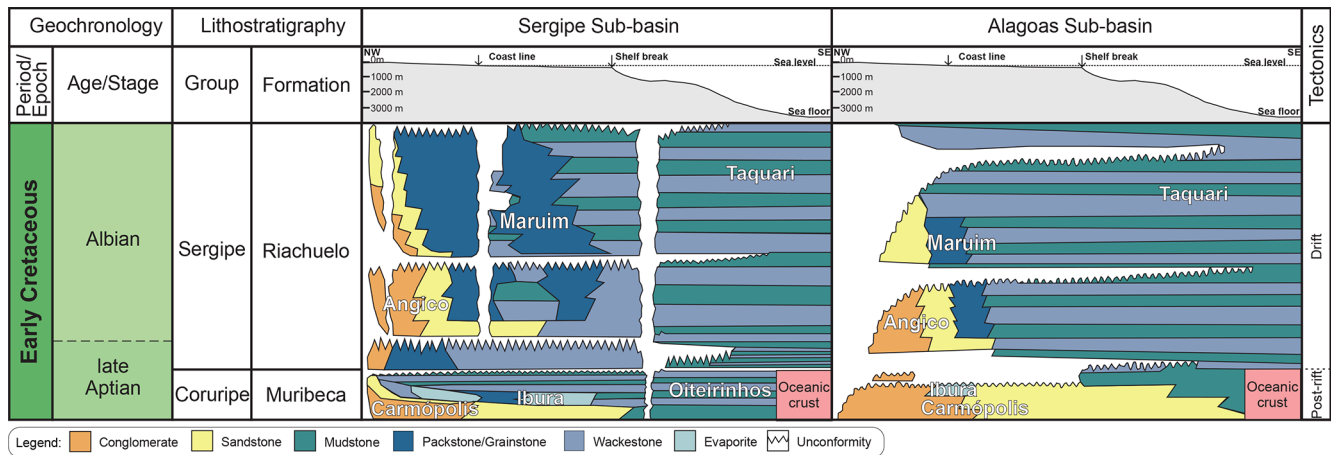
Figure 3. Lithostratigraphic chart of the late Aptian–Albian interval deposits of the Sergipe–Alagoas Basin (e.g., Schaller, 1969; Campos Neto et al., 2007; Bengtson et al., 2018).

Figure 4. The drilling rig used to retrieve core material for this study was mainly oriented perpendicular to the strata truncated.

shore section) from the Riachuelo Formation, Sergipe–Alagoas Basin. Preliminary sedimentological results for each core that mainly represent Riachuelo Formation deposits and magnetostratigraphic, cyclostratigraphic, and biostratigraphic results of core SER-03 are summarized below (Table 1). Detailed stratigraphic studies will be carried out as more analyses of the recovered cores are performed.

Core SER-01 has a total length of 174.7 m, with a recovery of 82.8 % (Table 1). It has been divided into three main lithostratigraphic units, from the base to the top (Fig. 5). Unit I (basal unit) consists of the interval ranging from 174.7

to 99.2 m and is characterized mainly by fine- to coarse-grained sandstone. At the top of this unit, the sandstone is interbedded with centimeter-scale mudstone layers. In addition, within the unit, a large amount of (millimeter- to centimeter-scale) phytoclasts was observed. Unit II (99.2–24.1 m) is the most calcareous interval in the section, characterized from the base to the top by light gray fine-grained sandstones, medium gray mudstones, and light gray marls (Fig. 6). Centimeter-scale beds of medium gray wackestone and packstone were observed in the interval between 81.7 and 52.4 m, which usually contain abundant gastropod and bivalve shells as well as ooliths. In addition, small fractures filled with calcite were also observed. Unit III (24.1–2.6 m) consists mainly of medium gray shale (24.1–14.7 m) grading into a gray claystone (interval 14.7–2.6 m). The interval between 2.6 and 0 m is composed of yellow to white soil and weathered rock. Outcrops (A-38 and A-39) near the core SER-01 contain late Aptian ammonites and foraminifers from the Taquari and Maruim members (Table 1).

Core SER-03 has a total length of 200.1 m, with a recovery of 87.7 % (Table 1). It was divided into two lithostratigraphic units (Fig. 5). Unit I includes the interval between 198 and 95.3 m and is composed mainly of thick intercalated layers of dark gray shale and light gray marl. There are at least two intervals where the shale exhibits a dark gray color (184.3–183.3 and 153.0–151.5 m). Phytoclasts occur in the shales locally. Small beds of calcareous mudstone occur between the depths of 178.3 and 177.6 m (Fig. 6). Ammonite shells are observed at 116.4 and 144.5 m (Fig. 5). Unit II (95.3–5.8 m) is characterized mainly by thick intercalated layers of medium light gray mudstone and medium light gray shale (95.3–15.6 m) followed by grayish-brown claystones (12.5–5.8 m). Fine- to medium-grained sandstones forming millimeter- to centimeter-thick layers (55.2–25.7 m) can be observed at specific depths in the core. Ammonite fossils are also found in the mudstone layers
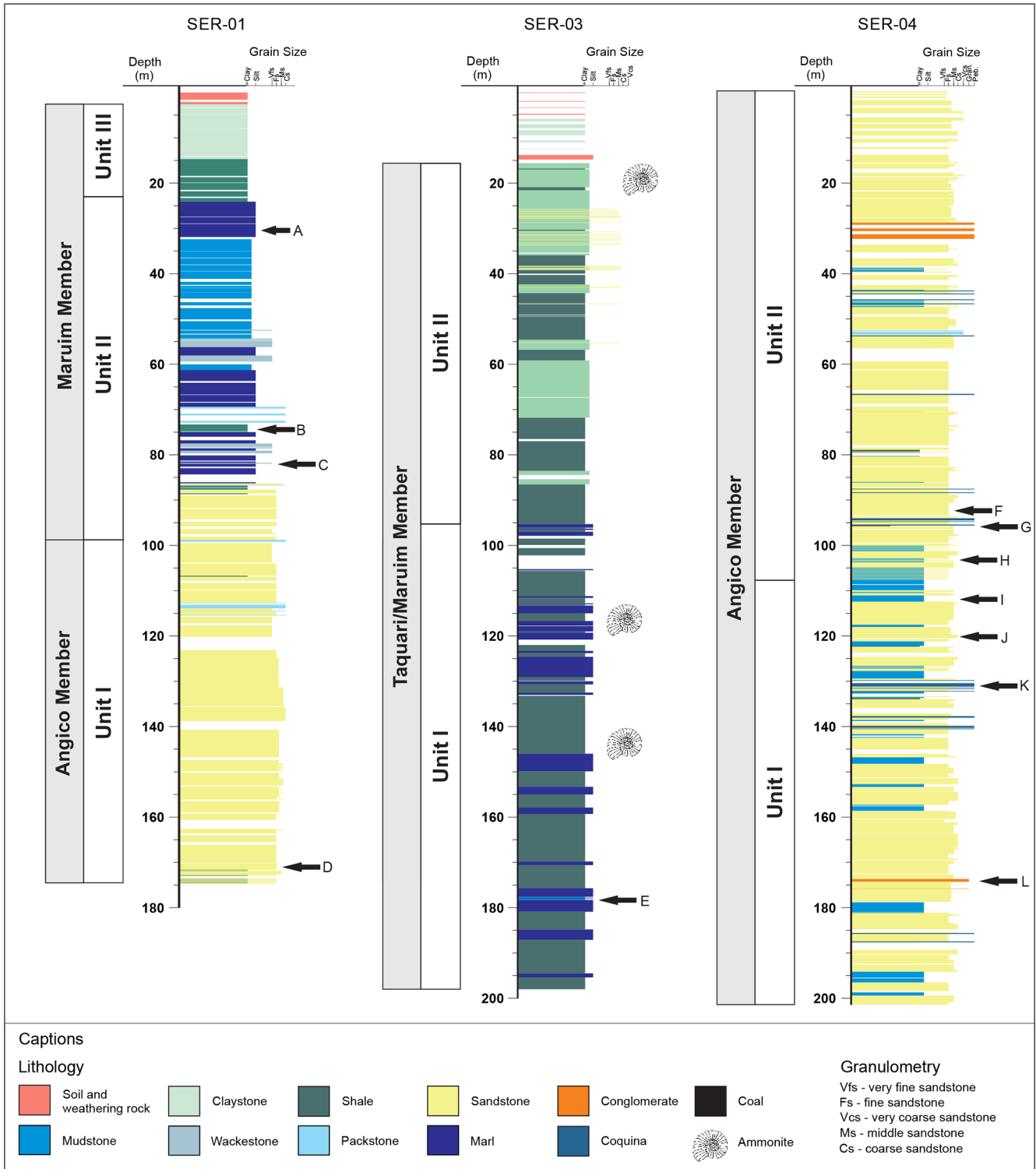
Figure 5. Stratigraphic sections of the Early Cretaceous cores (Aptian–Albian interval) from the Riachuelo Formation (Sergipe–Alagoas Basin), showing the distinct lithostratigraphic units and ammonites identified for each core. The lithostratigraphic units in each core are tentatively assigned to the different members identified in the deposits from the Riachuelo Formation. The levels (black arrows) at which detail pictures of different lithologies were taken are indicated (see Fig. 6).

Table 1. Overview of the cores obtained from the Riachuelo Formation and Sergipe–Alagoas Basin as well as a summary of the main paleontological and stratigraphic features of outcrops in the vicinity of drill sites in the Riachuelo Formation and Sergipe–Alagoas Basin. Information adapted from Koutsoukos (1989) and Siqueira (2005).

Drilled cores' data			
Drilling data	SER-01	SER-03	SER-04
Drilling site city	Pacatuba	Laranjeiras	Riachuelo
UTM-N (datum WGS 84)	8848772	8807705	8812502
UTM-E (datum WGS 84)	751401	691528	697149
Total drill core length (meters)	174.7	200.1	201.4
Total recovery (%)	82.8	87.7	82.5
Main paleontological and stratigraphic features of outcrops in the vicinity of drilled cores			
Locality data	SER-01	SER-03	SER-04
Locality name	A-38	A-27	A-32
Type	Outcrop on the road from Japoatã to Pacatuba	Outcrop on the BR-235 highway	Outcrop near Riachuelo
UTM-N (datum WGS 84)	8849775	8806125	8812575
UTM-E (datum WGS 84)	750675	688470	698525
Fossils	Ammonites and foraminifers	Ammonites and foraminifers	Ammonites and foraminifers
Lithostratigraphy	Riachuelo Formation, Taquari Member	Riachuelo Formation, Angico Member	Riachuelo Formation, Taquari Member
Biostratigraphy	*Cheloniceras* spp. zone (ammonite)	*Douvilleiceras euzebioi/ Oxytropidoceras buarquianum* zones (ammonites)	*Douvilleiceras euzebioi* zone (ammonite)
Age	Late Aptian	Early–middle Albian	Early Albian
Locality data	SER-01	SER-03	SER-04
Locality name	A-39	A-28	Riachuelo 1
Type	Santo Antônio quarry; road from Japoatã to Pacatuba	Outcrop on the BR-235 highway	Outcrop located between the SE-210 and SE-102 highways
UTM-N (datum WGS 84)	8847700	8806575	8812424
UTM-E (datum WGS 84)	752250	688100	698482
Fossils	Ammonites	Ammonites	Ammonites, bivalves (*Neithea* and *Pina*), gastropods, and echinoids
Lithostratigraphy	Riachuelo Formation, Maruim Member	Riachuelo Formation, Angico Member	Riachuelo Formation
Biostratigraphy	*Cheloniceras* spp. zone (ammonite)	*Douvilleiceras euzebioi/ Oxytropidoceras buarquianum* zones (ammonites)	*Eodouvilleiceras* sp. 1 and *Douvilleiceras* aff. *mammillatum* (ammonites association)
Age	Late Aptian	Early–middle Albian	Aptian–Albian

(19.5–17.5 m) (Fig. 5). Vegetation fragments occur throughout the interval. Lastly, the top 15 m of the core is characterized by unconsolidated soil and weathered rock. In addition, foraminifers collected from some samples were previously assigned to the *Microhedbergella renilaevis* and *Ticinella primula* planktic foraminiferal zones, suggesting an early Albian age (Kochhann et al., 2019). Outcrops (A-27 and A-28 of the Angico Member) near core SER-03 contain ammonites and foraminifers from the early–middle Albian (Table 1).
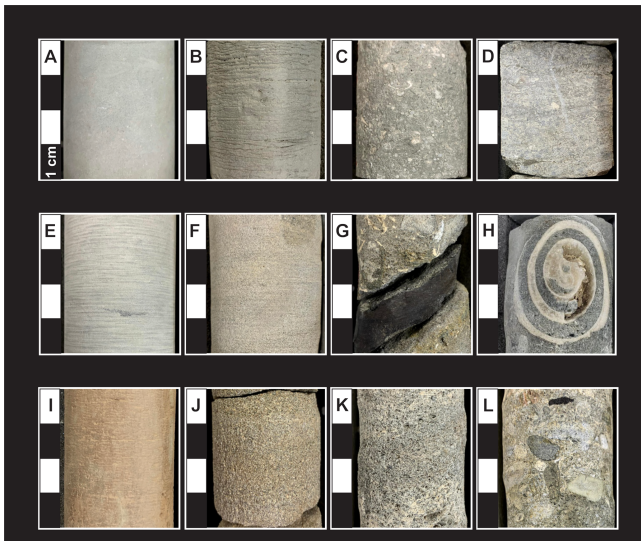
Figure 6. Core sections showing lithologies identified in this study: **(A)** marl (SER-01, 30.68–30.74 m); **(B)** shale (SER-01, 73.99–73.93 m); **(C)** wackestone (SER-01, 81.75–81.69 m); **(D)** packstone (SER-01, 172.69–172.63 m); **(E)** mudstone (SER-03, 178.30–178.24 m); **(F)** medium sandstone (SER-04, 93.06–93.00 m); **(G)** coal (SER-04, 95.63–95.62 m); **(H)** gastropod shell (SER-04, 102.98–102.93 m); **(I)** mudstone (SER-04, 111.84–111.90 m); **(J)** coarse sandstone (SER-04, 120.85–120.79 m); **(K)** coquina (SER-04, 130.94–130.88 m); and **(L)** conglomerate (SER-04, 175.9–175.8 m). The scale bar represents 1 cm.

Core SER-04 has a total length of 201.4 m, with a recovery of 82.5 % (Table 1). The deposits of core SER-04 are primarily sandstones with varying grain sizes. It has been divided into two main lithostratigraphic units (Fig. 5). Unit I (201.4–107.7 m) is dominated by intercalated coarse- to fine-grained sandstones and thick mudstone layers (Fig. 6). Throughout the unit, there are at least eight medium reddish-brown mudstone horizons contrasted with medium light gray mudstones. There are occurrences of conglomeratic sandstone beds (two) in the interval between 175.9 and 173.8 m and centimeter-scale coquina beds in the interval ranging from 140.3 to 129.7 m (Fig. 6). Unit II (107.7–0.9 m) is composed mainly of fine- to coarse-grained sandstones varying in color from grayish brown to light olive gray. At the base (107.7–100.0 m), the unit is mainly characterized by thick layers of fine- to medium-grained sandstones interbedded with mudstones, and gastropod shells also occur (Fig. 6). These sandstones can also be interbedded with light gray coquinas, coal (95.6–43.7 m), medium light gray shales (80.3–78.9 m), medium light gray mudstones (54.7–38.9 m), and medium light gray packstones with abundant gastropod and bivalve shells (54.3–53.2 m). Light gray conglomeratic sandstones composed of granules and pebbles occur at the top of the section (interval 32.2–28.5 m). Finally, there are two remarkable horizons of hybrid centimeter-thick sandstones containing abundant mollusk shells at depths of 26.4–21.2

and 6.0–4.4 m (Fig. 5). Outcrops (A-32 and Riachuelo 1) near core SER-04 contain Aptian–early Albian ammonites and foraminifers and a rich assemblage of bivalves, gastropods, and echinoids from the Taquari Member (Table 1).

For paleomagnetic and cyclostratigraphic data, a total of 368 discrete $\sim 8\,\mathrm{cm^3}$ samples from core SER-03 are measured in low (χlf, Fig. 7a) and high (χhf, Fig. 7b) operating frequencies. Magnetic susceptibility (χlf) values ranged from 1.26×10^{-7} to $1.83 \times 10^{-8}\,\mathrm{m^3\,kg^{-1}}$ (mean of $8.41 \times 10^{-8}\,\mathrm{m^3\,kg^{-1}}$). The χlf values displayed sharp amplitude changes throughout the core. Magnetic susceptibility (χhf) varied between 1.23×10^{-7} and $1.82 \times 10^{-8}\,\mathrm{m^3\,kg^{-1}}$ (mean of $8.18 \times 10^{-8}\,\mathrm{m^3\,kg^{-1}}$) throughout core SER-03 (Fig. 7b), which is close to what was observed with χlf. Frequency-dependent susceptibility (χfd $= (\chi$lf $- \chi$hf$)/\chi$lf $\times 100$) allows for the quantification of contributions from ultra-fine superparamagnetic (SP) particles (Gewehr de Mello et al., 2020). The χfd in the studied sequence (Fig. 7c) ranged from 0 % to 5.69 % (2.70 % average), which indicates that the samples contain a mixture of SP and coarse grains.

Throughout the studied section, the intensity of the magnetization ranged from 2.49×10^{-9} to $9.49 \times 10^{-8}\,\mathrm{Am^2\,kg^{-1}}$ (mean of $2.68 \times 10^{-8}\,\mathrm{Am^2\,kg^{-1}}$) (Fig. 7d). Stepwise AF demagnetization of the representative sediment samples (190.05, 125.79, 76.38, and 23.75 m) revealed a stable and well-defined natural remnant magnetization (NRM) component (Fig. 8). All identified magnetization directions with negative inclinations correspond to a normal polarity field (Fig. 8). These results suggest that the studied section is part of the Cretaceous Normal Superchron (Gewehr de Mello et al., 2020). Similar results have already been reported for the region (e.g., Font et al., 2009). Furthermore, Kochhann et al. (2019) developed a cyclostratigraphic preliminary study, using biostratigraphic markers (*M. renilaevis* and *T. primula* planktic foraminiferal zones) and gamma-ray data, estimating that the sedimentary succession of SER-03 spans about 4 Myr.

6   Future plans

The deposits recovered from the drill cores (SER-01, SER-03, and SER-04) contain complete records from the Aptian–Albian interval of the South Atlantic Ocean. Detailed multidisciplinary studies are being conducted in samples from these cores in order to develop a multiproxy, high-resolution dataset, which will be composed of micropaleontologic (planktonic foraminifera, calcareous nannofossils, radiolarians, ostracods, dinoflagellate cysts, pollens, and spores), microbiofaciologic, and ichnologic (ichnofabric, ichnological suites, and ichnofacies) data. Furthermore, paleomagnetic (paleosecular variation, paleointensity, environmental magnetism), geochemical (X-ray fluorescence, XRF; X-ray diffractometry, XRD; percentage of total organic carbon, TOC; sulfur, S, and CaCO$_3$ content; and strontium, car-
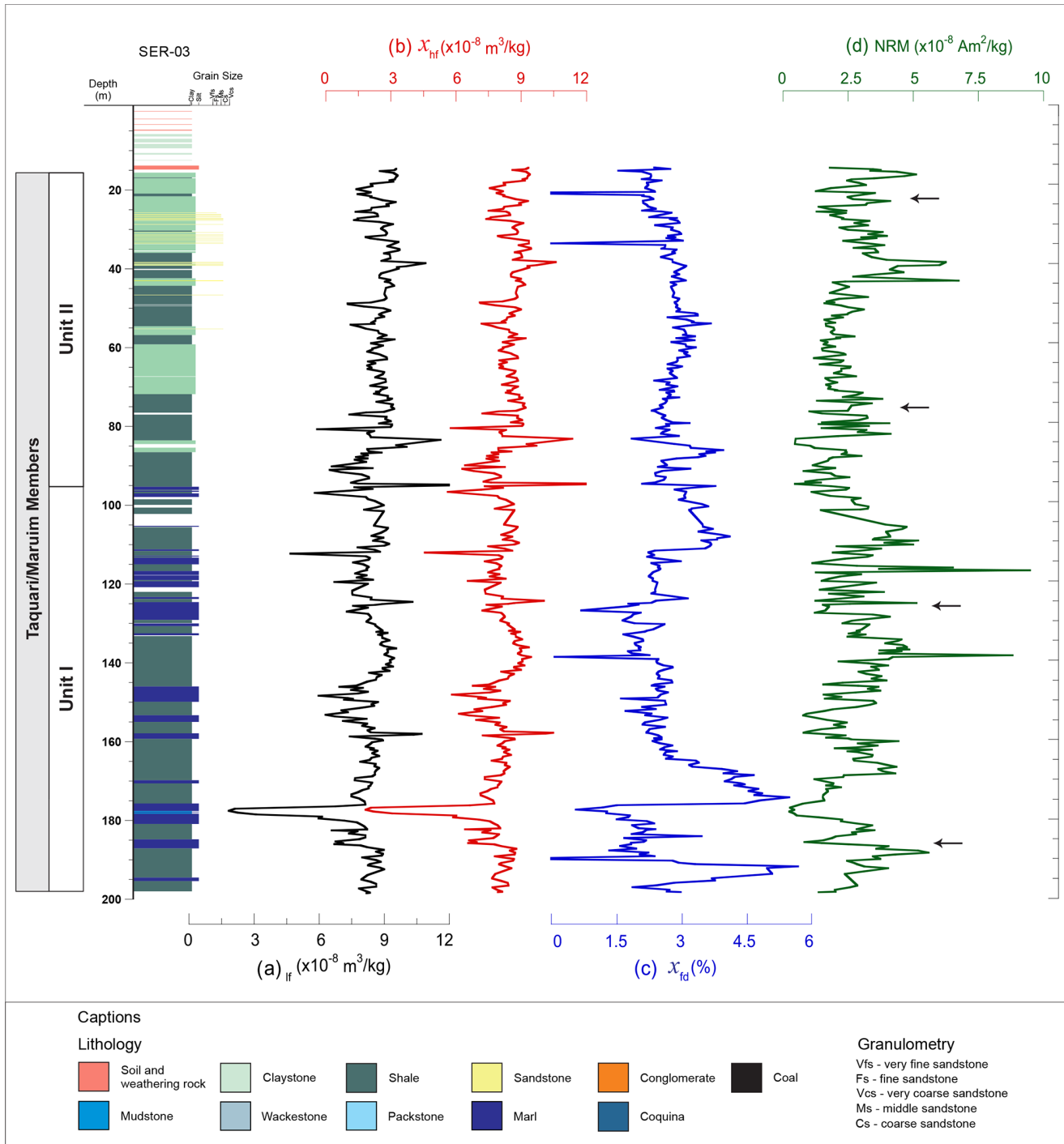
Figure 7. Magnetic susceptibility in low-frequency (**a**), high-frequency (**b**), and frequency-dependent susceptibility (**c**) data of 368 samples from core SER-03. Natural remnant magnetization (NRM) of 368 samples from core SER-03 is also show. The positions of the paleomagnetic samples in Fig. 8 are indicated by black arrows.

bon, oxygen, and calcium isotopes), and cyclostratigraphic (orbital tuning and evolutive spectral analysis) data will also be included. The combination of these paleontological, sedimentological, and geochemical analyses in the drill core samples will provide invaluable information about

the Aptian–Albian, such as the biostratigraphy, paleoclimatic changes, paleoenvironmental evolution, and paleoceanographic parameters of the South Atlantic Ocean during this time interval.
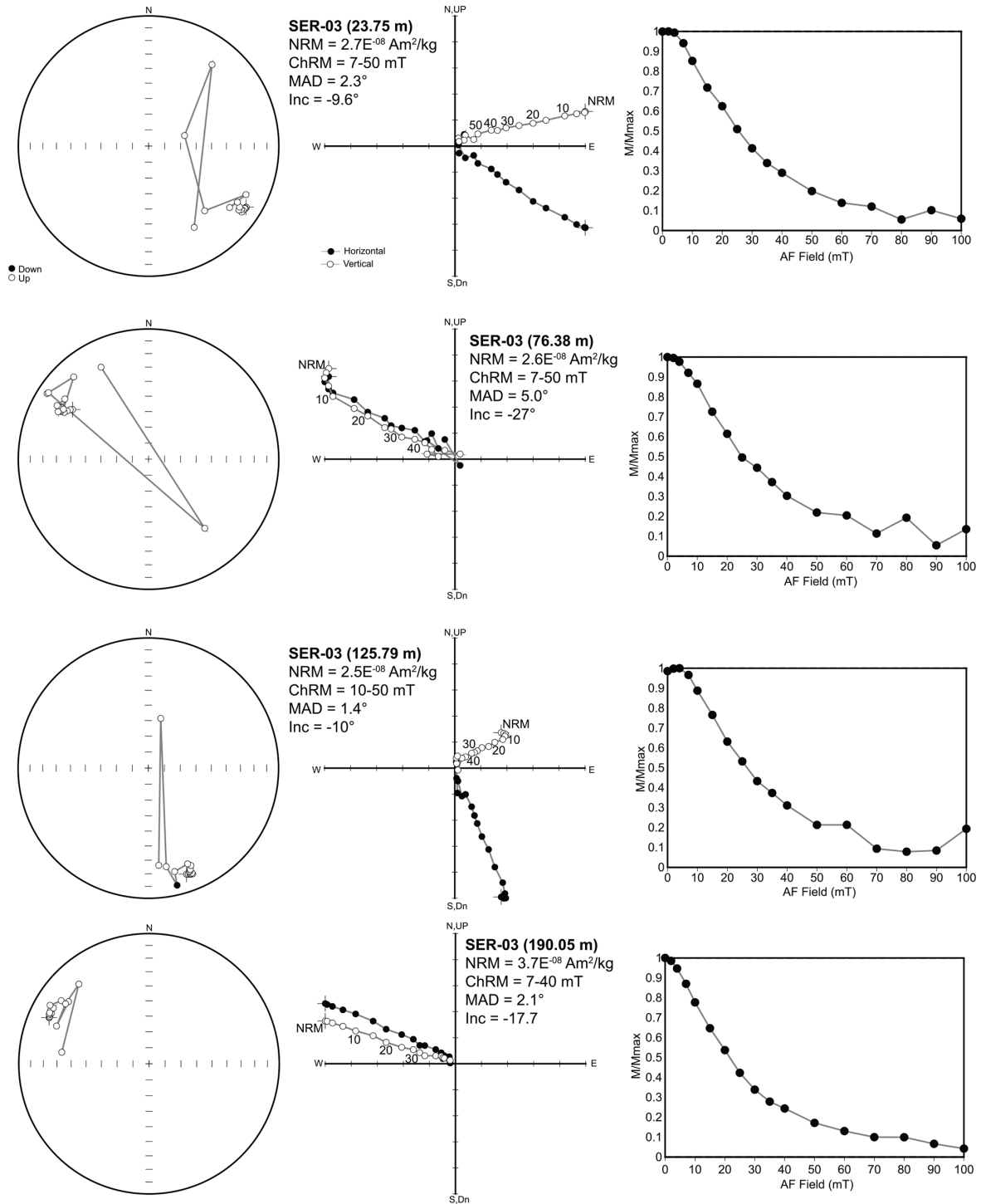
Figure 8. Typical alternating field (AF) demagnetization plots of four representative samples from the studied section. The down-core position of the samples is indicated by arrows in Fig. 7. Solid symbols indicate normal components; open symbols indicate reverse components.

7   Conclusion

The drilling campaigns successfully collected Lower Cretaceous rocks (onshore section) from the Riachuelo Formation of the Sergipe–Alagoas Basin. Three holes were cored in this formation; they represent the only known preserved carbonate shelf containing the Aptian–Albian transition in Brazil and most likely constitute a complete record of an Aptian–Albian sedimentary section of the South Atlantic Ocean.

Sedimentological data of the SER-01, SER-02, and SER-03 cores show that mixed calcareous–siliciclastic sediments can be assigned to the Angico Member and probably represent deposits of delta fan. The calcareous rocks retrieved are part of the Maruim and Taquari members, mainly deposited on a carbonate shelf, on the external shelf, and on the slope, respectively. Furthermore, phytoclasts, gastropod, and bivalve shells were observed in the deposits of the core SER-01, whereas phytoclasts, ammonite shells, and foraminifers were observed in the deposits of the core SER-03. In this core, foraminifers collected from some samples were assigned to the *Microhedbergella renilaevis* and *Ticinella primula* planktic foraminiferal zones, suggesting an early Albian age. In addition, core SER-04 recovered coquina layers and abundant mollusk shells, suggesting that microfossil assemblages can be obtained from these sediment samples. The paleomagnetic results obtained in the deposits of core SER-03 suggest that the section is part of the Cretaceous Normal Superchron. The cyclostratigraphic data and gamma-ray data suggest that the sedimentary succession spans about 4 Myr.

A combination of stratigraphic, sedimentological, paleomagnetism, geochemical, ichnological, and micropaleontological approaches will be applied to obtain critical information on the characteristics of the deposits and to understand the influence of the paleoclimatic and paleoceanographic global events (e.g., Vocontian Basin and PLG) at the Aptian–Albian interval in the South Atlantic and to assess if a correlation exists between the biotic assemblages of the South Atlantic Ocean and the Tethys Sea. In addition, such integrated analysis of the late Aptian–Albian interval will bring new insights into the stratigraphy and tectonic history of the basin as well as the onset and early evolution of the South Atlantic. Cores drilled in this project can potentially allow for the correlation and calibration of local biozones with global biozones.

The results from the onshore sites drilled in the Sergipe–Alagoas Basin will contribute to International Ocean Discovery Program (IODP) Expedition 388, Equatorial Atlantic Gateway: origin, evolution, and paleoenvironment of the Equatorial Atlantic Gateway (Dunkley Jones et al., 2019).

Data availability. All data from this research are published in this paper.

Author contributions. GF was responsible for writing, reviewing, and editing the paper in addition to conceptualizing and supervising the study. MDRB, JVM, and JFS contributed to writing, reviewing, and editing the paper. FHdOL and OS Jr. wrote the original draft of the paper in addition to preparing, conceptualizing, and supervising the study. RdMG, GK, RGdM, FML, CGL, and EdSA contributed to the investigation.

References

Antonietto, L. S., Carmo, D. A., Viviers, M. C., and Adôrno, R. R.: Biostratigraphic and paleozoogeographic review of the upper Aptian-Albian ostracods of riachuelo formation, Sergipe-Alagoas Basin, Northeastern Brazil, Rev. Bras. Paleontolog., 18, 355–368, https://doi.org/10.4072/rbp.2015.3.02, 2015.

Arai, M.: Aptian/Albian (Early Cretaceous) paleogeography of the south atlantic: A paleontological perspective, Braz. J. Geol., 44, 339–350, https://doi.org/10.5327/Z2317-4889201400020012, 2014.

Arthur, M. A. and Natland, J. H.: Carbonaceous sediments in the North and South Atlantic: The role of salinity in stable stratification of early Cretaceous basins, in: Deep Drilling Results in the Atlantic Ocean: Continental Margins and Paleoenvironment, edited by: Talwani, M., Hay, W., and Ryan, W. B. F., American Geophysical Union, Washington, USA, 375–401, available at: https://agupubs.onlinelibrary.wiley.com/doi/10.1029/ME003p0375 (last access: 1 April 2021), 1979.

Asmus, H. E.: Geologia da margem continental brasileira, in: Geologia do Brasil, edited by Schobbenhaus, C., Campos, D. A., Derze, G. R., and Asmus, H. E., DNPM, Brasilia, 443–472, 1984.

Asmus, H. E. and Porto, R.: Classificação das bacias sedimentares brasileiras segundo a tectônica de placas, in: Anais do XXVI Congresso Brasileiro de Geologia, Sociedade Brasileira de Geologia, October 1972, Belem, Brazil, 67–90, 1972.

Azevedo, R. L. M.: Paleoceanografia e a evolução do Atlântico Sul no Albiano, Boletim de Geociências da Petrobras, 12, 231–249, 2004.

Bengtson, P.: The Cenomanian-Coniacian of the Sergipe Basin, Brazil, Universitetsforlaget, Oslo, Norway, 1983.

Bengtson, P., Zucon, M. H., and da Conceição Santos Sobral, A.: Cretaceous ammonite zonation of the Sergipe Basin, northeastern Brazil, Cretaceous Res., 88, 111–122, https://doi.org/10.1016/j.cretres.2017.07.021, 2018.

Berggren, W. A. and Hollister, C. D.: Paleogeography, paleobiogeography and the history of circulation in the Atlantic Ocean, in: Studies in Paleo-Oceanography, edited by: Hay, W. W., Society of Economic Paleontologists and Mineralogists, Special Publications, 126–186, http://archives.datapages.com/data/sepm_sp/SP20/Paleogeography_Paleobiogeography.htm (last access: 15 April 2020), 1974.

Beurlen, K.: A posição estratigráfica da Formação Riachuelo – (Cretáceo, Sergipe), Bol. Soc. Bras. Geol., 17, 85–88, 1968.

Biggin, A. J., van Hinsbergen, D. J. J., Langereis, C. G., Straathof, G. B., and Deenen, M. H. L.: Geomagnetic secular variation in the Cretaceous Normal Superchron and in the Jurassic, Phys. Earth Planet. In., 169, 3–19, https://doi.org/10.1016/j.pepi.2008.07.004, 2008.

Bottini, C. and Erba, E.: Mid-Cretaceous paleoenvironmental changes in the western Tethys, Clim. Past, 14, 1147–1163, https://doi.org/10.5194/cp-14-1147-2018, 2018.

Bottini, C., Erba, E., Tiraboschi, D., Jenkyns, H. C., Schouten, S., and Sinninghe Damsté, J. S.: Climate variability and ocean fertility during the Aptian Stage, Clim. Past, 11, 383–402, https://doi.org/10.5194/cp-11-383-2015, 2015.

Browning, E. L. and Watkins, D. K.: Elevated primary productivity of calcareous nannoplankton associated with ocean anoxic event 1b during the Aptian/Albian transition (Early Cretaceous), Paleoceanography, 23, 1–11, https://doi.org/10.1029/2007PA001413, 2008.

Bruno, M. D. R., Fauth, G., Watkins, D. K., and Savian, J. F.: Albian-Cenomanian calcareous nannofossils from DSDP Site 364 (Kwanza Basin, Angola): Biostratigraphic and paleoceanographic implications for the South Atlantic, Cretaceous Res., 109, 104377, https://doi.org/10.1016/j.cretres.2020.104377, 2020.

Cainelli, C., Babinski, N. A., Santos, R. C. R., and Uesugui, N.: Sedimentos albo-santonianos da Bacia Sergipe-Alagoas: ambientes de sedimentação e perspectivas petrolíferas, Revista Brasileira de Geociências, 17, 135–138, 1987.

Campos Neto, O. P. d. A., Souza-Lima, W., and Gomes Cruz, F. E.: Bacia de Sergipe-Alagoas, Boletim de Geociências da Petrobras, 15, 405–415, 2007.

Carvalho, M. d. A., Bengtson, P., and Lana, C. C.: Late Aptian (Cretaceous) paleoceanography of the South Atlantic Ocean inferred from dinocyst communities of the Sergipe Basin, Brazil, Paleoceanography, 31, 2–26, https://doi.org/10.1002/2014PA002772, 2016.

Clarke, L. J. and Jenkyns, H. C.: New oxygen isotope evidence for long-term Cretaceous climatic, Geology, 27, 699–702, https://doi.org/10.1130/0091-7613(1999)027<0699:NOIEFL>2.3.CO;2, 1999.

Coccioni, R., Jovane, L., Bancalà, G., Bucci, C., Fauth, G., Frontalini, F., Janikian, L., Savian, J., Paes de Almeida, R., Mathias, G. L., and Ferreira da Trindade, R. I.: Umbria-Marche Basin, Central Italy: A Reference Section for the Aptian-Albian Interval at Low Latitudes, Sci. Dril., 13, 42–46, https://doi.org/10.2204/iodp.sd.13.07.2011, 2012.

Coccioni, R., Sabatino, N., Frontalini, F., Gardin, S., Sideri, M., and Sprovieri, M.: The neglected history of Oceanic Anoxic Event 1b: insights and new data from the Poggio le Guaine section (Umbria-Marche Basin), Stratigraphy, 11, 245–282, 2014.

Colin, J.-P. and Andreu, B.: Cretaceous halocyprid Ostracoda, in: Ostracoda and Global Events, edited by: Whatley, C. and Maybury, R., Chapman and Hall, London, UK, 515–523, 1990.

Courtillot, V. E. and Renne, P. R.: On the ages of flood basalt events, C. R. Geosci., 335, 113–140, https://doi.org/10.1016/S1631-0713(03)00006-3, 2003.

Cronin, M., Tauxe, L., Constable, C., Selkin, P., and Pick, T.: Noise in the quiet zone, Earth Planet. Sc. Lett., 190, 13–30, https://doi.org/10.1016/S0012-821X(01)00354-5, 2001.

Dearing, J. A., Dann, R. J. L., Hay, K., Lees, J. A., Loveland, P. J., Maher, B. A., and O'Grady, K.: Frequency-dependent susceptibility measurements of environmental materials, Geophys. J. Int., 124, 228–240, https://doi.org/10.1111/j.1365-246X.1996.tb06366.x, 1996.

Dias-Brito, D.: A Bacia de Campos no MesoCretáceo: Uma contribuição à paleoceanografia do Atlântico Sul primitivo, Revista Brasileira de Geociências, 17, 162–167, https://doi.org/10.25249/0375-7536.1987162167, 1987.

Dummann, W., Steinig, S., Hofmann, P., Flögel, S., Osborne, A. H., Frank, M., Herrle, J. O., Bretschneider, L., Sheward, R. M., and Wagner, T.: The impact of Early Cretaceous gateway evolution on ocean circulation and organic carbon burial in the emerging South Atlantic and Southern Ocean basins, Earth Planet. Sc. Lett., 530, 1–11, https://doi.org/10.1016/j.epsl.2019.115890, 2020.

Dunkley Jones, T., Fauth, G., and LeVay, L. J.: Expedition 388 Scientific Prospectus: Equatorial Atlantic Gateway: origin, evolution, and paleoenvironment of the Equatorial Atlantic Gateway, International Ocean Discovery Program, 1–31, https://doi.org/10.14379/iodp.sp.388.2019, 2019.

Erbacher, J., Hemleben, C., Huber, B. T., and Markey, M.: Correlating environmental changes during early Albian oceanic anoxic event 1B using benthic foraminiferal paleoecology, Mar. Micropaleontol., 38, 7–28, https://doi.org/10.1016/S0377-8398(99)00036-5, 1999.

Feijó, F. J.: Bacias de Sergipe e Alagoas, Boletim de Geociências da Petrobras, 8, 149–161, 1994.

Feijó, F. J.: O início da livre circulação das águas do Oceano Atlântico, Boletim de Geociências da Petrobras, 10, 157–164, 1996.

Föllmi, K. B.: Early Cretaceous life, climate and anoxia, Cretaceous Res., 35, 230–257, https://doi.org/10.1016/j.cretres.2011.12.005, 2012.

Font, E., Ernesto, M., Silva, P. F., Correia, P. B., and Nascimento, M. A. L.: Palaeomagnetism, rock magnetism and AMS of the Cabo Magmatic Province, NE Brazil, and the opening of South Atlantic, Geophys. J. Int., 179, 905–922, https://doi.org/10.1111/j.1365-246X.2009.04333.x, 2009.

Gale, A. S., Mutterlose, J., Batenburg, S. J., Gradstein, F. M., Agterberg, F. P., Ogg, J. G., and Petrizzo, M. R.: The Cretaceous Period, in: Geologic Time Scale 2020, edited by: Gradstein, F. M., Ogg, J. G., Schmitz, M. B., and Ogg, G. M., Elsevier, 1023–1086, https://doi.org/10.1016/C2020-1-02369-3, 2020.

Gee, J. S. and Kent, D. V.: Source of Oceanic Magnetic Anomalies and the Geomagnetic Polarity Timescale, Treatise on Geophysics, 5, 455–507, https://doi.org/10.7916/D8DV1V8P, 2007.

Gewehr de Mello, R., Fauth, G., Guilherme Diemer Kochhann, K., Gonsalves Leandro, C., Daniel Rodrigues Bruno, M., Krahl, G., Marcanth Lopes, F., and Francisco Savian, J.: Magnetostratigraphy and environmental magnetism of the Aptian-Albian boundary of sedimentary core from Sergipe-Alagoas Basin: preliminary results, EGU General Assembly 2020, Online, 4–8 May 2020, EGU2020-17533, https://doi.org/10.5194/egusphere-egu2020-17533, 2020.

Granot, R., Tauxe, L., Gee, J. S., and Ron, H.: A view into the Cretaceous geomagnetic field from analysis of gabbros and submarine glasses, Earth Planet. Sc. Lett., 256, 1–11, https://doi.org/10.1016/j.epsl.2006.12.028, 2007.

Granot, R., Dyment, J., and Gallet, Y.: Geomagnetic field variability during the Cretaceous Normal Superchron, Nat. Geosci., 5, 220–223, https://doi.org/10.1038/ngeo1404, 2012.

Haq, B. U.: Cretaceous eustasy revisited, Global Planet. Change, 113, 44–58, https://doi.org/10.1016/j.gloplacha.2013.12.007, 2014.

Hay, W. W., DeConto, R. M., Wold, C. N., Wilson, K. M., Voigt, S., Schulz, M., Rossby Wold, A., Dullo, W. C., Ronov, A. B., Balukhovsky, A. N., and Söding, E.: Alternative global Cretaceous paleogeography, in: Evolution of the Cretaceous Ocean-climate System, edited by: Barrera, C. C. and Johnson, E., Geological Society of America, Special Paper, Boulder, Colorado, USA, 1–47, 1999.

He, H., Pan, Y., Tauxe, L., Qin, H., and Zhu, R.: Toward age determination of the M0r (Barremian-Aptian boundary) of the Early Cretaceous, Phys. Earth Planet. In., 169, 41–48, https://doi.org/10.1016/j.pepi.2008.07.014, 2008.

Helsley, C. E. and Steiner, M. B.: Evidence for long intervals of normal polarity during Cretaceous period, Earth Planet. Sc. Lett., 1, 325–332, https://doi.org/10.1016/S0012-821X(68)80060-3, 1968.

Herrle, J. O. and Mutterlose, J.: Calcareous nannofossils from the Aptian-Lower Albian of southeast France: Palaeoecological and biostratigraphic implications, Cretaceous Res., 24, 1–22, https://doi.org/10.1016/S0195-6671(03)00023-5, 2003.

Herrle, J. O., Kößler, P., Friedrich, O., Erlenkeuser, H., and Hemleben, C.: High-resolution carbon isotope records of the Aptian to Lower Albian from SE France and the Mazagan Plateau (DSDP Site 545): A stratigraphic tool for paleoceanographic and paleobiologic reconstruction, Earth Planet. Sc. Lett., 218, 149–161, https://doi.org/10.1016/S0012-821X(03)00646-0, 2004.

Herrle, J. O., Schröder-Adams, C. J., Davis, W., Pugh, A. T., Galloway, J. M., and Fath, J.: Mid-cretaceous high arctic stratigraphy, climate, and oceanic anoxic events, Geology, 43, 403–406, https://doi.org/10.1130/G36439.1, 2015.

Hessel, M. H.: Gervillia (Gervillia) solenoidea Defrance, 1820 (Bivalvia Bakevelliidae) do Neo-aptiano de Sergipe, Brasil, Rev. Bras. Paleontolog., 7, 67–76, 2004.

Hrouda, F. and Pokorný, J.: Modelling accuracy limits for frequency-dependent anisotropy of magnetic susceptibility of rocks and soils, Stud. Geophys. Geod., 56, 789–802, https://doi.org/10.1007/s11200-011-9009-5, 2012.

Hu, X., Wagreich, M., and Yilmaz, I. O.: Marine rapid environmental/climatic change in the Cretaceous greenhouse world, Cretaceous Res., 38, 1–6, https://doi.org/10.1016/j.cretres.2012.04.012, 2012.

Huber, B. T. and Leckie, R. M.: Planktic foraminiferal species turnover across deep-sea Aptian/Albian boundary sections, J. Foramin. Res., 41, 53–95, https://doi.org/10.2113/gsjfr.41.1.53, 2011.

Huber, B. T., MacLeod, K. G., Gröcke, D. R., and Kucera, M.: Paleotemperature and paleosalinity inferences and chemostratigraphy across the Aptian/Albian boundary in the subtropical North Atlantic, Paleoceanography, 26, 1–20, https://doi.org/10.1029/2011PA002178, 2011.

Jenkyns, H. C.: Geochemistry of oceanic anoxic events, Geochem. Geophy. Geosy., 11, 1–30, https://doi.org/10.1029/2009GC002788, 2010.

Jenkyns, H. C., Schouten-Huibers, L., Schouten, S., and Sinninghe Damsté, J. S.: Warm Middle Jurassic–Early Cretaceous high-latitude sea-surface temperatures from the Southern Ocean, Clim. Past, 8, 215–226, https://doi.org/10.5194/cp-8-215-2012, 2012.

Kellogg, J. N. and Mohriak, W. U.: The Tectonic and Geological Environment of Coastal South America, in: Coastal Marine Ecosystems of Latin America, edited by: Seelinger, B. and Kjerfbe, U., 1–16, Springer, Berlin, Heidelberg, Germany, 2001.

Kennedy, J. W., Gale, A. S., Bown, P. R., Caron, M., Davey, R. J., Gröcke, D. R., and Wray, D. S.: Integrated stratigraphy across the Aptian-Albian boundary in the Marnes Bleues, at the Col de Pre-Guittard, Arnayon (Drome), and at Tartonne (Alpes-de-Haute-Provence), France: A candidate global boundary stratotype section and boundary point for the base, Cretaceous Res., 21, 591–720, https://doi.org/10.1006/cres.2000.0223, 2000.

Kennedy, J. W., Gale, A. S., Huber, B. T., Petrizzo, M. R., Bown, P. R., Barchetta, A., and Jenkyns, H. C.: Integrated stratigraphy across the Aptian/Albian boundary at Col de Pré-Guittard (southeast France): A candidate global boundary stratotype section, Cretaceous Res., 51, 248–259, https://doi.org/10.1016/j.cretres.2014.06.005, 2014.

Kennedy, J. W., Gale, A. S., Huber, B. T., Petrizzo, M. R., Bown, P. R., and Jenkyns, H. C.: The Global Boundary Stratotype Section and Point (GSSP) for the base of the Albian Stage, of the Cretaceous, the Col de Pré-Guittard section, Arnayon, Drôme, France, Episodes, 40, 177–188, https://doi.org/10.18814/epiiugs/2017/v40i3/017021, 2017.

Kirschvink, J. L.: The least-square line and plane and the analysis of paleomagnetic data, Geophys. J. Roy. Astr. S., 62, 699–718, https://doi.org/10.1111/j.1365-246X.1980.tb02601.x, 1980.

Kochhann, K. G. D., Krahl, G., Fauth, G., do Monte Guerra, R., Bruno, M. D. R., da Silva Aguiar, E., and Lima, F. H. O.: Cyclostratigraphy of Early Albian Marine Strata of the Sergipe Basin, Brazil, in: AGU Fall Meeting 2019, AGU, 9–13 December 2019, San Francisco, USA, https://agu.confex.com/agu/fm19/meetingapp.cgi/Paper/537653 (last access: 27 April 2020), 2019.

Koutsoukos, E. A. M.: Mid- to Late Cretaceous microbiostratigraphy, palaeoecology and palaeogeography of the Sergipe basin, northeastern Brazil, PhD Thesis, Department of Geological Sciences of Polytechnic South West, Plymouth, UK, 856 pp., 1989.

Koutsoukos, E. A. M.: Late Aptian to Maastrichtian foraminiferal biogeography and palaeoceanography of the Sergipe Basin, Brazil, Palaeogeogr. Palaeocl., 92, 295–324, https://doi.org/10.1016/0031-0182(92)90089-N, 1992.

Koutsoukos, E. A. M. and Bengtson, P.: Towards an integrated biostratigraphy of the upper Aptian-Maastrichtian of the Sergipe Basin, Brazil, Documents des laboratoires de géologie, 125, 241–262, 1993.

Koutsoukos, E. A. M., Mello, M. R., and Azambuja Filho, N. C.: Micropalaeontological and geochemical evidence of mid-Cretaceous dysoxic-anoxic palaeoenvironments in the Sergipe Basin, northeastern Brazil, Geol. Soc. Spec. Publ., 58, 427–447, https://doi.org/10.1144/GSL.SP.1991.058.01.27, 1991a.

Koutsoukos, E. A. M., Mello, M. R., Azambuja Filho, N. C., Hart, M. B., and Maxwell, J. R.: The upper Aptian-Albian succession of the Sergipe Basin, Brazil: an integrated paleoenvironmental assessment, AAPG Bull., 75, 479–498, https://doi.org/10.1306/0C9B2817-1710-11D7-8645000102C1865D, 1991b.

Leckie, R. M., Bralower, T. J., and Cashman, R.: Oceanic anoxic events and plankton evolution: Biotic response to tectonic forcing during the mid-Cretaceous, Paleoceanography, 17, 13-1–13-29, https://doi.org/10.1029/2001pa000623, 2002.

Linder, J. and Gilder, S. A.: Geomagnetic secular variation recorded by sediments deposited during the Cretaceous normal superchron at low latitude, Phys. Earth Planet. In., 187, 245–260, https://doi.org/10.1016/j.pepi.2011.05.010, 2011.

Manso, C. L. C. and Souza-Lima, W.: O Equinóide Douvillaster Lambert, 1917 na Formação Riachuelo, Bacia de Sergipe, Brasil, Rev. Bras. Paleontolog., 5, 29–37, 2003.

McAnena, A., Flögel, S., Hofmann, P., Herrle, J. O., Griesand, A., Pross, J., Talbot, H. M., Rethemeyer, J., Wallmann, K., and Wagner, T.: Atlantic cooling associated with a marine biotic crisis during the mid-Cretaceous period, Nat. Geosci., 6, 558–561, https://doi.org/10.1038/NGEO1850, 2013.

Michels, F. H., de Souza, P. A., and Premaor, E.: Aptian-Albian palynologic assemblages interbedded within salt deposits in the Espírito Santo Basin, eastern Brazil: Biostratigraphical and paleoenvironmental analysis, Mar. Petrol. Geol., 91, 785–799, https://doi.org/10.1016/j.marpetgeo.2018.01.023, 2018.

Milani, E. J., Rangel, H. D., Bueno, G. V., Stica, J. M., Winter, W. R., Caixeta, J. M., and Pessoa Neto, O. d. C.: Bacias Sedimentares Brasileiras – Cartas Estratigráficas, Boletim de Geociências da Petrobras, 15, 183–205, 2007.

Mohriak, W. U.: Bacias Sedimentares da Margem Continental Brasileira, in: Geologia, Tectônica e Recursos Minerais do Brasil, edited by: Bizzi, J. H., Schobbenhaus, L. A., Vidottie, C., and Gonçalves, R. M., CPRM, Brasilia, 87–165, 2003.

Mohriak, W. U. and Fainstein, R.: Phanerozoic regional geology of the eastern Brazilian margin, in: Regional Geology and Tectonics, Elsevier, 222–282, https://doi.org/10.1016/B978-0-444-56357-6.00006-8, 2012.

Mohriak, W. U., Bassetto, M., and Vieira, I. S.: Crustal architecture and tectonic evolution of the Sergipe-Alagoas and Jacuípe basins, offshore northeastern Brazil, Tectonophysics, 288, 199–220, https://doi.org/10.1016/B978-0-444-56357-6.00006-8, 1998.

Mohriak, W. U., Nemcok, M., and Enciso, G.: South Atlantic divergent margin evolution: rift-border uplift and salt tectonics in the basins of SE Brazil, in: Geological Society, edited by: Pankhurst, M. J., Trouw, R. J., Brito Neves, R. A. J., and de Wit, B. B., Geological Society, Special Publications, London, UK, 365–951, https://doi.org/10.1144/SP294.19, 2008.

Mutterlose, J., Bornemann, A., and Herrle, J. O.: The Aptian – Albian cold snap: Evidence for "mid" Cretaceous icehouse interludes, Neues Jahrb. Geol. P.-A., 252, 217–225, https://doi.org/10.1127/0077-7749/2009/0252-0217, 2009.

O'Brien, C. L., Robinson, S. A., Pancost, R. D., Sinninghe Damsté, J. S., Schouten, S., Lunt, D. J., Alsenz, H., Bornemann, A., Bottini, C., Brassell, S. C., Farnsworth, A., Forster, A., Huber, B. T., Inglis, G. N., Jenkyns, H. C., Linnert, C., Littler, K., Markwick, P., McAnena, A., Mutterlose, J., Naafs, B. D. A., Püttmann, W., Sluijs, A., van Helmond, N. A. G. M., Vellekoop, J., Wagner, T., and Wrobel, N. E.: Cretaceous sea-surface temperature evolution: Constraints from TEX86 and planktonic foraminiferal oxygen isotopes, Earth-Sci. Rev., 172, 224–247, https://doi.org/10.1016/j.earscirev.2017.07.012, 2017.

Ogg, J. G., Ogg, G. M., and Gradstein, F. M.: A concise geologic time scale 2016, Elsevier, 234 pp., 2016.

Pérez-Díaz, L. and Eagles, G.: South Atlantic paleo-bathymetry since early Cretaceous, Sci. Rep.-UK, 7, 1–16, https://doi.org/10.1038/s41598-017-11959-7, 2017.

Petrizzo, M. R., Huber, B. T., Gale, A. S., Barchetta, A., and Jenkyns, H. C.: Abrupt planktic foraminiferal turnover across the niveau kilian at col de pré-guittard (Vocontian Basin, southeast France): New criteria for defining the Aptian/Albian boundary, Newsl. Stratigr., 45, 55–74, https://doi.org/10.1127/0078-0421/2012/0013, 2012.

Petrizzo, M. R., Wagreich, M., and Haggart, J.: Annual Report 2016 of the International Subcommission on Cretaceous Stratigraphy, available at: http://cretaceous.stratigraphy.org/archives/ (last access: 10 April 2020), 2016.

Pirrie, D., Doyle, P., Marshall, J. D., and Ellis, G.: Cool Cretaceous climates: new data from the Albian of Western Australia, J. Geol. Soc. London, 152, 139–142, https://doi.org/10.1144/gsjgs.152.5.0739, 1995.

Pirrie, D., Marshall, J. D., Doyle, P., and Riccardi, A. C.: Cool early Albian climates, new data from Argentina, Cretaceous Res., 25, 27–33, https://doi.org/10.1016/j.cretres.2003.10.002, 2004.

Rabinowitz, P. D. and Labrecque, J.: The Mesozoic South Atlantic Ocean and Evolution of Its Continental Margins, J. Geophys. Res.-Sol. Ea., 84, 5973–6002, https://doi.org/10.1029/JB084iB11p05973, 1979.

Rand, H. M. and Mabesoone, J. M.: Northeastern Brazil and the final separation of South America and Africa, Palaeogeogr. Palaeocl., 38, 163–183, https://doi.org/10.1016/0031-0182(82)90002-5, 1982.

Riccardi, A. C.: Jurassic and Cretaceous marine connections between the Southeast Pacific and Tethys, Palaeogeogr. Palaeocl., 87, 189, https://doi.org/10.1016/0031-0182(91)90134-D, 1991.

Sabatino, N., Coccioni, R., Salvagio Manta, D., Baudin, F., Vallefuoco, M., Traina, A., and Sprovieri, M.: High-resolution chemostratigraphy of the late Aptian-early Albian oceanic anoxic event (OAE 1b) from the Poggio le Guaine section

(Umbria-Marche Basin, central Italy), Palaeogeogr. Palaeocl., 426, 319–333, https://doi.org/10.1016/j.palaeo.2015.03.009, 2015.

Sabatino, N., Ferraro, S., Coccioni, R., Bonsignore, M., del Core, M., Tancredi, V., and Sprovieri, M.: Mercury anomalies in upper Aptian-lower Albian sediments from the Tethys realm, Palaeogeogr. Palaeocl., 495, 163–170, https://doi.org/10.1016/j.palaeo.2018.01.008, 2018.

Satolli, S., Besse, J., Speranza, F., and Calamita, F.: The 125–150 Ma high-resolution Apparent Polar Wander Path for Adria from magnetostratigraphic sections in Umbria-Marche (Northern Apennines, Italy): Timing and duration of the global Jurassic-Cretaceous hairpin turn, Earth Planet. Sc. Lett., 257, 329–342, https://doi.org/10.1016/j.epsl.2007.03.009, 2008.

Schaller, H.: Revisão estratigráfica da Bacia de Sergipe/Alagoas, Boletim Técnico da Petrobras, 12, 21–86, 1969.

Sibuet, J.-C., Hay, W. W., Prunier, A., Montadert, L., Hinz, K., and Fritsch, J.: Early evolution of the South Atlantic Ocean: role of the rifting episode, in: Initial Reports of the Deep Sea Drilling Project, edited by: Hay, J. C. and Sibuet, W. H., U.S. Government Printing Office, Washington, USA, 469–481, https://doi.org/10.2973/dsdp.proc.75.107.1984, 1984.

Silva Jr., R., de Moraes Rios-Netto, A., Silva, S. C., Valle, B., Borghi, L., and Abbots-Queiroz, F.: Middle Cretaceous calcareous nannofossils from the cored well UFRJ-2-LRJ-01-SE, Sergipe-Alagoas Basin, Brazil: New biostratigraphy and paleobiogeographic inferences, Cretaceous Res., 106, https://doi.org/10.1016/j.cretres.2019.104245, 2020.

Siqueira, M. H. Z. R.: Amonóides da transição Aptiano-Albiano da Bacia de Sergipe, Brasil, PhD Thesis, Universidade Federal da Bahia, Salvador, 165 pp., 2005.

Tarduno, J. A.: Brief reversed polarity interval during the Cretaceous Normal Polarity Superchron, Geology, 18, 683–686, https://doi.org/10.1130/0091-7613(1990)018<0683:BRPIDT>2.3.CO;2, 1990.

Tarduno, J. A., Cottrell, R. D., and Smirnov, A. V.: High Geomagnetic Intensity during the Mid-Cretaceous from Thellier analyses of single plagioclase crystals, Science, 291, 1779–1783, https://doi.org/10.1126/science.1057519, 2001.

Torsvik, T. H., Rousse, S., Labails, C., and Smethurst, M. A.: A new scheme for the opening of the South Atlantic Ocean and the dissection of an Aptian salt basin, Geophys. J. Int., 177, 1315–1333, https://doi.org/10.1111/j.1365-246X.2009.04137.x, 2009.

Valle, B., Dal'Bó, P. F. F., Mendes, M., Favoreto, J., Rigueti, A. L., Borghi, L., and Silva, R.: Stratigraphic evolution of a Brazilian carbonate platform during the Cretaceous: the late Albian–early Turonian of the Sergipe–Alagoas Basin, Facies, 65, 1–17, https://doi.org/10.1007/s10347-018-0543-2, 2019.

Zijderveld, J. D. A.: AC demagnetization of rocks: Analysis of results, in: Methods in Palaeomagnetism, edited by: Runcorn, S. K., Creer, K. M., and Collinson, D. W., Elsevier, New York, USA, 254–286, 1967.

Scientific Drilling
Open Access

Composite development and stratigraphy of the Onepoto maar lake sediment sequence (Auckland Volcanic Field, New Zealand)

Benjamin Läuchli[1]**, Paul Christian Augustinus**[1]**, Leonie Peti**[1]**, and Jenni Louise Hopkins**[2]

[1]School of Environment, The University of Auckland, Private Bag 920129, Auckland 1142, New Zealand
[2]School of Geography, Environment and Earth Sciences, Victoria University of Wellington, P.O. Box 600, Wellington 6140, New Zealand

Correspondence: Benjamin Läuchli (bluc030@aucklanduni.ac.nz)

Abstract. The accurate and precise reconstruction of Quaternary climate as well as the events that punctuate it is an important driver of the study of lake sediment archives. However, until recently lake sediment-based palaeoclimate reconstructions have largely concentrated on Northern Hemisphere lake sequences due to a scarcity of continuous and high-resolution lake sediment sequences from the Southern Hemisphere, especially from the southern mid-latitudes. In this context, the deep maar lakes of the Auckland Volcanic Field of northern New Zealand are significant as several contain continuous and well-laminated sediment sequences. Onepoto Basin potentially contains the longest temporal lake sediment record from the Auckland Volcanic Field (AVF), spanning from Marine Isotope Stage 6e (MIS 6e) to the early Holocene when lacustrine sedimentation was terminated by marine breach of the south-western crater tuff ring associated with post-glacial sea-level rise. The Onepoto record consists of two new, overlapping cores spanning ca. 73 m combined with archive material in a complete composite stratigraphy. Tephrochronology and ^{14}C dating provide the fundamental chronological framework for the core, with magnetic relative palaeo-intensity variability downcore, and meteoric ^{10}Be influx into the palaeo-olake to refine the chronology. The µ-XRF (micro X-ray fluorescence) downcore variability for the entirety of the lake sediment sequence has been established with measurement of a range of proxies for climate currently underway. This work will produce the first continuous record of the last 200 kyr of palaeoclimate from northern New Zealand to date.

1 Introduction

Deep-lake sediment archives allow for the development of a more comprehensive interpretation of past climatic and environmental evolution during the Quaternary than other continental climate archives, such as tree rings, peat bogs, and speleothems, and are often less prone to hiatuses than loess and fluvial deposits (Zolitschka and Enters, 2009). Sediments deposited in maar lakes often record regional climate signals due to the typically funnel-shaped crater structure of the maars and absence of major inlets and outlets (e.g., Marchetto et al., 2015), thereby minimising the flux of allochthonous sediment and other material into the lake basin (e.g., Brauer et al., 1999; Augustinus et al., 2011; Sandiford

et al., 2003; Zolitschka et al., 2013). In contrast to the Northern Hemisphere where long, high-resolution late Quaternary terrestrial palaeoclimate archives are common and are well studied (e.g., the Eifel maar lakes in Germany; Sirocko et al., 2016), their New Zealand lake counterparts are few, often show poor resolution, and suffer from age controversies (e.g., Molloy et al., 2009; Hopkins et al., 2017). The Auckland maar lakes are crucial in the context of the Southern Hemisphere mid-latitudes as they contain archives representative of past south-western Pacific climate variability (Alloway et al., 2007). Furthermore, the location of Auckland is ideal for palaeoclimate studies, since it is located at the ecological boundary between the subtropical northern tip of New

Zealand's North Island and the cooler central North Island as well as regions further south (Augustinus et al., 2012).

The maar lakes of the Auckland Volcanic Field (AVF) provide long, continuous, high-resolution (decadal to sub-decadal), high-quality, laminated sediment records suitable for detailed examination of south-west Pacific palaeoclimate over the last 200 kyr (Hopkins et al., 2017). Lacustrine sequences of comparable continuity and resolution are rarely encountered in the terrestrial mid-latitudes of the Southern Hemisphere and tend to cover shorter timescales. Furthermore, many distinct tephra layers from local basaltic activity (e.g., AVF) or rhyolitic and andesitic volcanic centres (VCs) further afield (e.g., Taupo Volcanic Zone (TVZ), Egmont/Taranaki Volcanic Centre (TaVC)) are preserved in these lacustrine archives (e.g., Shane and Hoverd, 2002; Molloy et al., 2009; Hopkins et al., 2015) and form isochronous markers for stratigraphic correlation to other maar lake sediment sequences (Molloy et al., 2009). In particular, a number of independently dated rhyolitic tephra allow for well-established age control for the past ca. 45 kyr (Danišík et al., 2012). Pre-45 ka ages, of the rhyolitic, andesitic, and basaltic tephra, are often not well constrained, with their age estimates in many cases relying on interpolation from sedimentation rates between known-age TVZ-sourced rhyolitic tephra and correlation with the source volcanoes (Molloy et al., 2009; Lindsay et al., 2011; Peti and Augustinus, 2019). Furthermore, a range of proximal basaltic tephra (correlated to their source centres in the AVF) also provide additional age markers within the cores (Hopkins et al., 2017, 2020; Leonard et al., 2017).

Here we present a palaeolake sediment record from Onepoto maar that provides one of the few known opportunities for the identification of climatically forced environmental changes from the Southern Hemisphere mid-latitudes spanning much of the last ca. 200 kyr (Hopkins et al., 2017). This report (1) details the approach used to construct a new robust composite stratigraphy for the Onepoto Basin lacustrine sequence and (2) highlights the potential of the Onepoto sediment sequence for investigation of how Southern Hemisphere and inter-hemispheric climate dynamics are linked at high-precision over the last two glacial cycles.

2 Study site

The maar studied here is located on modern-day Auckland's North Shore (Fig. 1d) and is the product of an explosive phreatomagmatic eruption that is proposed to have occurred not long after the formation of adjoining Lake Pupuke maar (mean age 193.2 ± 2.8 ka by ^{40}Ar / ^{39}Ar dating; Leonard et al., 2017) based on morphostratigraphy (Hopkins et al., 2017). However, ^{39}Ar–^{40}Ar dating of basaltic lapilli attributed to the formative eruption of Onepoto maar indicates that the age of maar formation may be as old as 245 ± 40 ka (Sandiford et al., 2003; Shane and Sandiford, 2003). After

the formative phreatomagmatic eruption, a freshwater lake developed in the maar fed by groundwater seepage and precipitation runoff from the crater rim. The maar lake persisted until an early Holocene sea-level rise breached the south-western crater tuff ring, transforming the basin into an estuarine lagoon ca. 9.0 ka cal BP (Hägg and Augustinus, 2003; Hayward et al., 2008; Augustinus et al., 2011). The present-day Onepoto Basin (Fig. 1a) is occupied by a mixture of recreational parklands and wetlands whilst the surrounding tuff ring is densely covered with residential housing. The drill core presented in this study was recovered in 2018 from a central section of the crater in an area of profundal sedimentation based on previous exploratory drilling (Fig. 1a; Hägg and Augustinus, 2003; Augustinus et al., 2012).

3 Methods

3.1 Coring

A first scientific drilling campaign at Onepoto Basin in the years 2001/2002 produced a continuous lake sediment sequence to a depth of ∼ 60 m below the surface. This initial work produced a scientific drilling report (Hägg and Augustinus, 2003) and further publications (e.g., Shane and Hoverd, 2002; Shane and Sandiford, 2003; Augustinus et al., 2011, 2012). In 2011, another attempt to extract a complete sequence of lake sediment infill from the Onepoto maar crater was undertaken to refine the incomplete tephra record contained in Shane and Hoverd (2002) and Molloy et al. (2009). However, core disturbance and loss during extraction did not allow for the development of a complete sediment sequence. Consequently, a new drilling campaign occurred in October/November 2018 and recovered a minimally disturbed and overlapping sedimentary sequence via two adjacent cores that spanned the complete lacustrine sequence. The locations of all coring sites are given in Fig. 1a.

The drilling was undertaken using a Fraste XL 170 Duo mobile-drilling rig (rotary and sonic capable). Due to the soft nature of the sediments, the sonic function of the drilling rig was initially used to ensure the recovery of undisturbed lake sediment core segments. However, issues were encountered when drilling through the wet expansive muds/clays while operating the drill rig in the sonic mode. Better drilling progress was made (and a higher recovery rate of undisturbed core samples achieved) by simply operating the rig with its standard rotary function. The rig was set up near the centre of the Onepoto domain (Fig. 1a; degree–minute–second (DMS) coordinates: 36°48′30″ S, 174°45′1″ E), corresponding to the depocentre of the maar crater defined from gravity and magnetic surveys (Nunns and Hochstein, 2019). A set of two overlapping cores (A and B cores) with 50 cm vertical and 4 m lateral offset between them was collected in 1.5 and 2 m long barrels, both with an internal diameter of 80 mm. The filled core barrels were brought to the surface, and the sediments extruded into split PVC tubes. The upper 40 m

Figure 1. (a) Aerial photograph of the Onepoto domain study site with location of recent (2018; DMS coordinates: 36°48′30″ S, 174°45′1″ E; source from the LINZ Data Service and licensed for reuse under Creative Commons Attribution 4.0 New Zealand licence) and previous (2001–2002/2011) coring episodes (aerial footage sourced from the LINZ Data Service and licensed for reuse under the Creative Commons Attribute 4.0 New Zealand licence). **(b)** Overview of the North Island and South Island of New Zealand. **(c)** The North Island of New Zealand with its major volcanic centres. **(d)** The Auckland region with the location of significant maars that formed freshwater lakes in the AVF highlighted in blue.

of the overall sedimentary sequence consisted of estuarine mud of which ∼ 39 m was washed out before retrieving the underlying target laminated lake sediments ∼ 1 m above the marine–freshwater transition. Before the laminated lake sediment extraction was initiated, the boreholes were cased to prevent borehole closure during the deeper drilling. A maximum drilling depth of 73.2 m was achieved. However, the basalt lava encountered at the base of the core during the 2011 coring was not reached due to high water pressures at depth which prevented further drilling progress.

3.2 Core description and visual facies identification

The core sections were logged immediately after core splitting during preparation of the individual half core segments for X-ray-density and μ-XRF (micro X-ray fluorescence) core scanning. All core surfaces were logged in a field-moist state (examples of representative core sections are given in Fig. 5) and described visually with regards to thickness and shape of laminations and sedimentary banding, sediment colour (Munsell Soil Color Chart 1992), approximated grain size (clay, silt, fine to coarse sand), bioturbation, macroscopic plant fragments, charcoal content, vivianite, volcanic ash layers (tephra), and visible disturbance of sedimentary struc-

tures. Most lithostratigraphic units were identified following conventional methods and often exhibit distinct contacts between units. Individual units contain sediments of similar colour and character as well as the presence of laminations in some cases. Identified sub-units differentiate between intervals of smaller differences in colour, composition as well as the presence, quality, and thickness of laminations and bands.

3.3 μ-XRF core scanning and low-field volumetric magnetic susceptibility

The sediment cores were scanned with an Itrax μ-XRF core scanner (Cox Analytical Systems, Sweden) at the School of Environment, The University of Auckland, New Zealand. The approach of μ-XRF core scanning involves very little sample preparation and is nondestructive (Croudace et al., 2006; Croudace and Rothwell, 2015). To establish a downcore record of elemental variability, measurements were taken at 1 mm increments with 10 s exposure time per measurement point. Both Mo (at 30 kV, 55 mA) and Cr tubes (at 60 kV, 30 mA) were used as X-ray sources to achieve an excitation of the full range of detectable elements (Mg (by Cr tube) and Al–U) with both increased detection precision for heavier (Mo tube = $Z \geq 26$) as well as lighter elements

(Cr tube $= Z \le 26$; Jarvis et al., 2015; St.-Onge et al., 2007). Additionally, high-resolution optical images (47 µm) and radiographic images (at 60 kV, 50 mA; at 1 mm) were also produced during the scanning process. Supplementary high-resolution radiographic images (0.2 mm resolution) were obtained with the aim to reveal sedimentary layers and grains, fine tephra beds and to identify pieces of wood/bark or seeds for ^{14}C dating (Croudace et al., 2006; Francus et al., 2009; Croudace and Rothwell, 2015). Low-field volumetric magnetic susceptibility was recorded for all cores with a hand-held Bartington MS2 with a MS2e surface scanning sensor system at 5 mm increments and the range scale set to 0.1. Core sections from the 2011 campaign were also scanned with the Itrax µ-XRF elemental core scanner using a Mo tube (at 30 kV, 55 mA) to facilitate correlation with the new 2018 sequence. XRF data were acquired by following the same method as for the 2018 cores.

3.4 Tephra identification based on geochemical fingerprinting

Eighty five out of the identified 89 tephra horizons were sampled for geochemical fingerprinting from the newly obtained sediment cores and sieved (mesh size $= 36$ µm) under distilled water at The University of Auckland (New Zealand). Further sample preparation and the analysis itself on an electron micro-probe analyser (EMPA) were conducted at Victoria University of Wellington (New Zealand). Each sample was poured into a hole of a mount and then filled with epoxy resin. Afterwards, the pugs were thoroughly shaken to remove air bubbles before being left to cure. Once fully solidified, the bottom side of the samples was polished stepwise to expose fresh glass shard surfaces. The quality of the polished surface and its cleanliness were checked under the microscope. In a final step the individual pugs were carbon coated. The geochemical analyses were run using a JEOL JXA 8230 Superprobe using the following instrument settings: 15 kV acceleration voltage and ~ 8 nA beam current for glass analysis. Matrix-matched standard A99 basaltic glass was used as a bracketing standard, while for rhyolitic and intermediate glass samples VG-568 was used. To avoid instrument drift, standards were run every 20 samples.

3.5 Radiocarbon dating

The ^{14}C age determinations were carried out on seven bulk sediment samples. Preparation for the analysis involved physical pre-treatment (sample drying, gentle break up, transferred to a centrifuge tube and weighed on a balance) at The University of Auckland (New Zealand) and several steps of standard chemical pre-treatment of organic samples from sediments (first HCl acid washing, NaOH alkali treatment and final HCl acid treatment) at ANSTO (Australian Nuclear Science and Technology Organisation, Sydney, Australia). The analyses were undertaken at the ANTARES AMS

(accelerator mass spectrometry) facility at ANSTO following the procedure outlined in Fink et al. (2004). Rbacon (version 2.4.3; Blaauw and Christen, 2011) in R (version 1.3.1073; R Core Team, 2020) was used to calibrate AMS ^{14}C ages using the latest SHCal20 calibration (Hogg et al., 2020) and for construction of the preliminary age model.

3.6 Composite stratigraphy development and core chronology

The 2018 A and B core segments were correlated using guidelines outlined in Peti and Augustinus (2019). Initial core section matching was guided by the vertical offset (here 0.5 m) between cores A and B, with the marine–freshwater transition (M/F) used as a top-of-core reference horizon to enable comparison to previous work at Onepoto Basin (e.g., Augustinus et al., 2011, 2012). Core matching was mainly achieved using the following:

1. Geochemical fingerprinting and correlation of tephra layers,

2. Comparison of high-resolution optical and X-ray density images,

3. Correlation of magnetic susceptibility and µ-XRF data (Ti normalised against inc+coh; with a Mo tube as X-ray source).

Figure 2 provides a depiction of core section alignment using high-resolution optical images, Itrax µ-XRF and low-field volumetric magnetic susceptibility data.

Due to the proximity of the A and B core drill sites (~ 4 m), marker layers, such as tephra layers, mass movement deposits, distinct segments with well-laminated sediments, and features representative for individual lithostratigraphic units, were generally encountered in the overlapping core sections. However, a tendency for an increased variability in thickness of sedimentary features between the A and B cores was noted at depths >46 m. This is in accordance with previous studies which have found that even in close-proximity cores from deep maar lake basin environments, corresponding sedimentary features can differ in thickness between adjacent cores (e.g., Peti and Augustinus, 2019; Poth and Negendank, 1993; Williams et al., 1993). Core segments expanded significantly after extraction and removal of the sediment overburden, especially where the segments were dominated by soft, organic-rich mud. To correct for this, the specific core segments were compressed by a factor equivalent to the amount of expansion (range of expansion in certain cases up to 30–50 cm), with the drill rod length (1.5 or 2 m) being the measure. Table S1 in the Supplement provides an overview on the amount of expansion and adjusted depths for the composite record build. The relative positions of related data points (e.g., loss-on-ignition, sediment carbon/nitrogen and stable isotope content, biomarker, and pollen sampling) have been recalculated accordingly.
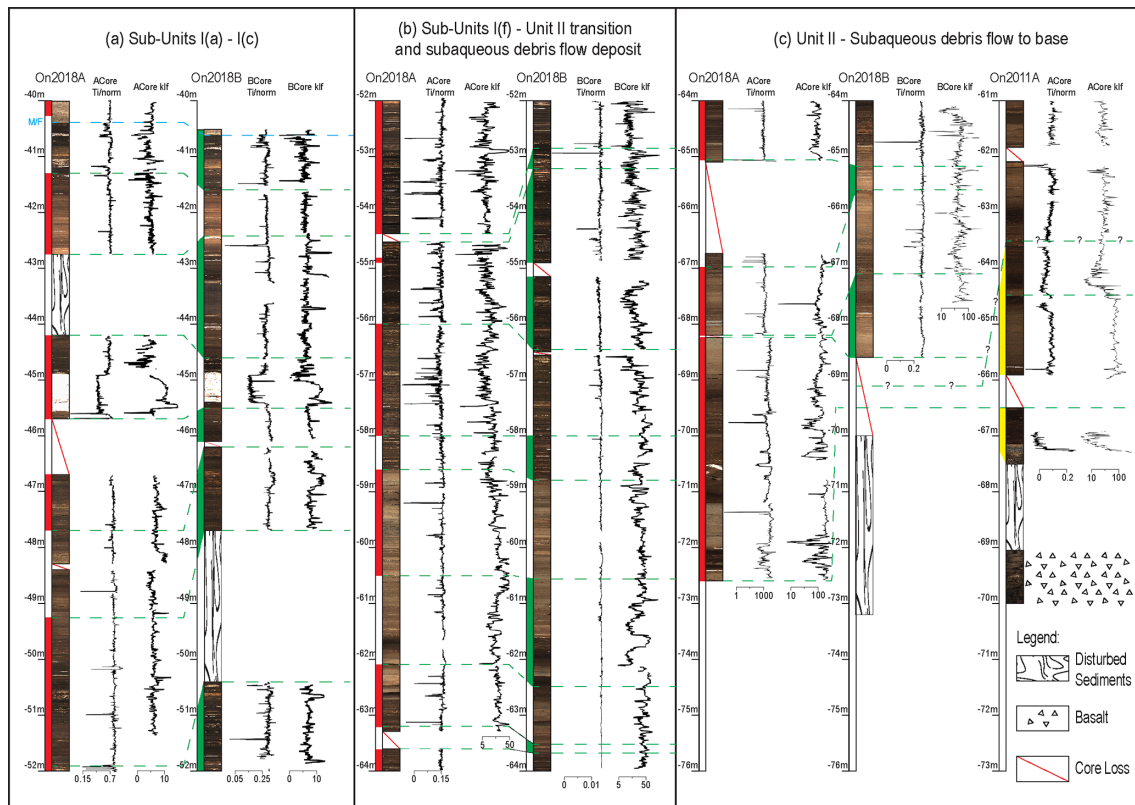
Figure 2. Schematic depiction of core section alignment using high-resolution optical images, Itrax µ-XRF Ti/norm., and low-field volumetric magnetic susceptibility (klf) data (dimensionless Si units $\times 10^{-5}$). Red highlights the 2018 core A (ACore) sample chosen for composite; green highlights the 2018 core B (BCore) sample chosen for composite; and yellow highlights the 2011 core A archive material chosen for composite. Symbol * represents normalisation with inc+coh to correct for variability in water and organic matter content, grain size, and ageing of the X-ray tube (Löwemark et al., 2011; Kylander et al., 2012).

A complete composite record that spans the entire lacustrine sequence was established by linking the A and B cores from the 2018 drilling with archive core material from the 2011 coring campaign. An event-corrected depth scale (ECD) was established by removal of all identified instantaneous event deposits (89 primary tephra and 211 mass movement deposits: total thickness of tephra and mass movement layers of ~ 6.90 m). Mass influx material could usually be identified visually or using the radiographic images. If not already visually distinct, tephra layers were identified through a combination of magnetic susceptibility measurements (e.g., increased Fe content (magnetite) in basaltic tephra), µ-XRF core scanning (Si and Sr were found to be the most reliable elements for rhyolitic tephra layer identification) and X-ray density images.

4 Results and discussion

4.1 Lithostratigraphic units

The laminated lake sediments are overlain by ~ 40 m of estuarine muds (see Figs. 3 and 4). A general lithostratigraphic model for the laminated lacustrine sequence was produced by Hägg and Augustinus (2003) from a single and incomplete core retrieved ca. 200 m east of the crater centre (Fig. 1). In general, the existing lithostratigraphic model could be transferred to the 2018 sequence, with individual unit boundaries usually encountered at similar depths. Detailed descriptions of the individual units are provided in Table 1 and are depicted in Fig. 3. The sequence was divided into two main units and six individual sub-units for Unit I. However, the underlying Unit II could not easily be subdivided into individual sub-units during logging due to the lack of clear transitions from one facies type to the next and frequent disruption of the sequence by mass-wasting deposits. Furthermore, Unit II differs from Unit I in containing many mass movement deposits (centimetre- to metre-scale thickness) and inwashed organic detritus that was only found sporadically in sub-units I(e) and I(f). A sharp contact that would mark the transition from Unit I to Unit II could not be identified. In our model an approximated boundary was defined based on the onset of increased presence of coarse sand to gravel-rich layers. The main difference between the 2001/02 and 2018 records lies in facies Unit II being 10.45 m thicker in the

2018 core collected at the centre of the maar lake. This indicates that the bulk of mass movement material transported into the basin accumulated in the depocentre of the basin. A cross-section of the crater established based on the results of all three coring campaigns confirms a nearly bowl-shaped geometry (Fig. 4) for the crater as proposed by Nunns and Hochstein (2019). However, a reported primary estimate of 63 m for the depth of crater infill (Nunns and Hochstein, 2019) is not supported by the coring results produced from the recent 2011 and 2018 drill holes from which we deduce an overall thickness of 73.2 m. For the newly established composite record presented here, we rule out doubling up of core segments as a reason for the significant difference in length between the two cores while building the new composite sedimentary sequence since the preserved sedimentary features, when combined with the µ-XRF and magnetic susceptibility data, allow for straightforward core correlation. Furthermore, a comparison of the overall thickness of the lacustrine sequence as recorded in the 2011 and the new 2018 cores shows a ∼ 5 m difference (2011 core of ∼ 31 m vs. newly established composite record of ∼ 36 m), which could be related to technical issues and core loss during the 2011 drilling campaign.

4.2 Tephra identification

Eleven rhyolitic (Rotoma, Waiohau, Rotorua, Rerewhakaaitu, Okareka, Kawakawa/Oruanui, Okaia, Hauparu, Maketu, Tahuna, and Rotoehu) and one andesitic tephra (Eg4) were identified based on geochemical fingerprinting. The identification of these tephra layers (and their correlation to the formative eruptive events), is supported by the geochemical composition of the glass shards contained in the individual tephra as well as their relative stratigraphic position to the tephrochronological frameworks in Shane and Hoverd (2002) and Molloy et al. (2009). Reported average deposit thicknesses were also often referred to for additional supportive evidence. Major-element oxide bivariate plots of reference tephra data and rhyolitic tephra glass shards presented here are depicted in Fig. 6. This has allowed for a direct transfer of published ages onto the Onepoto lake sediment sequence. The corresponding glass analysis data are provided in Table S2 of the Supplement. Figure 7a to c depict how well the EMPA geochemistry for the probed rhyolitic tephra overlap with the glass-based reference data available from Molloy (2008) and reflect the expected geochemistry of the eruptive centres from which the individual tephra beds originate, analogues to the descriptions in Molloy et al. (2009). Furthermore, EMPA geochemistry for Eg4 is plotted in Fig. 7d–f. The stratigraphic position and geochemical composition of the targeted bed in the new Onepoto record assigned to Eg4 by us matches most with the corresponding Eg4 bed assigned by Molloy et al. (2009). A comparison to the next stratigraphically closest Egmont/Taranaki sourced tephra, Eg3, resulted in

a non-conclusive overlap and a less robust stratigraphic cross-correlation. Additionally, three AVF-sourced basaltic deposits (AVF B, AVF C and AVF D) have been assigned based on stratigraphic position relative to the established AVF tephrochronology (Hopkins et al., 2015; Molloy et al., 2009), whereas the vertical position of AVF 1 recently calculated to 90.435 ± 1.555 ka cal BP (Peti et al., 2021) to date could not be reliably identified. The latter, however, is subject of further investigation by applying klf and µ-XRF downcore variability data trends matching from relevant sections of the Onepoto and the Orakei record. All assigned eruptive events with ages are summarised in Table 2.

4.3 Radiocarbon dating

All seven radiocarbon ages obtained from the Onepoto core on bulk organic matter are summarised in Table 3. Terrestrial macro-organic remains, which are commonly more preferable for ^{14}C dating, were not available from the <50 ka part of the record. The study therefore had to resort to bulk organic matter for this approach. As influx of old organics from eroded soils, mobilised from the crater rim, is limited for the later phase of the lake's existence, we expect the results of the AMS radiocarbon age dating from bulk organic matter to be adequate. Furthermore, due to the lack of carbonates in the catchment, any distortion due to a hard water effect is unlikely.

4.4 Age–depth model based on the tephrochronology and radiocarbon ages

An updated age model for the Onepoto lake sequence (Fig. 7) has been established that relies on the identification of 11 known-age rhyolitic tephra beds (ca. 9–ca. 50 ka) with sufficiently distinct geochemistry and AMS radiocarbon ages obtained from the core on bulk organic matter. The presence of the 11 rhyolitic tephra deposits with reliable ages in tight succession help to constrain the resulting ^{14}C ages. For the >50 ka part of the record, the andesitic "Eg4" tephra (77.165 ± 1.5 ka; Peti et al., 2021) allows for correlation with the newly refined Orakei maar crater lake sediment record (Peti and Augustinus, 2019; Peti et al., 2020). Basaltic ejecta dating back to the early stages of Onepoto maar lake formation (AVF D) are used as age tie points (AVF B, 146.9 ± 2.8 ka; Hopkins et al., 2017; Leonard et al., 2017; AVF C, estimated age 181 ± 0.6 ka; Hopkins et al., 2017). The age of maar formation is currently proposed to have occurred >150 ka and <193 ka (Hopkins et al., 2017; Leonard et al., 2017) but may be as old as 245 ± 40 ka based on ^{39}Ar–^{40}Ar dating of basaltic lapilli attributed to the formative eruption (Sandiford et al., 2003; Shane and Sandiford, 2003). Based on the available evidence, we consider the latter age to be problematic and have thus only included the former in our age model. For the younger age, we use the established mean age of formation of adjacent Lake Pupuke

Figure 3. Onepoto maar palaeolake composite stratigraphy, lithological descriptions, and tephra marker layers. Tephra abbreviations: Rm = Rotoma; Wh = Waiohau; Rr = Rotorua; Rw = Rerewhakaaitu; Ok = Okareka; Kk = Kawkawa/Oruanui; Op = Opepe; AVF 12, AVF 10, AVF 7 = basaltic tephra, AVF sourced (Molloy et al., 2009); O = Okaia; Mk = Maketu; Ta = Tahuna; OVC1 = rhyolitic tephra, Okataina Volcanic Centre sourced (Molloy et al., 2009); Re = Rotoehu; An = andesitic tephra. Detailed lithostratigraphic descriptions are provided in Table S1 of the Supplement.
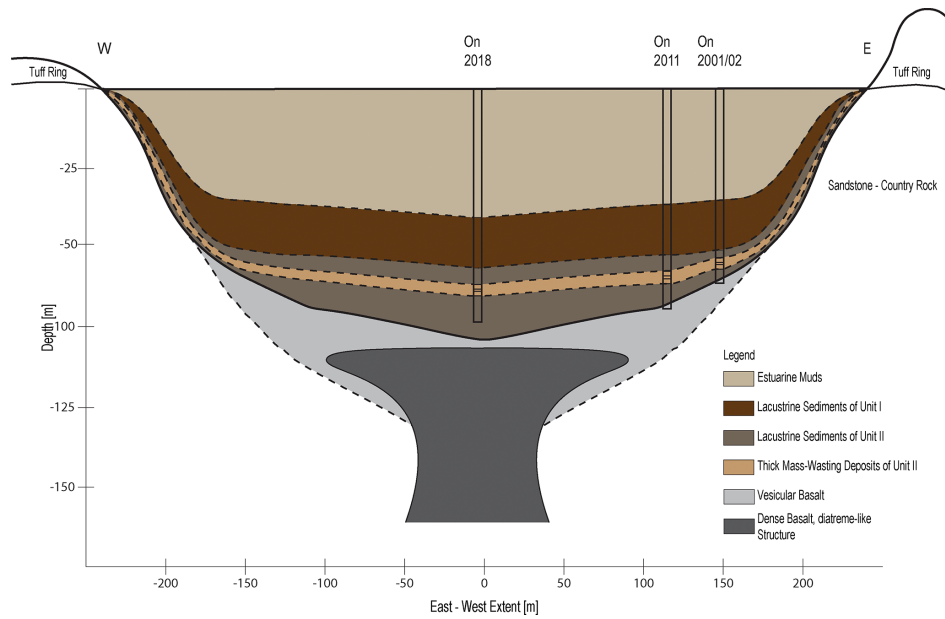
Figure 4. Cross-section of the crater and its infill. Extent and position of diatreme-like structure under the crater and vesicular basalt at depth guided by descriptions in Nunns and Hochstein (2019) as well as drill core findings (On2011, On2001/02) for the latter. Thickness and lateral extent of major lithostratigraphic units taken or estimate based on drill core findings (On2018, On2011, and On2001/02).
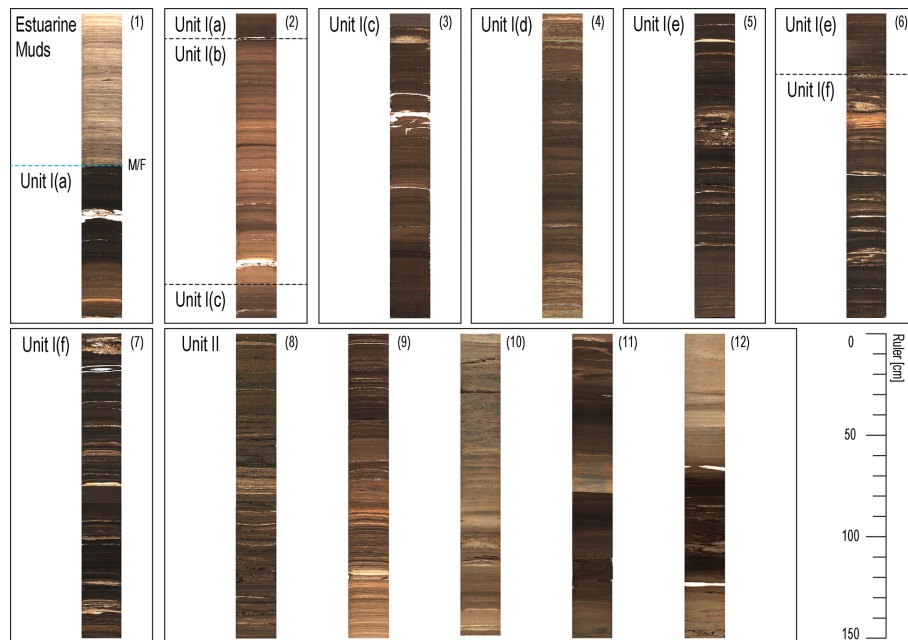

Figure 5. High-resolution core section images representative of the main facies units (Unit I and Unit II) as well as the six sub-units of Unit I (I(a) to I(e)). The depicted core images are ca. 1.5 m long. An = andesitic tephra, B = basaltic tephra, Rh = rhyolitic tephra. (1) Transition from estuarine muds to Unit I(a); (2) transition from Unit I(a) over Unit I(b) to Unit I(c); (3) sediments of Unit I(c); (4) sediments of Unit I(d); (5) sediments of Unit I(e) with moderately developed laminations, occasional lighter and darker coloured bands; (6) transition from Unit I(e) to Unit (f) with coarser grained mass-waste deposits and their finer, orange-coloured gritty bands. (7) Sediments of Unit I(f) with coarse-grained (centimetre-scale) mass-waste deposits, fine, orange-coloured gritty bands, and centimetre-scale vivianite nodule bracketed by andesitic tephra (see top of core section); (8) well-developed laminations of Unit II; (9) well-developed laminations with decreasing quality downcore; (10) weathered basaltic detritus in Unit II; (11) subaqueous debris flow deposit Unit II; and (12) rhyolitic tephra ca. 2 m above the core base.
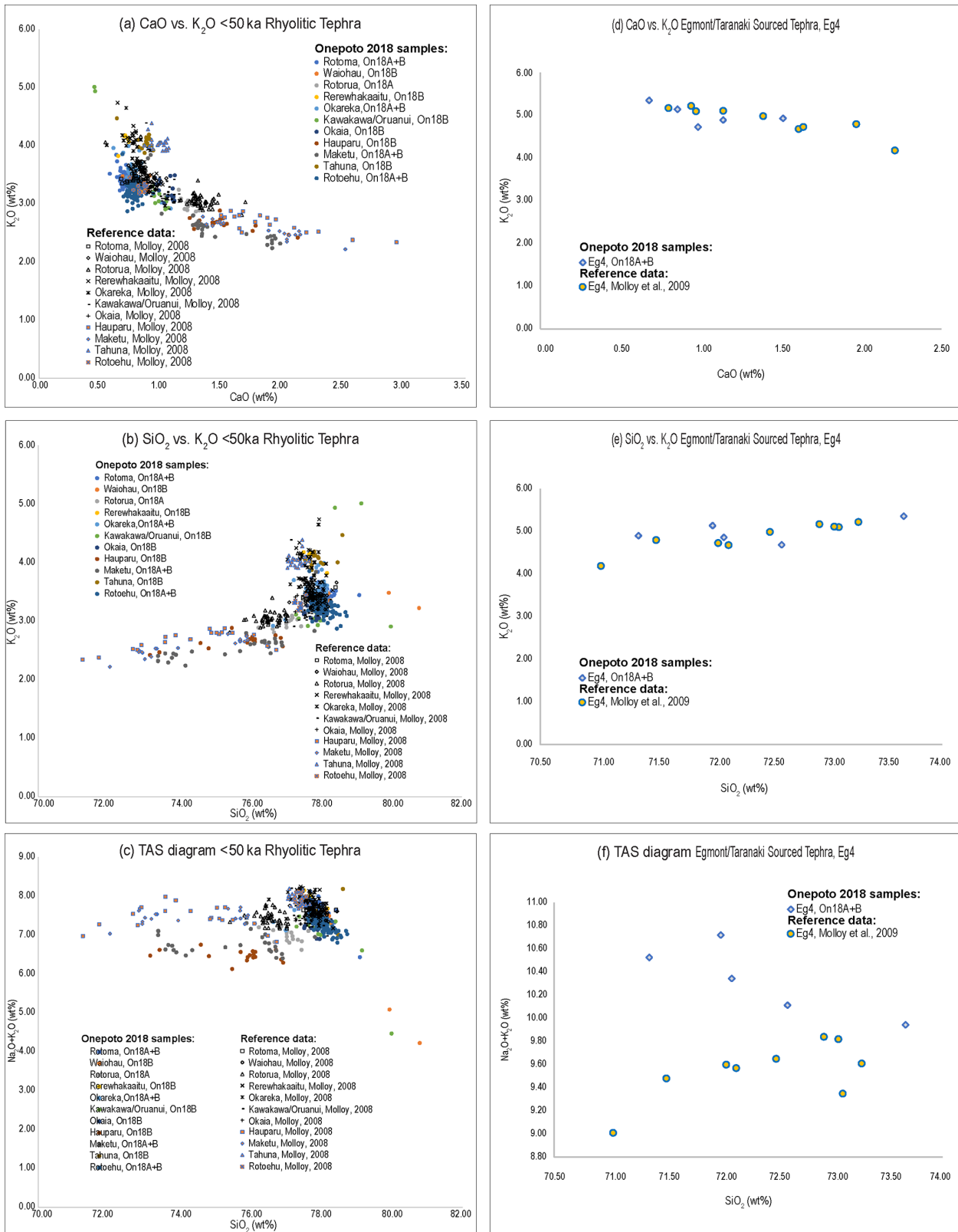
Figure 6. Glass shard major-element oxide bivariate plots of reference glass tephra data (taken from Molloy, 2008) and Onepoto (2018 drilling) samples.

Table 1. Description of the lithostratigraphic units for the 2018 Onepoto composite record based on the naming convention defined by Hägg and Augustinus, 2003. ECD represents event-corrected depth.

Lithostratigraphic unit	Depths below marine–freshwater transition (M/F) [m]	ECD [m]	Description
Unit I – Sub-Unit I(a)	0.0–1.5	0.0–ca. 1.2	Silts deposited prior to marine breach. Mainly dark brown to black, with well-developed laminations (sub-millimetre) and lighter-coloured centimetre-scale bands. A lighter-brown to greyish-brown section is present from 0.42–0.69 m M/F.
Unit I – Sub-Unit I(b)	1.5–2.7	ca. 1.2–2.5	Silts of dark grey to grey, brown colour with moderately developed laminations (sub-millimetre thickness) and bands (1–5 mm thickness).
Unit I – Sub-Unit I(c)	2.70–6.24	ca. 2.5–5.4	Silty clays, dark brown faint bands (1–5 mm thickness), well-developed laminations present (sub-millimetre thickness).
Unit I – Sub-Unit I(d)	6.24–9.34	ca. 5.4–8.16	Silty clays of light brown to light greyish-brown colour with little to no laminations present but gritty fine sand and lighter and darker bands (centimetre scale).
Unit I – Sub-Unit I(e)	9.34–11.38	ca. 8.39–10.18	Clays, dark brown to black, with moderately developed laminations (sub-millimetre thickness) to increasingly well-developed downcore and lighter and darker bands (10–20 mm thick) and occasional ≤ 10 mm thick light brown fine sand bands.
Unit I – Sub-Unit I(f)	11.38–15.72	ca. 10.18–13.38	Very dark brown to black, also abundant light brown to olive coloured and greyish-brown (10–20 mm thick) bands. Fine to medium sand layers are common and well-developed laminations are present (sub-millimetre thickness). Increased plant fragment content and vivianite flecks.
Unit II	15.72–36.12	ca. 13.38–29.47	Silty clays and silts with colours ranging from dark greyish-brown to olive grey and laminations generally poorly to medium well-developed as well as a high content of coarse sand to gravel-rich layers. However, also sections with well-developed laminations present (17.76–19.36 m, 25.73–26.46 m M/F).

maar (193 ± 2.8 ka; Leonard et al., 2017) as minimum age of the suggested >150 ka and <193 ka (Hopkins et al., 2017; Leonard et al., 2017). Tephra and AMS ^{14}C ages are given in Tables 2 and 3. Rbacon (version 2.5.1; Blaauw and Christen, 2011) in R (version 1.3.1103; R Core Team, 2020) was used to calibrate AMS ^{14}C ages using the latest SHCal20 calibration (Hogg et al., 2020) and to construct the age model, using a prior accumulation rate of 100 yr/cm (Fig. 7a) and 50 yr/cm (Fig. 7b) based on a ballpark estimate provided

by Rbacon. Prior accumulation shape, memory strength and memory mean follow the suggestions provided by the Rbacon age model presented in Blaauw and Christen (2011). Revised tephra ages provided by Lowe et al. (2013) and Peti et al. (2021) permit correction of sedimentation rates and inferred ages for non-numerically dated tephra (largely Egmont/Taranaki VC-sourced andesitic tephra) as previously reported by Molloy et al. (2009) and Augustinus et al. (2011). Furthermore, we present a new sedimentation rate model for

Table 2. Rhyolitic and andesitic tephra marker beds and basaltic deposits preserved in the Onepoto lake sediment record with assigned ages. ECD represents event-corrected depth.

Tephra ID	Material	Thickness [mm]	Age [cal BP]	Error (±2σ)	Depth below marine–freshwater transition (M/F) [m]	ECD depth [m]	Age taken from
Rotoma	Rhyolite	50	9423	120	0.23	0.23	Lowe et al. (2013)
Opepe	Rhyolite	5	9991	160	0.32	0.27	Lowe et al. (2013)
Waiohau	Rhyolite	1	14 009	155	0.83	0.78	Lowe et al. (2013)
Rotorua	Rhyolite	35	15 635	412	0.98	0.89	Lowe et al. (2013)
Rerewhakaaitu	Rhyolite	2	17 496	462	1.32	1.23	Lowe et al. (2013)
Okareka	Rhyolite	3	23 525	1390[a]–210	1.96	1.89	Original age from Molloy et al. (2009); calibrated with SHCal20 (Hogg et al., 2020); Peti et al., 2020, 2021)
Kawakawa/Oruanui	Rhyolite	30	25 360	160	2.43	2.3	Vandergoes et al. (2013)
Okaia	Rhyolite	5	28 621	1428	2.81	2.66	Lowe et al. (2013)
Maketu	Rhyolite	20	36 100	900	3.83	3.61	Danišík et al. (2020)
Tahuna	Rhyolite	1	38 400	1700	4.1	3.88	Danišík et al. (2020)
Rotoehu	Rhyolite	720	45 100	3300	5.34	4.51	Danišík et al. (2012)
Eg4	Andesite	5	77 165	1400–1455[b]	7.63	6.76	Peti et al. (2021)
AVF B	Basalt	20	146 900	2800	28.07	22.26	Leonard et al. (2017)
AVF C	Basalt	360	181 000	600	34.82	27.91	Inferred age in Hopkins et al. (2017)
AVF D	Basalt	Bedrock	>150 000 <193 000	2800	36.12	29.47	Hopkins et al. (2017); Leonard et al. (2017)
AVF D (problematic alternative age)	Basalt	Bedrock	245 000	40 000	36.12		Shane and Sandiford (2003)

[a] As Bacon does not allow asymmetrical errors by default for non-radiocarbon dates, a 2σ error of 1390 was used

[b] As Bacon does not allow asymmetrical errors by default for non-radiocarbon dates, a 2σ error of 1455 was used.

Table 3. AMS radiocarbon ages from the Onepoto maar lake sediment record. Ages calibrated against SHCal20 (Hogg et al., 2020) in OxCal version 4.4; (Bronk Ramsey, 2009), with reserved data repository https://doi.org/10.6084/m9.figshare.13683874.

Sample ID	Sample type	Conventional AMS ^{14}C age	δ^{13}C per mil	Error (±1σ)	Age [cal BP]	Error (±2σ)	Depth below M/F [m]	ECD [m]
OZZ288	Bulk sediment	10 340	−28.2	±0.1	12 199	151	0.56	0.51
OZZ273	Bulk sediment	10 860	−29.5	±0.1	12 785	30	0.64	0.59
OZZ274	Bulk sediment	13 890	−28.9	±0.2	16 880	92	1.08	0.99
OZZ278	Bulk sediment	17 200	−20.3	±0.1	20 752	86	1.71	1.62
OZZ280	Bulk sediment	20 050	−22.2	±0.1	24 049	98	2.15	2.05
OZZ281	Bulk sediment	30 430	−28.2	±0.1	34 844	200	2.32	3.45
OZZ283	Bulk sediment	39 710	−27.9	±0.1	43 056	320	4.32	4.10

Onepoto applicable prior to the deposition of the Rotoehu tephra (45.1 ± 3.3 ka; Danišík et al., 2012) and post-AVF C eruption age.

Calculated sedimentation rates seem to support a time of eruption younger than 193 ka. However, the data density for the pre-50 ka record is low, which emphasises the need for further age markers in this part of the sequence. We anticipate that the reconstruction of meteoric ^{10}Be flux into the lake basin proposed by us and U/Th dating on a large (4 × 1 cm) vivianite nodule (Sub-Unit I(f), ca. 13.35 m below M/F transition; estimated age ca. 93 ka based on our age model) will

improve the robustness of the full Onepoto sequence age model.

4.5 Comparison of the Onepoto and Orakei maar lake sediment sequences

The well-preserved, mainly rhyolitic, tephra deposits within the <50 ka segment of the Onepoto palaeolake sequence not only provide an excellent chronological framework for the sequence but also allow for correlation to other long lacustrine records from the AVF (e.g., Orakei Basin and Lake Pupuke; Molloy et al., 2009). While Lake Pupuke's
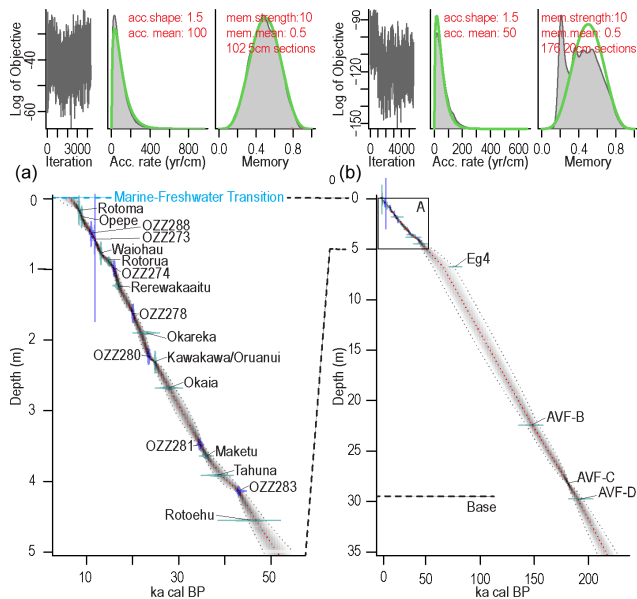
Figure 7. Onepoto lake sediment sequence age model spanning the entire sediment sequence using an event-corrected depth scale established using Rbacon (version 2.5.1; Blaauw and Christen, 2011) in R (version 1.3.1103; R Core Team, 2020). **(a)** Post-50 ka record based on AMS ^{14}C ages and known-age rhyolitic tephra ages (mean 95 % confidence ranges 2.03 ka, min 0.31 ka at 0.59 m, max 6.11 ka at 50 m). **(b)** Full lake sediment sequence including andesitic tephra and basaltic ejecta as age markers in the pre-50 ka part of the record (mean 95 % confidence ranges 13.23 ka, min 0.11 ka at 0.18 m, max 20.85 ka at 10.81 m. The accumulation rate is estimated by Rbacon by millions of Markov Chain Monte Carlo (MCMC) iterations. The memory defines how much the accumulation rate of a particular depth in a core depends on the depth above it (Blaauw and Christen, 2011).

lacustrine sediment sequence has been studied in great detail for the last 50 kyr (e.g., Nilsson et al., 2011; Stephens et al., 2012a, b), a comparison with the palaeolake sediment sequence extracted from nearby Orakei maar (Peti and Augustinus, 2019), however, allows for a correlation of lithostratigraphic units from Onepoto Basin with the high-resolution (averaged SAR (sediment accumulation rate) of 0.04 mm/yr; Peti et al., 2020) terrestrial record from Orakei Basin which spans the last 130 kyr. For the period from 50–9 ka, the correlation of the two records is guided by the presence of well-visible and geochemically distinct rhyolitic tephra beds (Rotorua, Okareka, Kawakawa/Oruanui, Okaia, Maketu, Tahuna, and Rotoehu) and one basaltic tephra deposit (AVF 12). In contrast, for the period from 130–50 ka our correlation is based upon the presence of the andesitic Eg4 tephra in both records and sedimentary characteristics (colour, texture, evidence of influx organic macro material content, and coarse-grained material).

Both maar lakes were subject to the same regional environmental and climatic drivers determining sediment influx

and depositional conditions. Units from the two lake records have been grouped by us to "lithostratigraphic groups" (further referred to as LG) and evaluated as to whether the onset and termination of these units coincide. The correlation of the transitions from one unit to the next relies on a recently established robust age model for Orakei Basin (Peti et al., 2020) and for Onepoto Basin on the age model presented in this study. Correlation of the lithostratigraphic units between the cores is given in Fig. 8.

For LG-1, the lithostratigraphic units at the very top, Unit I(a) (Onepoto) and Unit 1 to Unit 2 (Orakei) show distinct differences with respect to sediment colour, texture, and composition. In both cases their termination is marked by a transition from lacustrine to marine conditions at ca. 9 ka. Unit I(a) is mainly dominated by dark brown to black silts with well-developed laminations (sub-millimetre) and lighter-coloured bands (centimetre scale). Unit 1 and Unit 2 in the Orakei record, on the other hand, are characterised by a transition from light brown massive clay with bioturbation (Unit 2) to peat (Unit 1). This suggests locally varying environmental conditions for the two sites. Onepoto maar lake remained a deep, stratified lake with conditions favouring the development of laminations due to bottom-water/sediment anoxia but with an increased input of fine organic matter until the conclusion of lacustrine conditions (dark colour). On the other hand, Orakei maar lake gradually shallowed over time due to sediment influx, and input of fine organic detritus was reduced. Direct correlation between these units is supported by the presence of Rotorua tephra at ca. 15.64 ka cal BP.

For LG-2, the closest similarities between units of the records are found between Unit I(b) (Onepoto) and units 3 to 7 (Orakei). Both groups share close estimated times of onset (ca. 28 ka) and termination (ca. 18 ka) and are similar in sediment colour and composition. The units in both records are dominated by lighter-coloured sediments with moderately well-developed laminations in both. However, the laminae in the Orakei lacustrine sequence are better defined. These sedimentary characteristics suggest a more stratified water column for Orakei maar lake with bottom-water/sediment anoxia before transitioning into banded sands/silts with wood fragments. The latter indicates a gradual shallowing at this site. Input of fine organic matter is somewhat reduced at Onepoto palaeolake and significantly reduced at Orakei palaeolake. Okareka and Kawakawa/Oruanui (KOT) tephra provide reliable age markers at ca. 22.21 and ca. 25.36 ka cal BP, respectively, that can be correlated across the two records. In addition, in both records an increase in basaltic tephra deposits is noticeable such as AVF 10 and AVF 12. Not only does this reflect heightened volcanic activity within in the AVF at the time but also indicates that both basins were located downwind from the eruptive cones that produced these tephra.

For LG-3, Unit I(c) (Onepoto) and Unit 8 (Orakei) are both constrained by estimated times of onset of ca. 58 ka and termination of ca. 28 ka, respectively. Both lithostrati-
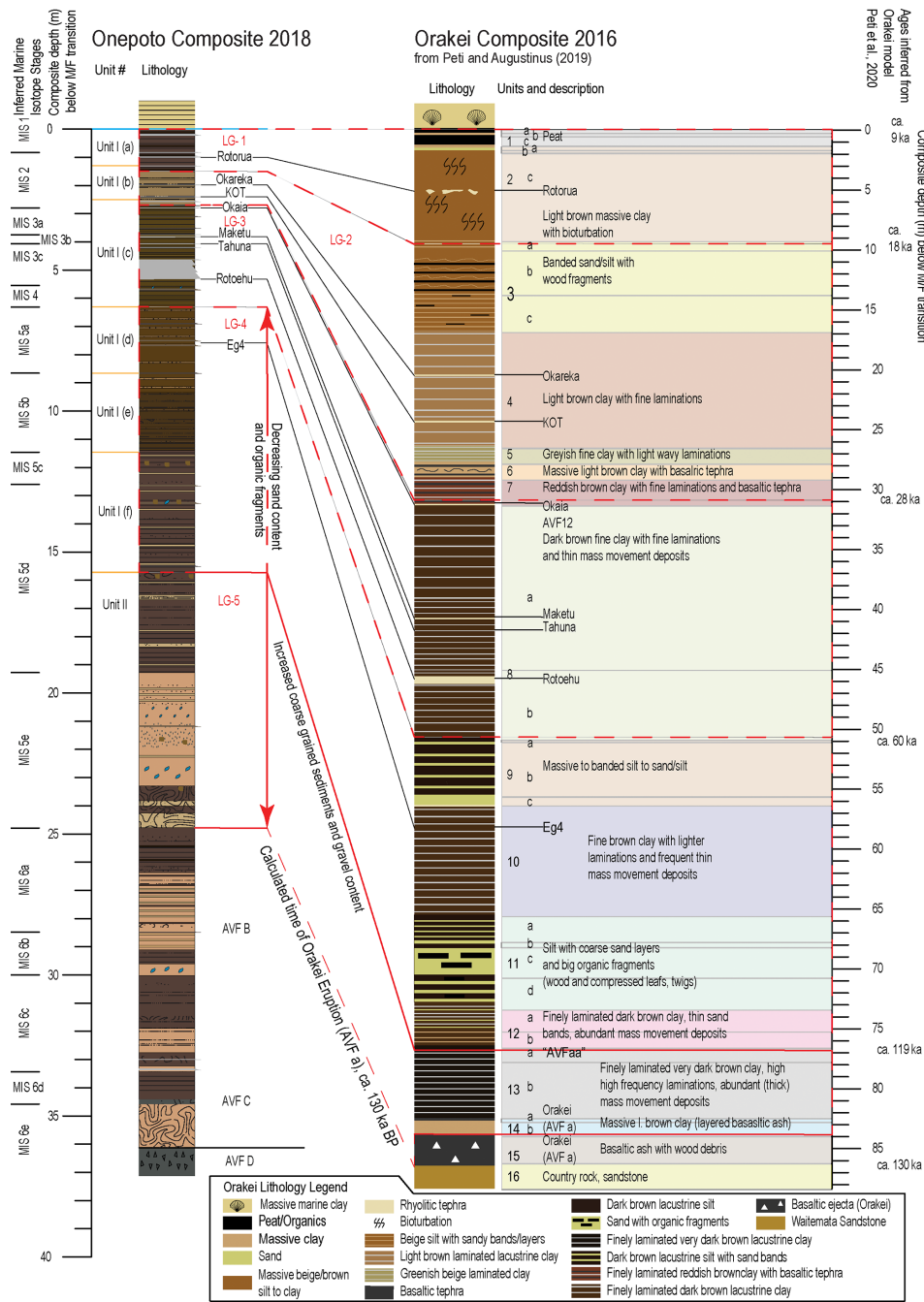
Figure 8. Comparison of lithostratigraphic units identified in the Onepoto and Orakei maar lake records as well as inferred correlations to the MIS 6e–MIS 1 (where MIS represents marine isotope stage). Orakei Basin lake sediment facies model modified from Peti and Augustinus (2019). Lithology legend for Onepoto follows that in Fig. 3. Red dashed lines show corresponding facies transitions; black dashed lines show possibly correlatable tephra beds; red solid lines show transition from sediments with less sandy/coarse content to sediments with increased coarse-grained content; black solid lines show correlatable tephra beds; and the dashed blue line represents the marine–freshwater transition.

graphic units show dark brown, fine-grained sediments with well-developed laminations. While thin, mass-movement deposits are reported for Unit 8, similar features are not found in Unit I(c), with minor traces of macroscopic plant fragments present in the latter. The observed features indicate

mostly comparable environmental conditions for both lakes with water column stratification and bottom-water/sediment anoxia, which allows for the development of well-developed laminations. The dark colouration of the sediments indicates a steady input of fine organic matter into both

lakes. In this case Okaia (ca. 28.62 ka cal BP), Maketu (ca. 35.61 ka cal BP), Tahuna (ca. 37.85 ka cal BP), and Rotoehu (ca. 45.1 ka) tephra offer age dates and are reliable marker layers for a direct correlation between these units.

For LG-4 (between ca. 60 to 119 ka), Onepoto Basin's units I(d) to I(f) share similar characteristics to units 9 to 12 (Orakei). Drawing from the more robust Orakei age model, the onset and termination times can be inferred (ca. 58 and ca. 110 ka). The sedimentary characteristics of the individual units from both records share a general trend of a downcore transition from banded (at the top) to increasingly well-laminated sediments. It is important to note though that the distinctness of the preserved laminations in the Orakei record are superior to those of the Onepoto lake sediment record. Similarly, there is a gradual downcore increase in organic detritus and mass-wasting deposits observable in both sequences. Mass-wasting inducing events (e.g., storms and/or earthquakes) and a less fully developed stratification of the water column are at both sites towards the top of this group, indicated by transition from laminations to banding towards the top in Unit I(d) and Unit 9. For this group, Eg4 tephra currently provides the most reliable age marker.

For LG-5 (ca. 130–119 ka), time constraints for this phase are provided by a good agreement between the age model present in this study with the dated age of eruption that formed Orakei Basin (ca. 130 ka) and the basaltic "AVF aa" tephra recorded in the Orakei lake sediment sequence (ca. 119 ka). The transition from Unit I to Unit II (Onepoto) and from Unit 12 to Unit 13 (Orakei) is marked by a significant increase in coarse sand and gravel-rich layers with often angular-shaped grains (mass-wasting deposits) in both records. However, the Orakei lake sediment sequence depicts well-developed laminations at high frequency that have no corresponding equivalent in the Onepoto lake sequence. In the latter, laminations are rather poorly to, at best, moderately developed. This suggests better developed water column stratification at Orakei maar lake at this time. Both sites reflect reoccurring strong (coarse grained material) mass-wasting inducing events (e.g., storms and/or earthquakes). After Orakei maar's formative eruption, the initial shallow lake (massive sediments in Unit 14) transitioned into a deep lake basin with conditions favourable for lamination formation in the profundal zone (high-frequency laminations in Unit 13). Onepoto maar lake, on the other hand, depicts a fully developed lake system with at times not optimal bottom-water conditions that allowed for the development of laminations.

Generally, both lake sediment sequences recorded increased activity of tephra source volcanic centres with felsic magma composition (e.g., TVZ) over the last ca. 45 kyr whilst older lake sediments are largely devoid of rhyolitic tephra. For most of the later stages of infill of both lakes (<60 ka), the identified sedimentary features broadly reflect environmental settings. This is especially the case for LG-3 and most of LG-2. However, a diverging trend becomes increasingly apparent prior to the onset of estuarine deposition at ca. 9 ka (later stage of LG-2 and LG-1), displayed by a shallowing upwards trend recorded in the Orakei maar palaeolake. Onepoto maar, on the other hand, remains a deep lake basin until the breach of the crater rim and subsequent onset of estuarine sedimentation. Furthermore, in both maar lake sequences a general trend to increased presence of mass-movement deposits (sand to gravel) and organic fragments (e.g., wood) is recorded downcore, especially from the onset of LG-4 onwards (>60 ka) to LG-5. Overall, laminations (< millimetre scale) are more well developed and continuous in the Orakei lake sequence in contrast to the Onepoto lake sediment record (Figs. 3 and 8).

4.6 Preliminary reconstruction of Onepoto maar lake sediment sequence evolution

Formation of the crater (> 150–193 ka; AVF D) to AVF C (ca. 181 ka). This early phase of lake sedimentation can be allocated to MIS 6e based on the available age constraints. However, the disturbed condition of the sediments, likely caused when the drill core penetrated the comparably thick and dense basaltic lapilli of deposit AVF C, does not allow for reliable interpretation of environmental conditions.

AVF C (ca. 181 ka) to AVF B (ca. 146 ka). The ca. 35 kyr phase represented in this part of the record can be roughly correlated to MIS 6d, MIS 6c, and MIS 6b (Railsback et al., 2015) based on the given age constraints provided by the age–depth model presented in this study. Overall, the sediments of this section consist of light brown to dark brown silts and clays with mainly poorly to moderately developed laminations and occasional thicker (decimetre-scale) mass-wasting deposits. We calculate an averaged accumulation of ∼ 1.92 m clastic and tephra material in this ∼ 6.24 m part of the record. The transitions from one stage to the next are often marked by changes in colour and facies. While the ca. 1 m thick dark brown silts with moderately to well-developed laminations above AVF C align with MIS 6d, the following 2 m of sediments above can be correlated to MIS 6c. The preservation of laminated sediments during MIS 6d infer the presence of a stratified water column with bottom-water conditions or sediment anoxia that prevented sediment bioturbation. In contrast, the sediments of MIS 6d contain a thicker dark brown mass-wasting deposit and light brown silts with poor to moderately developed laminations. The latter depicts less favourable bottom-water conditions for the development of laminated sediments. MIS 6b is represented by ∼ 2 m of massive light brown clayey silts with vivianite flecks and dark brown silts with moderately developed laminations that suggest another phase of suboptimal bottom-water condition for lamination development.

AVF B (ca. 146 ka) to Eg4 (77.17 ka). Between the Eg4 (ca. 77 ka) and AVF B tephra (ca. 146 ka), a ca. 69 kyr duration of lacustrine sedimentation is generally marked by repeated influx of crater-wall-sourced sands and gravel as well as metre-

scale subaqueous debris flow deposits. Altogether, we document an averaged accumulation of ~ 4.94 m of clastic and tephra material for this ~ 7.56 m part of the record. Here changes in colour and facies or transitions from one lithological unit to the other do not always strictly trace shifts between marine isotope stages. This either implies local environmental drivers partially overriding broader climatic trends or that climatic changes occurring recorded elsewhere have not set in the same time in the area around at the study site. While the ~ 2 m of sediments following AVF B consists of mainly light brown clayey silts with gritty bands, a noticeable transition occurs at 26.46 m with the onset of ~ 0.75 m dark brown silts with well-developed laminations and comparably reduced influx of crater-rim-sourced material reflecting a brief phase of stable environmental conditions and bottom-water/sediment anoxia due to a stratified water column. From our age model, an estimated age of ca. 130 ka is inferred. The phase from the AVF B event to the deposition of the thick mass-wasting deposit can therefore be allocated to MIS 6a, placing it in the Penultimate Glacial Maximum (PGM). We interpret the cause of the subaqueous debris flow deposit to be possibly related to a significant seismic shock that was perhaps triggered by the formative eruption of Orakei Basin calculated to ca. 130 ka (Peti et al., 2021; see correlation Fig. 8). A slightly younger deposit of light brown clayey silts rich in abundant basaltic detritus (at 21–22 m; estimated age 126–127 ka) may be the product of an increased local volcanic activity such as the Orakei crater in a very early stage of its existence. Additionally, during this time (MIS 5e) the Onepoto maar ring is a substantial feature well protected from high MIS 5e sea levels by the tuff ring. A renewed shift in sediment colour and facies occurs at 19.36 m with the onset of dark brown ~ 1.6 m thick silts with well-developed laminations exhibiting a renewed phase of stable environmental conditions with a stratified water column and anoxic bottom waters or sediments. We can assign an estimated age range from 124–122 ka for this stage of Onepoto maar lake's evolution and correlate this phase with the onset of MIS 5d. Furthermore, the transition from lithostratigraphic Unit II to (Sub-)Unit I(f) at 15.8 m can be inferred to have occurred during MIS 5d at ca. 119 ka. The latter is supported by the existence of AVF aa (age in the Orakei maar lake record (Fig. 8)). Moreover, the current age constraints suggest the transition from MIS 5d to 5c to be recorded at 12.6 m as well as the transition from MIS 5c to 5b at 11.46 m, which coincides with the transition from Sub-Unit I(f) to Sub-Unit I(e). Additionally, the MIS 5b to MIS 5a boundary can be placed at the contact of Sub-Unit I(e) to Sub-Unit I(d) at 8.65 m. Unlike Orakei Basin where the individual substages of MIS 5 thus far could not be reliably detected by the recently executed study for this site (Peti, 2020), the >130 ka part of the Onepoto lake sediment record seems to reflect changes in lithological composition in response to broader climatic shifts. Yet, a further strengthening of the age model will be required for a robust interpretation.

Eg4 tephra to M/F (ca. 77–9 ka; upper ~ 7.56 m of the record). The lithostratigraphic sub-units I(a) to I(d) span the phase after the deposition of the Eg4 tephra until the transition to estuarine conditions. Overall, an average thickness of ~ 0.87 m of clastic material and tephra was deposited in the basin during this phase (Fig. 3) and may infer relatively stable environmental conditions with few sediment influx events. For this late phase of the Onepoto development, robust age constraints are provided by rhyolitic tephra ages and radiocarbon ages (Fig. 7). Well-laminated sediments are mainly found in Sub-Unit I(c), which we can correlate with MIS 3a. The available age constraints demonstrate that the largest part of this unit relates to the phase prior to the Last Glacial Maximum (LGM). However, the presence of Okaia tephra ca. 28.62 ka cal BP also highlights that the uppermost section could contain signals that support the eLGM (extended LGM; Newnham et al., 2007) of New Zealand (Rother et al., 2014). Further, Sub-Unit I(a) that follows above can be assigned to the late MIS 2 to MIS 1 transition. The preservation of these laminations indicates renewed phases of water column stratification with bottom-water/sediment anoxia preventing sediment bioturbation. Sub-Unit I(b) can therefore confidently be correlated to the LGM. A detailed description and interpretations on the regional environmental evolution recorded in the ca. 30–9 ka section of the lake sediment sequence are outlined in Augustinus et al. (2011, 2012) based on the analysis of pollen and diatom assemblages as well as geochemical proxies.

5 Possible project outcomes

A multi-method, high-resolution chronology (centennial to decadal timescale) is currently being established for the Onepoto palaeolake sediment sequence. This process uses radiocarbon dating, and U/Th dating on a large (4×1 cm) vivianite nodule (sub-unit I(f), ca. 13.35 m below M/F transition), relative palaeo-intensity variation of the Earth's magnetic field for targeted areas of the sediment record and magnetic-field-strength-controlled influx of meteoric ^{10}Be cosmogenic radionuclides into the basin. This approach mirrors aspects of the approach used for the Orakei palaeolake age model development (Peti et al., 2020) and will assist with development of robust high-resolution correlations between the lengths of the two sequences in common. The approach of combined palaeo-intensity variation and meteoric ^{10}Be has also been recently applied to the Lake Selina (Tasmania, Australia) sediment sequence and aided the chronology development (Lisé-Pronovost et al., 2021), which supports our expectations of this technique. Alongside this work, a comparison and correlation of the Orakei basin record and its recently established robust age model (Peti et al., 2020) with the newly established maar lake record presented here shows the potential of transferring key aspects of the Orakei age model to the Onepoto lake sediment sequence age model.

We expect the available multi-element µ-XRF core scanning time series to be crucial in linking the two records more robustly together. Furthermore, we are combining these µ-XRF downcore variability trends with measurements of loss-on-ignition, carbon and nitrogen content, and carbon isotopes to start the process of reconstructing climatically forced environmental change from northern New Zealand over much of the last two glacial cycles (ca. 200 ka). Representative thin-sections are also being examined from parts of the record with well-developed laminations (< millimetre scale) for micro-facies analysis to detect abrupt climate shifts and short- to long-term changes in seasonality. Extending pollen and diatom analyses prior to MIS 3 (Augustinus et al., 2011, 2012) will also provide important palaeoecological information necessary for development of detailed insights into drivers of changes in Onepoto palaeolimnology as well as catchment palaeoecology and associated palaeoclimate.

Multi-proxy analysis of the Onepoto maar lake sediments is expected to produce the following insights:

1. Further development of improved constraints for the frequency and magnitude of regional basaltic volcanic activity within the Auckland Volcanic Field by delivering better age estimates, especially prior to the deposition of the known-age Rotoehu tephra by combining the recently refined ages presented in Peti et al. (2021) with new results produced from the new Onepoto record.

2. A refined tephrochronology for Onepoto from all volcanic sources will also allow for an improved volcanic hazard assessment for Auckland City. As well as AVF basaltic volcanism, ash falls from distal sources (mostly andesitic but also rhyolitic) are a frequently reoccurring volcanic hazard for the Auckland region.

3. The dating of tephra age markers older than 50 ka using meteoric cosmogenic nuclide ([10]Be) variability in the Onepoto sediments driven by well-known changes in Earth's magnetic field intensity (see references in Peti et al., 2020) will enable more accurate and precise dating of the sequence. Our study aims to achieve an overlap with the Orakei maar record below the Rotoehu tephra (45 ka and the Laschamp excursion (ca. 41 ka, Nilsson et al., 2011) to complement the Orakei age model. This approach will likely establish trends of meteoric cosmogenic nuclide ([10]Be) variability spanning nearly two full glacial cycles. We expect that the Onepoto age model will be robust enough to be able to observe environmental oscillations and events identified in the sequence to regional and possibly intra- and inter-hemispheric climatic events.

4. Principal component analysis (PCA) of the µ-XRF core scanning time series will provide additionally aid for our palaeoenvironmental interpretation. Application of this approach to high-resolution XRF data identifies the

processes and features that drive the observed variability.

6 Conclusions

The ongoing study of the lake sediment sequence contained in Onepoto maar outlined here has produced a composite facies log derived from overlapping core sections guided by prominent tephra layers and sedimentary features such as mass movement deposits, distinct well-laminated segments and features representative of distinctive facies types. More challenging core section alignments were achieved using high-resolution radiographic images, tephrochronology, µ-XRF and magnetic susceptibility time series data.

The preliminary Onepoto age model presented here reflects the issue of poor age control for large sections of the pre-50 ka sequence. Nevertheless, promising improvements have been made by correlating the Onepoto sequence to that of Orakei Basin, thereby extending age control to the base of that sequence using a range of known-age tie points. Age markers for the early stage of the lake and its eruptive formation are provided through AVF-sourced basaltic ejecta (AVF B/ AVF C) and the lava at the base (AVF D). Significant age uncertainties, especially for AVF D, or independently supported ages as in the case of AVF C and the lack of further reliable marker layers (e.g., AVF A) between Eg4 to AVF B (spanning ca. 69 ka) as well as AVF B to AVF C (spanning ca. 34 ka) require more robust age constraints. This is currently underway using [10]Be cosmogenic nuclide flux supported by measurement of relative magnetic palaeo-intensity variation in sections of the core (e.g., Laschamp Event) using an approach analogous to that used for the Orakei maar lake chronology development.

The pre-77 ka phase of lake sediment deposition at Onepoto is marked by a dominance of debris flows and deposition of many thin andesitic tephra (mainly sub-millimetre-scale thickness) originating from distal volcanic centres (e.g., Egmont/Taranaki and Tongariro VCs). However, discontinuous sections of well-developed laminations (< millimetre scale) are also present. These findings are indicative of phases of varying clastic input/chemical conditions driven by climatic signals while the preservation was affected by bottom-water/sediment anoxia driven by water column stratification preventing sediment bioturbation.

AVF maar lake sediments exhibit enormous potential for the identification and interpretation of short-duration climate events and long-term climate trends as well as intra- and inter-hemispheric climate. In tandem with ongoing work on Orakei maar, the study of Onepoto maar lake sediments will extend this record by providing high-resolution palaeoclimate and palaeoenvironmental reconstructions spanning the last two glacial cycles.

Author contributions. PCA leads the AVF maar project, secured funding, and is involved in all aspects of the work. BL conducted the core descriptions, Itrax µ-XRF core scans, and development of the composite stratigraphy. EMPA measurements of tephra samples were conducted by JLH at Victoria University of Wellington. BL wrote the original version of this report with refinements from PCA with suggestions provided by LP and JLH. The drilling investigation team included PCA, BL, and LP.

References

Alloway, B. V., Lowe, D. J., Barrell, D. J. A., Newnham, R. M., Almond, P. C., Augustinus, P. C., Bertler, N. A. N., Carter, L., Litchfield, N. J., McGlone, M. S., Shulmeister, J., Vandergoes, M. J., and Williams, P. W.: Towards a climate event stratigraphy for New Zealand over the past 30 000 years (NZ-INTIMATE project), J. Quaternary Sci., 22, 9–35, https://doi.org/10.1002/Jqs.1079, 2007.

Augustinus, P. C., D'Costa, D., Deng, Y., Hagg, J., and Shane, P.: A multi-proxy record of changing environments from ca. 30000 to 9000 cal. a BP: Onepoto maar paleolake, Auckland, New Zealand, J. Quaternary Sci., 26, 389–401, https://doi.org/10.1002/jqs.1463, 2011.

Augustinus, P. C., Cochran, U., Kattel, G., D'Costa, D., and Shane, P.: Late Quaternary paleolimnology of Onepoto maar, Auckland, New Zealand: Implications for the drivers of regional paleoclimate, Quaternary. Int., 253, 18–31, https://doi.org/10.1016/j.quaint.2011.02.028, 2012.

Blaauw, M. and Christen, J. A.: Flexible paleoclimate age-depth models using an autoregressive gamma process, Bayesian Anal., 6, 457–474, https://doi.org/10.1214/11-BA618, 2011.

Brauer, A., Endres, C., and Negendank, J. F.: Lateglacial calendar year chronology based on annually laminated sediments from Lake Meerfelder Maar, Germany, Quaternary Int., 61, 17–25, https://doi.org/10.1016/S1040-6182(99)00014-2, 1999.

Bronk Ramsey, C.: Bayesian analysis of radiocarbon dates, Radiocarbon, 511, 337–360, https://doi.org/10.1017/S0033822200033865, 2009.

Croudace, I. W. and Rothwell, R. G.: Micro-XRF sediment core scanners: important new tools for the environmental and earth sciences, Spectroscopy Europe, 22, 6–13, https://doi.org/10.1007/978-94-017-9849-5, 2015.

Croudace, I. W., Rindby, A., and Rothwell, R.: ITRAX: description and evaluation of a new multi-function X-ray core scanner, Geol. SOC. Spec. Publ., London, 267, 51 LP-63, https://doi.org/10.1144/GSL.SP.2006.267.01.04, 2006.

Danišík, M., Shane, P., Schmitt, A. K., Hogg, A., Santos, G. M., Storm, S., Evans, N. J., Fifield, L. K., and Lindsay, J. M.: Re-anchoring the late Pleistocene tephrochronology of New Zealand based on concordant radiocarbon ages and combined 238U/230[Th] disequilibrium and (U–Th)/He zircon ages, Earth. Planet. Sci. Lett., 349, 240–250, https://doi.org/10.1016/j.epsl.2012.06.041, 2012.

Danišík, M., Lowe, D. J., Schmitt, A. K., Friedrichs, B., Hogg, A. G., and Evans, N. J.: Sub-millennial eruptive recurrence in the silicic Mangaone Subgroup tephra sequence, New Zealand, from Bayesian modelling of zircon double-dating and radiocarbon ages, Quat. Sci. Rev., 246, 106517, https://doi.org/10.1016/j.quascirev.2020.106517, 2020.

Fink, D., Hotchkis, M., Hua, Q., Jacobsen, G., Smith, A. M., Zoppi, U., Child, D., Mifsud, C., van der Gaast, H., Williams, A., and Williams, M.: The ANTARES AMS facility at ANSTO, NIM B, 223–224, 109–115, 2004.

Francus, P., Lamb, H., Nakagawa, T., Marshall, M., and Brown, E.: The potential of high-resolution X-ray fluorescence core scanning: applications in paleolimnology, PAGES (Past Global Changes) News, 17, 93–95, 2009.

Hägg, J. and Augustinus, P. C.: Scientific data report from the Onepoto Crater drilling (NZ-Maar) project: December 2000/July 2001, pp. 7–15, 2003.

Hayward, B. W., Morley, M. S., Sabaa, A. T., Grenfell, H. R., Molloy, C., Shane, P. A., and Augustinus, P. A.: Fossil record of the Post-glacial marine breaching of Auckland's volcanic maar craters, Records of the Auckland Museum, 45, 73–99, 2008.

Hogg, A. G., Heaton, T. J., Hua, Q., Palmer, J. G., Turney, C. S., Southon, J., Bayliss, A., Blackwell, P. G., Boswijk, G., Ramsey, C. B., and Pearson, C.: SHCal20 Southern Hemisphere Calibration, 0–55,000 Years cal BP, Radiocarbon, 62, 759–778, https://doi.org/10.1017/RDC.2020.59, 2020.

Hopkins, J. L., Millet, M. A., Timm, C., Wilson, C. J. N., Leonard, G. S., Palin, J. M., and Neil, H.: Tools and techniques for developing tephra stratigraphies in lake cores: A case study from the basaltic Auckland Volcanic Field, New Zealand, Quaternary Sci. Rev., 123, 58–75, https://doi.org/10.1016/j.quascirev.2015.06.014, 2015.

Hopkins, J. L., Wilson, C. J. N., Millet, M. A., Leonard, G. S., Timm, C., McGee, L. E., Smith, I. E. M., and Smith, E. G. C.: Multi-criteria correlation of tephra deposits to source centres applied in the Auckland Volcanic Field, New Zealand, B. Volcanol., 79, 55, https://doi.org/10.1007/s00445-017-1131-y, 2017.

Hopkins, J. L., Smid, E. R., Eccles, J. D., Hayes, J. L., Hayward, B. W., McGee, L. E., van Wijk, K., Wilson, T. M., Cronin, S. J., Leonard, G. S., and Lindsay, J. M.: Auckland Volcanic Field magmatism, volcanism, and hazard: a review, New Zeal. J. Geol. Geop., 1–22, https://doi.org/10.1080/00288306.2020.1736102, 2020.

Jarvis, S., Croudace, I. W., and Rothwell, R. G.: Parameter optimisation for the ITRAX core scanner, in: Micro-XRF Studies of Sediment Cores, Springer, Dordrecht, pp. 535–562, https://doi.org/10.1007/978-94-017-9849-5_22, 2015.

Kylander, M. E., Lind, E. M., Wastegard, S., and Lowemark, L.: Recommendations for using XRF core scanning as a tool in tephrochronology, Holocene, 22, 371–375, https://doi.org/10.1177/0959683611423688, 2012.

Läuchli, B. and Augustinus, P. C.: AMS radiocarbon ages from the Onepoto maar lake sediment record, figshare, https://doi.org/10.6084/m9.figshare.13683874, 2021.

Läuchli, B., Augustinus, P. C., and Hopkins, J. L.: Onepoto2018_Tephra_Rotoma-Eg4, figshare, https://doi.org/10.6084/m9.figshare.13683658, 2021.

Leonard, G. S., Calvert, A. T., Hopkins, J. L., Wilson, C. J. N., Smid, E. R., Lindsay, J. M., and Champion, D. E.: High-precision 40Ar/39Ar dating of Quaternary basalts from Auckland Volcanic Field, New Zealand, with implications for eruption rates and paleomagnetic correlations, J. Volcanol. Geoth. Res., 343, 60–74, https://doi.org/10.1016/j.jvolgeores.2017.05.033, 2017.

Lindsay, J. M., Leonard, G. S., Smid, E. R., and Hayward, B. W.: Age of the Auckland Volcanic Field: a review of existing data, New Zeal. J. Geol. Geop., 54, 379–401, https://doi.org/10.1080/00288306.2011.595805, 2011.

Lisé-Pronovost, A., Fletcher, M. S., Simon, Q., Jacobs, Z., Gadd, P. S., Heslop, D., Herries A. I. R., and Yokoyama, Y.: Chronostratigraphy of a 270-ka sediment record from Lake Selina, Tasmania: Combining radiometric, geomagnetic and climatic dating, Quat. Geochronol., 62, 101152, https://doi.org/10.1016/j.quageo.2021.101152, 2021.

Lowe, D. J., Blaauw, M., Hogg, A. G., and Newnham, R. M.: Ages of 24 widespread tephras erupted since 30,000 years ago in New Zealand, with re-evaluation of the timing and paleoclimatic implications of the Lateglacial cool episode recorded at Kaipo bog, Quaternary Sci. Rev., 74, 170–194, https://doi.org/10.1016/j.quascirev.2012.11.022, 2013.

Löwemark, L., Chen, H. F., Yang, T. N., Kylander, M., Yu, E. F., Hsu, Y. W., Lee, T. Q., Song, S. R., and Jarvis, S.: Normalizing XRF-scanner data: a cautionary note on the interpretation of high-resolution records from organic-rich lakes, J. Asian Earth Sci., 40, 1250–1256, https://doi.org/10.1016/j.jseaes.2010.06.002, 2011.

Marchetto, A., Ariztegui, D., Brauer, A., Lami, A., Mercuri, A. M., Sadori, L., Vigliotti, L., Wulf, S., and Guilizzoni, P.: Volcanic Lake Sediments as Sensitive Archives of Climate and Environmental Change, in: Volcanic Lakes, edited by: Rouwet, D., Christenson, B., Tassi, F., and Vandemeulebrouck, J., Berlin, Heidelberg: Springer Berlin Heidelberg, pp. 379–399, https://doi.org/10.1007/978-3-642-36833-2_17, 2015.

Molloy, C.: Tephrostratigraphy of the Auckland Maar Craters (unpublished master's thesis), University of Auckland, New Zealand, 2008.

Molloy, C., Shane, P., and Augustinus, P. C.: Eruption recurrence rates in a basaltic volcanic field based on tephra layers in maar sediments: Implications for hazards in the Auckland volcanic field, Bull. Geol. Soc. Am., 121, 1666–1677, https://doi.org/10.1130/B26447.1, 2009.

Newnham, R. M., Lowe, D. J., Giles, T., and Alloway, B. V.: Vegetation and climate of Auckland, New Zealand, since ca. 32 000 cal. yr ago: support for an extended LGM, J. Quat. Sci., 22, 517–534, 2007.

Nilsson, A., Muscheler, R., Snowball, I., Aldahan, A., Possnert, G., Augustinus, P. C., Atkin, D., and Stephens, T.: Multi-proxy identification of the Laschamp geomagnetic field excursion in Lake Pupuke, New Zealand, Earth Planet. Sci. Lett., 311, 155–164, https://doi.org/10.1016/j.epsl.2011.08.050, 2011.

Nunns, A. G. and Hochstein, M. P.: Geophysical constraints on the structure and formation of Onepoto, Orakei, Pupuke and Tank Farm maar volcanoes, Auckland Volcanic Field, New Zeal. J. Geol. Geop., 62, 341–356, https://doi.org/10.1080/00288306.2019.1581239, 2019.

Peti, L.: High-resolution composite stratigraphy and multi-method dating of Auckland maar sediment records spanning the Last Glacial Interval (unpublished doctoral thesis), University of Auckland, New Zealand, 2020.

Peti, L. and Augustinus, P. C.: Stratigraphy and sedimentology of the Orakei maar lake sediment sequence (Auckland Volcanic Field, New Zealand), Sci. Dril., 25, 47–56, https://doi.org/10.5194/sd-25-47-2019, 2019.

Peti, L., Fitzsimmons, K. E., Hopkins, J. L., Nilsson, A., Fujioka, T., Fink, D., Mifsud, C., Christl, M., Muscheler, R., and Augustinus, P. C.: Development of a multi-method chronology spanning the Last Glacial Interval from Orakei maar lake, Auckland, New Zealand, Geochronology, 2, 367–410, https://doi.org/10.5194/gchron-2-367-2020, 2020.

Peti, L., Hopkins, J. L., and Augustinus, P. C.: Revised tephrochronology for key tephras in the 130-ka Ōrākei Basin maar core, Auckland Volcanic Field, New Zealand: implications

for the timing of climatic changes, New Zeal. J. Geol. Geophy., 1–15, https://doi.org/10.1080/00288306.2020.1867200, 2021.

Poth, D. and Negendank, J. F.: Paleoclimate reconstruction at the Pleistocene/Holocene transition – A varve dated microstratigraphic record from Lake Meerfelder Maar (Westeifel, Germany), in: Paleolimnology of European maar lakes, Springer, Berlin, Heidelberg, pp. 209–222, https://doi.org/10.1007/BFb0117598, 1993.

Railsback, L. B., Gibbard, P. L., Head, M. J., Voarintsoa, N. R. G., and Toucanne, S.: An optimized scheme of lettered marine isotope substages for the last 1.0 million years, and the climatostratigraphic nature of isotope stages and substages, Quaternary Sci. Rev., 111, 94–106, https://doi.org/10.1016/j.quascirev.2015.01.012, 2015.

R Core Team: A language and environment for statistical computing, R Foundation for Statistical Computing, Vienna, Austria, available at: https://www.R-project.org/ (last access: 1 February 2021), 2020.

Rother, H., Fink, D., Shulmeister, J., Mifsud, C., Evans, M., and Pugh, J.: The early rise and late demise of New Zealand's last glacial maximum, P. Natl. Acad. Sci. USA, 11, 11630–11635, https://doi.org/10.1073/pnas.1401547111, 2014.

Sandiford, A., Newnham, R., Alloway, B., and Ogden, J.: A 28 000–7600 cal yr BP pollen record of vegetation and climate change from Pukaki Crater, northern New Zealand, Paleogeogr. Paleoclimatol. Paleoecol., 201, 235–247, https://doi.org/10.1016/S0031-0182(03)00611-4, 2003.

Shane, P. and Hoverd, J.: Distal record of multi-sourced tephra in Onepoto Basin, Auckland, New Zealand: implications for volcanic chronology, frequency and hazards, B. Volcanol., 64, 441–454, https://doi.org/10.1007/s00445-002-0217-2, 2002.

Shane, P. and Sandiford, A.: Paleovegetation of marine isotope stages 4 and 3 in Northern New Zealand and the age of the widespread Rotoehu tephra, Quaternary Res., 59, 420–429, https://doi.org/10.1016/S0033-5894(03)00044-9, 2003.

Sirocko, F., Knapp, H., Dreher, F., Förster, M. W., Albert, J., Brunck, H., Veres, D., Dietrich, S., Zech, M., Hambach, U., Röhner, M., Rudert, S., Schwibus, K., Adams, C., and Sigl, P.: The ELSA-Vegetation-Stack: Reconstruction of Landscape Evolution Zones (LEZ) from laminated Eifel maar sediments of the last 60 000 years, Glob. Planet. Change, 142, 108–135, 2016.

Stephens, T., Atkin, D., Augustinus, P. C., Shane, P., Lorrey, A., Street-Perrott, A., Nilsson, A., and Snowball, I.: A late glacial Antarctic climate teleconnection and variable Holocene seasonality at Lake Pupuke, Auckland, New Zealand, J. Paleolimnol., 48, 785–800, 2012a.

Stephens, T., Atkin, D., Cochran, U., Augustinus, P. C., Reid, M., Lorrey, A., Shane, P., and Street-Perrott, A.: A diatom-inferred record of reduced effective precipitation during the Last Glacial Coldest Phase (28.8–18.0 cal kyr BP) and increasing Holocene seasonality at Lake Pupuke, Auckland, New Zealand, J. Paleolimnol., 48, 801–817, https://doi.org/10.1007/s10933-012-9645-y, 2012b.

St.-Onge, G., Mulder, T., Francus, P., and Long, B.: Chapter Two Continuous Physical Properties of Cored Marine Sediments, in: Proxies in Late Cenozoic Paleoceanography, edited by: Hillaire-Marcel, C., and De Vernal, A. B. T., Elsevier, 1, 63–98, https://doi.org/10.1016/S1572-5480(07)01007-X, 2007.

Vandergoes, M. J., Hogg, A. G., Lowe, D. J., Newnham, R. M., Denton, G. H., Southon, J. B., David, J. A., Wilson, C. J. N., McGlone, M. S., Allan, A. S. R., Almond, P. C., Petchey, F., Dabell, K., Dieffenbacher-Krall, A. C., and Blaauw, M.: A revised age for the Kawakawa/Oruanui tephra, a key marker for the Last Glacial Maximum in New Zealand, Quat. Sci. Rev., 74, 195–201, https://doi.org/10.1016/j.quascirev.2012.11.006, 2013.

Williams, T., Creer, K. M., and Thouveny, N.: Preliminary 50m paleomagnetic records from Lac Du Bouchet, Haute Loire, France", in: Paleolimnology of European Maar Lakes, edited by: Negendank, J. F. W. and Zolitschka, B., Lecture Notes in Earth Sciences, Springer, Berlin, Heidelberg, 49, 367–376, https://doi.org/10.1007/BFb0117607, 1993.

Zolitschka, B. and Enters, D.: Lacustrine sediments,, in: Encyclopedia of Paleoclimatology and Ancient Environments, edited by: Gornitz, V., Encyclopedia of Earth Sciences Series, Springer, Dordrecht, the Netherlands, 486–488, https://doi.org/10.1007/978-1-4020-4411-3_120 2009.

Zolitschka, B., Anselmetti, F., Ariztegui, D., Corbella, H., Francus, P., Lücke, A., Maidana, N. I., Ohlendorf, C., Schäbitz, F., and Wastegård, S.: Environment and climate of the last 51,000 years–new insights from the Potrok Aike maar lake Sediment Archive Drilling project (PASADO), Quaternary Sci. Rev., 71, 1–12, https://doi.org/10.1016/j.quascirev.2012.11.024, 2013.

Scientific Drilling

Open Access

New geophysical memory-logging system for highly unstable and inclined scientific exploration drilling

Jochem Kück, Marco Groh, Martin Töpfer, Andreas Jurczyk, and Ulrich Harms

GFZ German Research Centre for Geosciences, Telegrafenberg, 14473 Potsdam, Germany

Correspondence: Jochem Kück (jkueck@gfz-potsdam.de)

Abstract. We established a cable-free memory-logging system for drill-string-deployed geophysical borehole measurements. For more than 20 years, various so-called "logging while tripping" (LWT) techniques have been available in the logging service industry. However, this method has rarely been used in scientific drilling, although it enables logging in deviated and unstable boreholes, such as in lacustrine sediment drilling projects. LWT operations have a far lower risk of damage or loss of downhole logging equipment compared with the common wireline logging. For this purpose, we developed, tested, and commissioned a modular memory-logging system that does not require drill string modifications, such as special collars, and can be deployed in standard wireline core drilling diameters (HQ, bit size of 96 mm, and PQ, bit size of 123 mm). The battery-powered, autonomous sondes register the profiles of the natural GR (gamma radiation) spectrum, sonic velocity, magnetic susceptibility, electric resistivity, temperature, and borehole inclination in high quality while they are pulled out along with the drill string. As a precise depth measurement carried out in the drill rig is just as important as the actual petrophysical downhole measurements, we developed depth-measuring devices providing a high accuracy of less than 0.1 m deviation from the wireline-determined depth. Moreover, the modular structure of the system facilitates sonde deployment in online mode for wireline measurements.

1 Introduction

Borehole measurements are an indispensable part of scientific drilling projects to gain physical and chemical parameters continuously and in situ (Goldberg, 1997). They are usually carried out using the well-established wireline logging method, in which the measuring sondes are moved on a logging cable in the borehole. This method has the advantages of power supply to the sondes, online data transfer to the recording unit at surface, and very precise and reliable depth measurements. Furthermore, it is easy and flexible to use, comprises the largest range of sonde types, and is readily available through a large number of academic and commercial providers. In the framework of the International Continental Scientific Drilling Program (ICDP), we have conducted more than 37 wireline logging campaigns (Hodell et al., 2006; Koeberl et al., 2007; Gebhardt et al., 2013; Jackson et al., 2019; Jerram et al., 2019; Abbott and Rodbell, 2020) using slimhole tools. For the majority of these missions, most demands could be covered. However, there is also a significant

proportion of projects in which unintentional or technically necessary downhole conditions adverse to wireline logging occur, making the use of logging sondes on a cable risky, extremely difficult, and, therefore, very time-consuming or even impossible. The most common adversities are partially blocked boreholes (e.g., large-scale wall collapse or local bridging) and borehole paths that deviate strongly from vertical.

In lacustrine sediment coring projects, operations are performed without casing; thus, unconsolidated sediments occurring over long sections often rapidly narrow boreholes and make them impassable for lightweight logging sondes. Mostly, however, a machine-powered drill string can pass through without problems or is used to redrill the well quickly. In such cases, the usual wireline logging procedure is to position the drill string at a depth with the drill bit below the suspected unstable section and to run the wireline sondes through the string into the open hole section below the bit. After measuring this section with all desired sondes,

the drill string is pulled higher, leaving the unstable section uncased. These steps are repeated as often as the formation instabilities require (Baumgarten and Wonik, 2015). Overall, this is a very time-consuming procedure and can take up to 10 times longer than normal, unimpeded wireline logging in a several-hundred-meter-deep hole. Another obstacle is that wireline sondes are always run through the drill bit into the open hole. This causes a high risk of getting stuck at the drill bit when reentering.

These limitations of wireline logging are currently hampering scientific and commercial operations; hence, there is a need for the invention of novel methods to perform downhole logging, especially under adverse conditions. The most prominent technique is the integration of logging sensors into the drill string (logging while drilling, LWD), which is widely used in complex hydrocarbon exploration (Hansen and White, 1991) and in scientific ocean drilling (e.g., Moore, 2000). Other deployment options include pipe-conveyed logging or stiff wireline logging, but these techniques are mostly associated with significantly higher costs compared with wireline logging. Another method has also frequently been used in scientific drilling involving robust wireless memory sondes that are mounted atop the inner core barrel, typically delivering parameters such as temperature, pressure, and acceleration, among others, which can be measured from inside a drill pipe (Guerin and Goldberg, 2002).

2   The logging while tripping method

For the logging of geophysical parameters, one cost-effective and minimum-risk method for drilling projects is the application of so-called memory-logging sondes (Singh et al., 2018). These sondes are not run on a logging cable, but measure autonomously at the end of the drill string after they have been dropped into the drill string (very much like an inner core barrel), and land on the landing shoulder in the outer core barrel at the drill bit. When the drill string is pulled out of the borehole (trip-out), the sondes are pulled along with it and the data are stored in the sonde, which is why this method is commonly referred to as "logging while tripping" (LWT; Figs. 1, 2; (Matheson and West, 2000).

The depth of each measuring point is determined at the surface as in wireline logging, but the assignment of the depth value to the measured value does not simultaneously take place during the measuring process; rather, the depth value is assigned to the measured value after the sonde data have been read out back on the surface. The combination of each individual downhole measured value with the associated surface depth value takes place by means of the measurement time (time stamp) registered in parallel at surface and down the hole. In other words, a downhole value with the same time as a depth value is assigned to this depth value. The depth and the downhole values are both deleted for times when the drill string is not moved upward, resulting a contin-
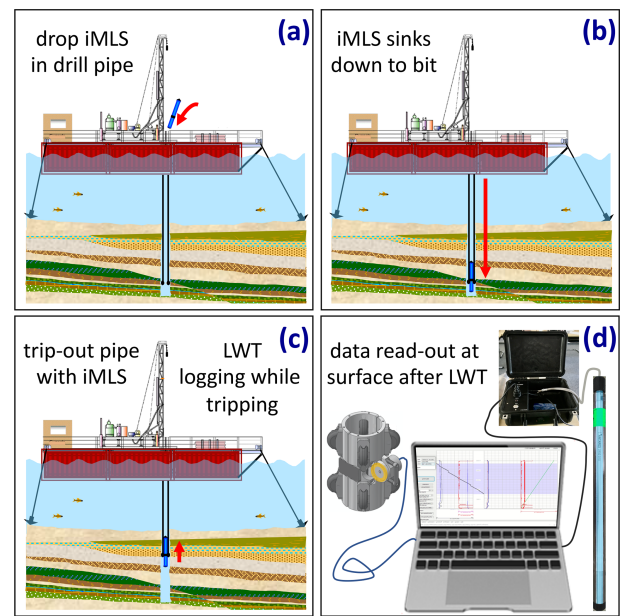

Figure 1. Representation of the logging while tripping (LWT) method in a lake coring setup: **(a)** dropping the ICDP memory-logging system (iMLS) in the drill string, **(b)** landing the iMLS in the outer core barrel at the drill bit, **(c)** trip-out of the drill string and alongside logging with the iMLS, and **(d)** reading out the data from the iMLS sonde memory and the iMLS depth-measuring device (iDMD).

uous, evenly decreasing depth profile of the downhole parameter. The LWT depth measurement in the drill rig is similar to the LWD depth determination; however, in the latter, the entire running-in of the drill string is measured from its very beginning at the derrick floor. LWT depth measurements can only begin when the last core has been drilled and brought to surface, i.e., the drill string has already been in the borehole for many core runs.

For LWT systems, the risks described above for wireline sondes are virtually negligible when running through unstable zones, because the tools only partially stick out of the core bit into the open hole. Moreover, the upper part of the tools always remains secure inside the drill string, which, on the one hand, completely eliminates the reentry risk and, on the other hand, minimizes exposure to the unstable hole. Should the LWT nevertheless get stuck, drillers can circulate drill mud through the drill bit in order to remove the blockage, and the tools in the drill string can easily be pulled with the high force of the drill rig. Under regular working conditions, the tool string can be retrieved at any time using the core retrieval device (coring wire line and overshot) – for example, if only a partial section of the borehole is to be logged or if technical drilling problems should arise.

Different variants of the logging while tripping method are used commercially worldwide (e.g., Aivalis et al., 2012; Beal, 2019). In the most widespread method, a special mod-
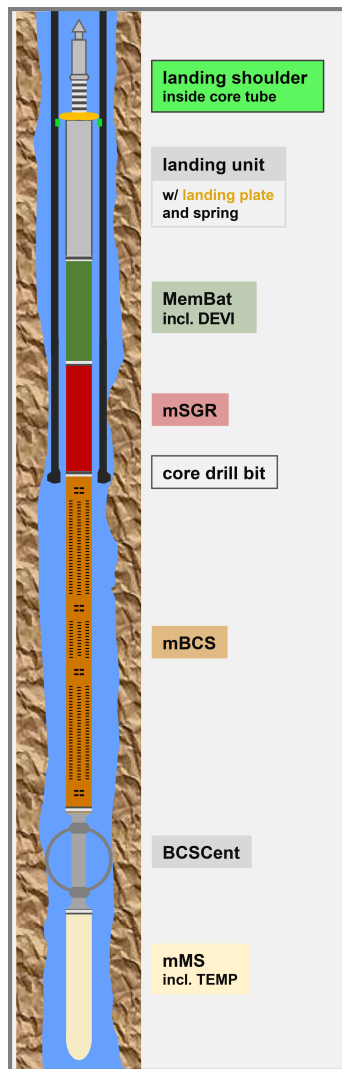
Figure 2. Sketch of a standard ICDP memory-logging system (iMLS) tool combination landed at the bottom of the drill string, partially sticking out into the open hole in a ready-to-log position (not to scale).

ified drill collar above the drill bit allows for the logging of some parameters from entirely within the pipe so that the logging tools never run into the open hole. Since 2012, a set of specially designed memory sondes have been deployed with the MeBo ocean floor drilling robot (Freudenthal et al., 2020), with most of the logging tools actually protruding out of the drill bit into the open hole. Having been involved in the very early development of the MeBo memory sondes, we used this successful example to develop, in cooperation with the same sonde manufacturer (ANTARES GmbH, Germany), a new and improved memory-logging sonde system motivated by a high demand for LWT capabilities in scientific drilling and a lack of affordable commercial LWT services.

3   The ICDP memory-logging system (iMLS)

The LWT system that we designed consists (from top to bottom) of a landing unit which can be adapted to different drill string dimensions, five combinable single memory sondes, and a precise, robust, and field-application-friendly depth-measuring device at the surface (Figs. 2, 3, 4).

3.1   The landing unit

This uppermost component of the iMLS tool string is mounted directly on the logging sondes. The purely mechanical landing unit is required to correctly position the actual measuring sondes inside and below the drill pipe. The unit consists of a fishing neck like that of an inner core barrel (Boart Longyear type), fitting pieces of different lengths, and a spring-loaded landing plate (Fig. 3). The modularity of the landing unit enables the use of the iMLS in various core drill strings with different bottom hole assembly geometry (outer core barrel and drill bit). Here, the length of the landing unit, the diameter of the landing plate, the hole size in the plate, and the stiffness of the impact suspension (spiral spring) are modified according to the length and the inner diameter of the outer core barrel. These exchanges can easily be done at the drill site, i.e., a change from PQ (bit size of 123 mm) to HQ (bit size of 96 mm) takes no more than 15 min. However, fitting rods for specific core barrel lengths have to be manufactured in advance. The iMLS is optimized for use in a wireline coring string with classic HQ dimensions (bit size of 96 mm), which is typical in ICDP drilling projects. With small adjustments, it can also be used in a larger PQ drill string (123 mm) and, with restrictions, in a smaller NQ string (76 mm). The suspension spring reduces the impact shock when the iMLS lands on the landing shoulder of the outer core barrel. Unlike an inner core barrel, which is anchored both downwards and upwards inside the outer core barrel, the landing plate does not latch; thus, the iMLS remains free upwards. This allows the sonde to give way upwards into the string should it accidentally be lowered and touch the well bottom or an obstruction. The descent rate of the sonde string inside the drill string is reduced by using an adapted landing plate design to change the flow resistance for a gentle and safe landing. The situation is different in strongly inclined bores with a deviation from vertical of $> 50°$ where the weight of the sondes is usually no longer sufficient to overcome friction and to cause the sondes to stop sliding down the drill string. In such cases, the iMLS can be actively pumped down the pipe with the drill mud circulation until it lands on the drill bit.

3.2   The sondes

Based on proven wireline slimhole sondes, the iMLS sondes were further developed for autonomous memory measurements. These are so-called slimhole tools with a maximum outer diameter of 52 mm. All of the sondes can register at
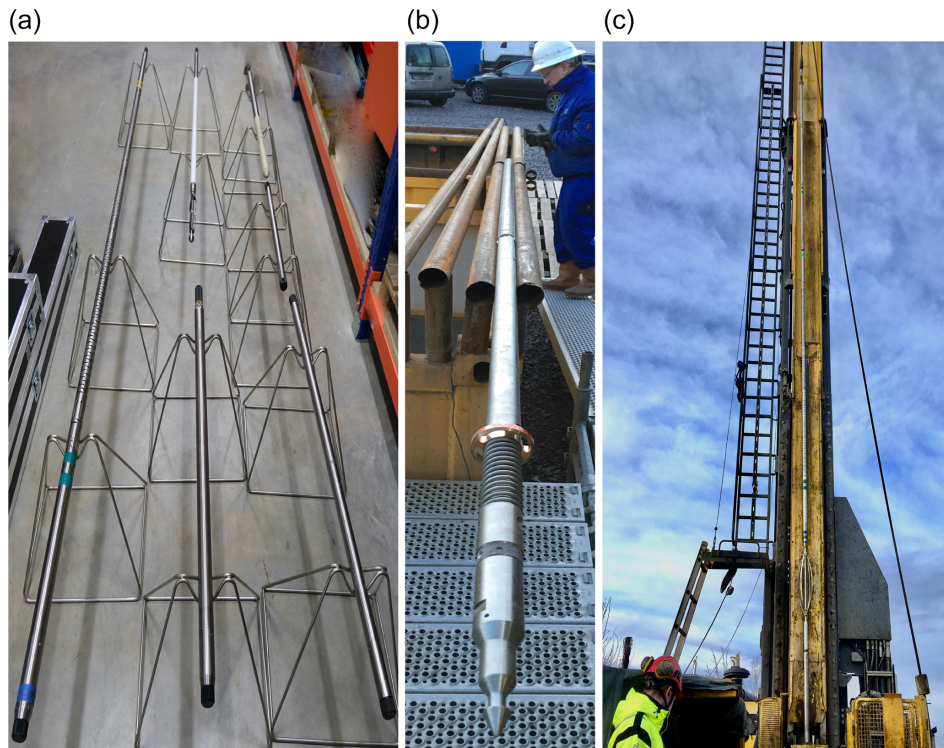
Figure 3. Sondes of the ICDP memory-logging system (iMLS): **(a)** mBCS, mDIL, mMS, MemBat, mTS, and mSGR (clockwise from left). **(b)** Landing unit with fishing spear head, spiral spring shock absorber, and brass landing plate. **(c)** The completely assembled iMLS tool string hanging in a wireline drill derrick before being dropped into a HQ drill string down to the coring bit at 500 m.
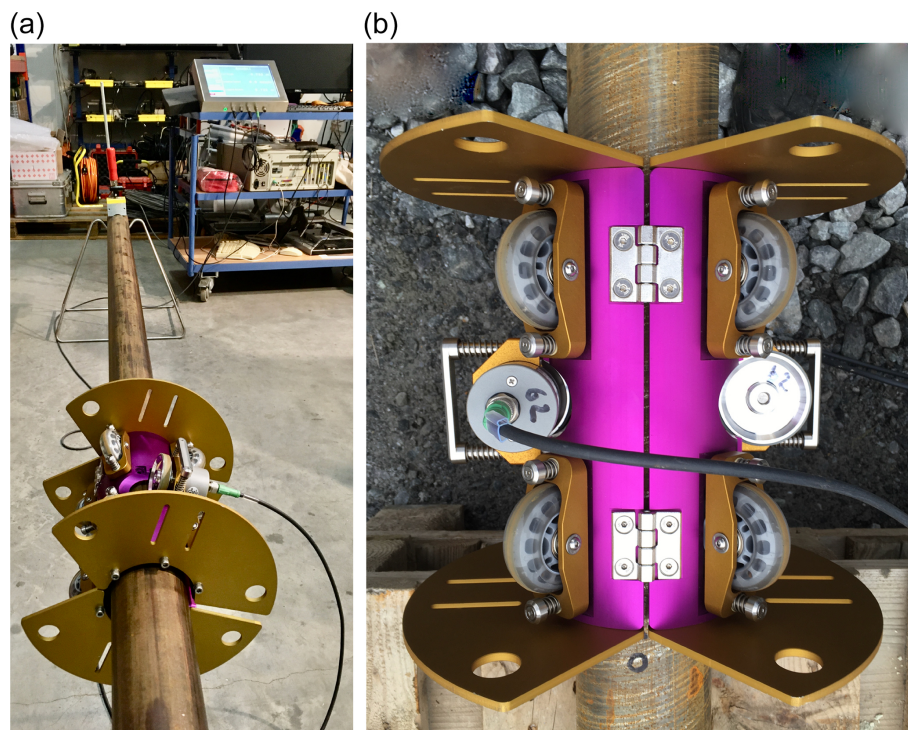

Figure 4. **(a)** A photo of the testing of the depth-measuring system iDMD-W mounted on a HQ drill pipe under lab conditions. **(b)** A close-up of the iDMD-W. The two depth-counting wheels are in the middle on opposite sides, and four of the eight guide wheels are visible above and below, all mounted on the magenta-colored sleeve. The brass-colored side flanges are used to attach the iDMD to the rig.

environmental conditions of up to 70 °C temperature and a maximum pressure of 50 MPa. This corresponds to a maximum depth of approximately 2–3 km in onshore drilling situations with a normal geothermal gradient.

The iMLS instrument package includes the key geophysical and technical parameters desired most frequently in scientific drilling:

- (MemBat) deviation from vertical – DEVI;

- (mSGR) spectrum of the natural gamma radiation – total GR, K, U, and Th;

- (mBCS) sonic velocity – full waveforms, Vp (Vs);

- (mMS) magnetic susceptibility – MSUS and TEMP;

- (mDIL) electric resistivity (induction) – Rmedium and Rdeep.

The minimum iMLS tool string is made up of the tool containing memory and battery (MemBat) and the mSGR tool, which is regularly crucial for precise core-to-log depth correction. The MemBat has a memory of 256 MB, equivalent to at least 500 h and provides a power supply of 12–15 VDC/24 Ah, equivalent to at least 50 h of recording with the maximum sonde stack. This is more than sufficient for every logging task within the depth range given by the tool specifications. The SGR sonde always remains positioned above the drill bit, i.e., within the drill pipe, because gamma rays do penetrate the steel pipe and the readings can be corrected for the attenuation. Sondes are typically combined in sonde stacks to minimize the number of logging runs and, hence, the required rig time. The minimum sonde stack of MemBat–mSGR can be combined with the other three sondes allowing for three longer sonde stacks: MemBat–mSGR–mBCS–mMS, MemBat–mSGR–mBCS–mDIL, and MemBat–mSGR–mMS (see Table 1).

The mSGR–mMS combination only protrudes 1.4 m out of the drill string bit and can, therefore, be used robustly in difficult borehole situations, even if the borehole is collapsed almost directly below the bit. The more fragile mDIL sonde is then only used in a second logging run, with the first run being utilized for hole condition reconnaissance. mBCS and mDIL are both used with in-line centralizers in the open hole. Another example of prioritization is lacustrine sediment logging with desired downhole parameters in a usual setup of (1) magnetic susceptibility and spectral gamma ray, (2) sonic velocity, and (3) electrical resistivity. Hence, the lowest risk choice for very difficult boreholes is the robust stack of mSGR and mMS; in less risky holes, the first run is the long stack mSGR–mBCS–mMS; and finally an mSGR–mDIL run may be utilized.

Besides being deployed using the drill string, the iMLS sondes can also be run in a borehole on any rope, slick line, or cable with a simple mechanical hook to still log in memory mode. It is a standard procedure to first run the mSGR alone on the coring wire line inside the drill string. This quickly yields a continuous total GR log that can be used for depth correlation of the logs from the subsequent LWT runs. The depth of this first log is determined independent of the driller depth-referenced LWT logs.

Furthermore, with a special additional wireline telemetry, the sondes can also be operated like normal logging sondes in wireline mode (online with real-time surface read-out). We made use of this additional feature in the field test and depth calibration test described below.

3.3   The iMLS depth-measuring device (iDMD)

In contrast to wireline logging, where a measuring wheel in the logging winch measures the length of the spooled cable directly while running the sondes in and out, the movement of the drill string first has to be measured precisely once it is tripped out for LWT. Several methods exist to do this. We developed two depth counters for the iMLS (1) because a ready-to-use depth device with LWT was not available on the market and (2) because we wanted to identify which of these two depth measurement methods is more practical, flexible, and robust under actual field conditions.

One depth counter works with a draw-wire sensor (iDMD-R, where R stands for rope) and the other works with measuring wheels (iDMD-W, where W stands for wheel). Both methods achieve an accuracy for the relative depth (length or traveled distance of the pipe movement) that compares very well to that of wireline logging (see below). However, the determination of the absolute LWT depth relies on the specification of the starting depth, i.e., the driller's depth of the bit before the start of the LWT. This depth is determined by the driller by measuring all drill string pieces on the pipe rack and adding them in the correct order during installation. Flawed pipe tallies cannot be excluded, meaning that the length of one or more pipe pieces may not have been counted, yielding a deeper bit position than the pipe tally indicates. As with any depth that is based on the driller's depth (e.g., bit depth, core depth, cuttings depth, and mud depth), the starting depth of the LWT also does not consider the lengthening of the drill string in the borehole due to its own weight. Accordingly, the obtained depth of the LWT is always less than the true depth. In the past, we have obtained differences between the wire line and driller's depth that varied by between almost zero in slim holes of only a few hundred meters depth and many meters in wide boreholes drilled for several kilometers with heavy pipe. However, during our new LWT measurements, the depth device reliably measured the true traveled distance of the already elongated drill string in the borehole.

Table 1. Technical specifications. mSGR refers to the spectrum of the natural gamma radiation – total GR, K, U, and Th; mBCS refers to borehole-compensated sonic velocity – full waveforms, Vp and Vs; mMS refers to the magnetic susceptibility and temperature; and mDIL refers to electric resistivity and induction – Rmedium and Rdeep.

Single ICDP memory-logging system (iMLS) tools	Length (m)	Weight (kg)	Diameter (mm)
All tools: maximum $T/p = 70\,°C/50\,MPa$			
Landing unit (LU)	1.7	16	50
MemBat	1.25	6.5	43
mSGR (cesium iodide crystal; vertical resolution of 0.2 m)	1.2	10.3	52
mBCS (T-R-R-T, short spacing; vertical resolution of 0.6 m)	3.9	27.2	52
mMS (magnetic susceptibility and temperature; vertical resolution of 0.2 m)	1.4	7.5	52
mDIL (vertical resolution of 0.8 m)	1.9	10	43
BCS–Cent (in-line centralizer for mBCS)	1.1	6	43–200
DIL–Cent (in-line centralizer for mDIL)	0.9	6	43–200
mTS (wireline telemetry for the memory sondes)	1.5	7	43
Possible iMLS sonde combinations	Total length (m)	Length below bit (m)	Weight (kg)
LU–MemBat–mSGR	4.15	0	22.5
LU–MemBat–mSGR–mMS	5.55	1.4	30
LU–MemBat–mSGR–mBCS–BCS–Cent	7.95	5	55.7
LU–MemBat–mSGR–mDIL–DIL–Cent	6.95	2.8	29.5
LU–MemBat–mSGR–mBCS–BCS–Cent–mMS	10.55	6.4	63.2
LU–MemBat–mSGR–mBCS–BCS–Cent–mDIL–DIL–Cent	11.95	7.8	62.7
Drill pipe and bit types	Rod body ID (mm)	Landing shoulder ID (mm)	Bit ID (mm)
HQ	77.8	74.1	63.5
HQ3	77.8	74.1	61.1

3.3.1 iDMD-R (rope)

With this device, the movement of the drill string is measured indirectly via the movement of the hook or the top drive. For this purpose, a robust draw-wire encoder (Kübler D120) is attached in the drill rig so that the up and down movements of the hook or the top drive can be measured. As both could also be moved without actually moving the drill string, e.g., when repositioning the top drive, this must be considered in the depth measurement. Therefore, another sensor registers whether the lower rod holder is open (pipe hangs in the top drive, iMLS moves along, and measurement is registered) or is closed (pipe hangs in the rod holder, iMLS does not move, and no movement is registered). A similar depth systems is used for LWD and for the heave compensation in some marine drilling situations. The installation of a draw-wire depth device in a drill rig has to be carefully planned and tested so as not to interfere with the driller's activities. In our logging tasks, we do not always encounter the same rig and

must instead contend with various drill rigs of very different sizes, constructions, and pipe handling types. Therefore, for the time being, we decided not to pursue this fragile and more difficult-to-adapt depth device, instead focusing on the development of a very small wheel-based device. However, we decided to keep our unperfected draw-wire device as a backup.

3.3.2 iDMD-W (wheel)

We designed the iDMD-W from scratch as a wheel-based depth measurement device that is basically comprised of two opposite wheels that are pressed directly onto the drill string (Fig. 4). In this sense, it measures very much like a wireline logging depth system that rides on the cable and records each movement of the cable at any time. These independent wheels continuously measure each movement and stoppage of the drill string passing through the depth device and, therefore, also those of the iMLS. Significant differences be-

tween the two readings make it possible to immediately recognize errors in the depth measurement. Errors could occur if a friction-reducing fluid caused the measuring wheels to occasionally slide on the drill string, which, in turn, would mean that the determined distances would be too short. In tests, one of the wheels was kept dry and the other wheel was moistened with water and with oil; these treatments did not cause any visible differences between the two length measurements. During measurement, the readings of both wheels are recorded and the larger value is chosen as the final depth output. This very compact and robust device is mounted like a sleeve around the drill string. The aluminum sleeve carries eight guide rollers and the two opposite measuring wheels. Due to its compactness, it can be installed in a position protected against damage between the top of the standpipe and the drill rod holder in a typical mining drill rig such as the ICDP DLDS (Deep Lakes Drilling System).

4   Field test and results

The technical functionality with respect to memory and wireline operation, pressure and temperature resistance, and handling of all iMLS sondes was verified in the 4000 m deep test borehole of the KTB Depth Laboratory (Harms and Kück, 2020).

The goal of the first full field utilization of the entire iMLS system was twofold: on the one hand, we aimed to check and improve the procedure that we had designed; on the other hand, we wished to examine the accuracy of the iMLS depth measurement method. The key operational objective was to exercise the complete LWT procedure for the first time, involving all components, and to compare the log depths obtained with those from subsequent wireline logging runs of the same memory sondes.

The field performance test was conducted during the active drilling operations at the 1000 m deep I-EDDA Test Center well (Almqvist et al., 2018). In cooperation with the drill rig operator, iMLS tests were carried out under realistic conditions in the depth range from 0 to 500 m. At the beginning of the test, the HQ core drill string was already installed in the hole with the coring bit at 500 m. First, a mechanical test was carried out with a dummy sonde, consisting of the landing unit and a solid steel bar with the dimensions and weight of an iMLS sonde string. After confirming the resilience and retrievability of the landing unit, the actual iMLS logging in memory mode was carried out along the depth section from 500 to 390 m with the long sonde combination of LU–MemBat–mSGR–mBCS–BCS–Cent–mMS (Fig. 3). A wheel-based depth counter prototype and the draw-wire device were used one after the other. The iDMD-W described above was not yet available at that time. The large size of the wheel-prototype only allowed for a mounting position between the rod holder and the top drive. Unfortunately, the prototype was rammed by the downward-moving top drive

after only 8 m of pipe tripping and became unusable, whereupon the iDMD-R was used. After the complete trip-out of the drill string, we ran the iMLS sondes in wireline mode in the open hole using a 600 m logging winch. We ran the same sonde stack as that used in LWT memory mode for the wireline mode logging. As the sondes and the logging speed were identical in memory and wireline logging, the logs show the same values and amplitudes, although their depth positions may have differed due to the very unequal depth-measuring method. The direct comparison of memory and wireline logs was then used to estimate the accuracy of the memory depth. The depth of the wireline log can be assumed to be almost equal to true depth because the TC1 hole is vertical and has a very smooth wall surface at these shallow depths.

When comparing wireline and memory logs, the memory depth first had to be shifted by a constant value using simple visual correlation due to the inexact starting depth information (drill bit depth) of the memory registrations. The magnetic susceptibility log (MSUS) was best suited to this task due to the almost complete reproduction of its profile in repeat measurements and its high vertical resolution of less than 0.1 m. Depth offsets for correction to the wireline depth were calculated as +4.6 m for the wheel prototype and +8.8 m for the iDMD-R. After this correction of the starting depth, the comparison of the wireline and the memory logs shows a remarkably good agreement of the depth of the measured curves (Fig. 5). The logs are only used here for the purpose of depth correlation. A detailed evaluation of these and additional geophysical logs along with core-derived data is the subject of ongoing investigations.

The excellent depth match is most evident in the high-depth-resolution curves of the magnetic susceptibility (MSUS), which almost overlay each other. The average depth difference is 0.2 m, which is in the order of the sample spacing of 0.1 m. Furthermore, the four parameters of the natural gamma ray spectrum sonde mSGR (total SGR; potassium, K; uranium, U; and thorium, Th) show a very good depth correlation of memory and wireline curves. All mSGR curves are corrected for the small hole size, and the memory curves are additionally corrected for the attenuation by the drill pipe. Slight differences in the curve shapes are due to the statistical nature of the natural gamma radiation as a product of radioactive decay. The P-wave velocity curves (Vp) of the sonic tool also show a good log–log correlation except for small divergences in a few short zones resulting from the difficult-to-process sonic waveform data.

The depth differences are less than 0.1 m along the 100 m long section. This demonstrates the ability of the iMLS depth devices to determine the movement of the sonde string in the borehole with the same accuracy and resolution as the classic wireline method. However, it also shows how immensely important the reliability of the exact starting depth reported by the driller is for LWT, without which an absolute LWT depth determination is impossible; for example, in lake drilling projects, the drop in the total GR at the lake floor
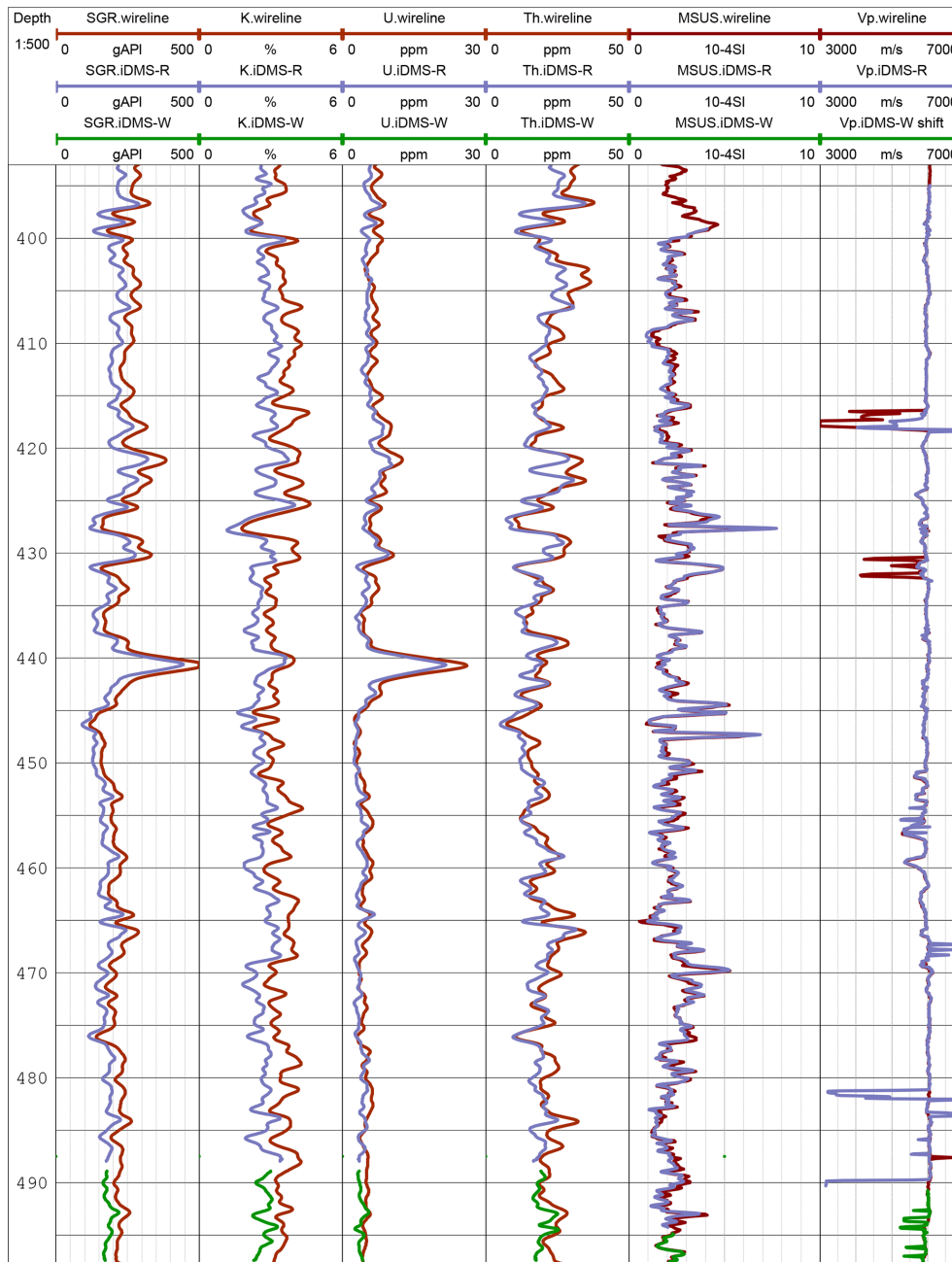
Figure 5. Depth (in meters) comparison of iMLS logging data from the wireline mode run (brown) and the memory mode run with two independent depth devices (green represents the iDMD-W prototype, and blue represents the iDMD-R) in the TC1 well, Örebro, Sweden. Depth differences between the wireline and memory mode are less than 0.1 m. Here, SGR denotes the parameter total gamma ray measured by the spectrum GR tool, and K, U, and Th are the contents of potassium, uranium, and thorium, respectively. All mSGR-derived curves are corrected for the effects of borehole size and steel casing. MSUS is the magnetic susceptibility, and Vp is the sonic P-wave velocity.

can sometimes be used as a reference, whereas in onshore drilling situations, this is not the case. As described above, differences of up to several meters between the bit depth notified by drillers and the wireline logger depth are common. For this reason, whenever possible, a wireline log of total gamma ray and magnetic susceptibility should be carried out

before an iMLS run. Even if only a short MSUS log length in the open hole is possible, the gained short profile can be used for depth correlation. A single total gamma ray would allow for a correlation, albeit a coarser one, in a case where a wireline sonde cannot run out of the bit at all. Logistically, a wireline pre-measurement will be possible in cases where

the iMLS serves as a backup for the primary preferred wireline measurements. This procedure is not possible in strongly inclined bores. Ultimately, even without an absolute depth reference (e.g., wireline depth), the LWT depth will instantaneously match the core depth, as both refer to the driller's depth.

Although our system is now basically ready for regular use in HQ and PQ holes, we will use both our iMLS and wireline logging systems in upcoming projects to carry out further tests of the depth-recording device in comparison to wireline logging in order to improve the iMLS performance and to verify the observed accuracy of the memory depth measurement on a broader statistical basis.

References

Abbott, M. B. and Rodbell, D. T.: Stratigraphic correlation and splice generation for sediments recovered from a large-lake drilling project: an example from Lake Junín, Peru, J. Paleolimnol., 63, 83–100, https://doi.org/10.1007/s10933-019-00098-w, 2020.

Aivalis, J., Meszaros, T., Porter, R., Reischman, R., Ridley, R.,Wells, P., Crouch, B. W., Reid, T. L., and Simpson, G. A.: Logging Through the Bit, Oilfield Review Summer 2012, 24, 44–53, 2012

Almqvist, B., Brander, L., Giese, R. Harms, U., Juhlin, C., Linde´n, C., Lorenz, H., and Rosberg, J.: I-EDDA test center for core-drilling and downhole investigations, EGU General Assembly 2018, 8–13 April 2018, Vienna, Austria, Geophysical Research Abstracts, 20, EGU2018-14837, 2018.

Baumgarten, H. and Wonik, T.: Cyclostratigraphic studies of sediments from Lake Van (Turkey) based on their uranium contents obtained from downhole logging and paleoclimatic implications, Int. J. Earth Sci., 104, 1639–1654, https://doi.org/10.1007/s00531-014-1082-x, 2015.

Beal, J.: Tight oil vertical log analysis applied to horizontal Logging While Tripping (LWT) data of Cretaceous-aged Viking formation, Saskatchewan, Canada: a multi-disciplinary review of initial and extended findings, AAPG Rocky Mountain Section Meeting, Cheyenne, WY, USA, 2019.

Freudenthal, T., Bohrmann, G., Gohl, K., Klages, J. P., Riedel, M., Wallmann, K., and Wefer, G.: More than ten years of successful operation of the MARUM-MeBo sea bed drilling technology: Highlights of recent scientific drilling campaigns, EGU General Assembly, Online Conference, 4–8 May 2020, SSP1.4, 2020.

Gebhardt, A. C., Francke, A., Kück, J., Sauerbrey, M., Niessen, F., Wennrich, V., and Melles, M.: Petrophysical characterization of the lacustrine sediment succession drilled in Lake El'gygytgyn, Far East Russian Arctic, Clim. Past, 9, 1933–1947, https://doi.org/10.5194/cp-9-1933-2013, 2013.

Goldberg, D.: The Role of Downhole Measurements in Marine Geology and Geophysics, Rev. Geophys., 35, 315–342, https://doi.org/10.1029/97RG00221, 1997.

Guerin, G. and Goldberg, D.: Heave compensation and formation strength evaluation from downhole acceleration measurements while coring, Geo-Mar. Lett., 22, 133–141, https://doi.org/10.1007/s00367-002-0104-z, 2002.

Hansen, R. R. and White, J.: Features of Logging-While-Drilling (LWD) in Horizontal Wells, SPE/IADC Drilling Conference, 11–14 March 1991, Amsterdam, the Netherlands, 21989-MS, https://doi.org/10.2118/21989-MS, 1991.

Harms, U. and Kück, J.: KTB Depth Laboratory: A Window into the Upper Crust, in: Encyclopedia of Solid Earth Geophysics, Encyclopedia of Earth Sciences Series, edited by: Gupta, H. K., https://doi.org/10.1007/978-3-030-10475-7_242-1, 2020.

Hodell, D., Anselmetti, F., Brenner, M., Ariztegui, D., and the PISDP Scientific Party: The Lake Petén Itzá Scientific Drilling Project, Sci. Dril., 3, 25–29, https://doi.org/10.2204/iodp.sd.3.02.2006, 2006.

Jackson, M. D., Gudmundsson, M. T., Weisenberger, T. B., Rhodes, J. M., Stefánsson, A., Kleine, B. I., Lippert, P. C., Marquardt, J. M., Reynolds, H. I., Kück, J., Marteinsson, V. T., Vannier, P., Bach, W., Barich, A., Bergsten, P., Bryce, J. G., Cappelletti, P., Couper, S., Fahnestock, M. F., Gorny, C. F., Grimaldi, C., Groh, M., Gudmundsson, Á., Gunnlaugsson, Á. T., Hamlin, C., Högnadóttir, T., Jónasson, K., Jónsson, S. S., Jørgensen, S. L., Klonowski, A. M., Marshall, B., Massey, E., McPhie, J., Moore, J. G., Ólafsson, E. S., Onstad, S. L., Perez, V., Prause, S., Snorrason, S. P., Türke, A., White, J. D. L., and Zimanowski, B.: SUSTAIN drilling at Surtsey volcano, Iceland, tracks hydrothermal and microbiological interactions in basalt 50 years after eruption, Sci. Dril., 25, 35–46, https://doi.org/10.5194/sd-25-35-2019, 2019.

Jerram, D. A., Millett, J. M., Kück, J., Thomas, D., Planke, S., Haskins, E., Lautze, N., and Pierdominici, S.: Understanding volcanic facies in the subsurface: a combined core, wireline logging and image log data set from the PTA2 and KMA1 boreholes, Big Island, Hawaiʻi, Sci. Dril., 25, 15–33, https://doi.org/10.5194/sd-25-15-2019, 2019.

Koeberl, C., Milkereit, B., Overpeck, J. T., Scholz, C., Amoako, P. Y. O., Boamah, D., Danuor, S., Karp, T., Kück, J., Hecky, R. E., King, J. W., and Peck, J. A.: An international and multidisciplinary drilling project into a young complex impact structure: The 2004 ICDP Bosumtwi Crater Drilling Project – An overview, Meteorit. Planet. Sci., 42, 483–511, 2007.

Matheson, R. and West, J.: Logging While Tripping – A New Alternative in Formation Evaluation, J. Can. Petrol. Technol., 39, 38–43, https://doi.org/10.2118/00-07-02, 2000.

Moore, J. C.: Synthesis of results: logging while drilling, northern Barbados accretionary prism, in: Proc. ODP, Sci. Results, 171A: College Station, TX (Ocean Drilling Program), edited by: Moore, J. C. and Klaus, A., 1–25, https://doi.org/10.2973/odp.proc.sr.171a.101.2000, 2000.

Singh, M., Al Benali, K., A., Sallam, Y., Sajeel, K., El Wazeer, F., Chaker, H., and Propper, M.: A Case Study on Open-Hole Logging While Tripping LWT Through Drill Pipes, as a New Technology for Risk Mitigation and Cost Optimization in Abu Dhabi Onshore Fields, Society of Petroleum Engineers, SPE-193315-MS, https://doi.org/10.2118/193315-MS, 2018.

Scientific Drilling

Open Access

Potential microbial contamination from drilling lubricants into subseafloor rock cores

H. Lizethe Pendleton[1], **Katrina I. Twing**[1,a], **Shahrzad Motamedi**[1], **and William J. Brazelton**[1]

[1]School of Biological Sciences, University of Utah, Salt Lake City, 84112 USA
[a]current address: Department of Microbiology, Weber State University, Ogden, 84408 USA

Correspondence: William J. Brazelton (william.brazelton@utah.edu)

Abstract. International Ocean Discovery Program (IODP) Expedition 357: "Serpentinization and Life" drilled shallow cores into the Atlantis Massif near the Mid-Atlantic Ridge in October 2015 using seabed drills. Serpentinization and other geochemical processes occurring within the Atlantis Massif release hydrogen, methane, and other chemicals that can potentially fuel microorganisms through chemosynthesis. The subseafloor rock cores collected during IODP Exp. 357 are the first of their kind, meaning the analysis and interpretation of these samples required new methodologies, including a specialized approach for distinguishing endemic subsurface inhabitants from potential contaminants from various sources. Background samples of various potential contamination sources were collected during sampling: 109 samples of seawater collected before, during, and after drilling; 20 samples of greases and oils associated with the drilling equipment; and samples of the laboratory's ambient air. Despite the widespread usage of drilling lubricants and the importance of controlling contamination in drill-core samples for microbiological analyses, no studies to date have looked at DNA in drilling greases and oils. In this study, drilling lubricants were analyzed as possible sources of microbial contamination of subseafloor rock core samples by environmental sequencing of 16S rRNA genes. We find that microbial signatures from drilling lubricants are only found in low abundance in seafloor samples (at most a few percent of total sequence counts), with laboratory contaminants being a greater source of contamination.

1 Introduction

Due to the low biomass of many subsurface habitats (Kallmeyer, 2017; Smith et al., 2000b), there is a need for improved quality control metrics in order to distinguish between endemic microbial communities and those introduced through contamination (Friese et al., 2017; Smith et al., 2000b; Wilkins et al., 2014; Kallmeyer 2017; Yanagawa et al., 2013; Santelli et al., 2010; Smith et al., 2000b). Contamination of drill core samples can occur from multiple sources before, during, and after drilling. Tracers introduced during drilling (e.g., Friese et al., 2017; Kallmeyer, 2017; Kallmeyer et al., 2006; Lever et al., 2006; Smith et al., 2000a; Yanagawa et al., 2013) are an essential tool for tracking environmental contamination that occurs during drilling, but such tracers cannot identify all possible sources of contamination. Methods for tracking and monitoring the level of contamination introduced during drilling can be generally grouped

into three categories: (1) particle tracers (e.g., microspheres), (2) chemical or dissolved tracers (e.g., perfluorocarbon compounds such as perfluoromethylcyclohexane – PFC), and (3) microbiological analyses (e.g., 16S rRNA, fatty acids) (Kallmeyer et al., 2006). Depending on the choice of tracer, various techniques can be used to determine the level of contamination of the drill core samples.

The Lost City is an iconic hydrothermal vent system located on the Atlantis Massif, near the Mid-Atlantic Ridge and Atlantis Fracture Zone (Kelley et al., 2005). The Atlantis Massif is a site of active seafloor serpentinization, and hydrothermal fluids venting through the Lost City chimneys contain products of serpentinization reactions, including hydrogen and methane gas, that can fuel chemoautotrophic microorganisms (Kelley et al., 2005; Lang and Brazelton, 2020). During International Ocean Discovery Program (IODP) Expedition 357: "Serpentinization and Life",

shallow rock cores were drilled in several locations along the Atlantis Massif to recover serpentinite cores where serpentinization is actively occurring, using seabed drills (Früh-Green et al., 2018). Seabed drills differ from traditional platform drilling as they are lowered directly to the drilling site and use bottom seawater as the drilling fluid instead of fluid from a non-indigenous source (Freudenthal and Wefer, 2007). Two seabed drills were used on the Royal Research Ship *James Cook* for this expedition: RD2 (British Geological Survey) and MARUM-MeBo70 (Center for Marine Environmental Sciences at the University of Bremen) (Früh-Green et al., 2017a; Freudenthal and Wefer, 2007). IODP Exp. 357 employed the use of the synthetic tracer PFC (Smith et al., 2000b) mixed into flushing seawater in an effort to assess the level of contamination introduced into the cores (Orcutt et al., 2017).

The subseafloor rock cores collected during IODP Exp. 357 are the first oceanic crust samples to be collected with seabed drills and suitable for microbiology, so the analysis and interpretation of these samples required the development of new methodologies, including a specialized approach for distinguishing true subsurface microbial inhabitants from surface contaminants (Motamedi et al., 2020). In addition to investigating seawater and lab air as potential sources of contamination of the core samples, the industrial oils and greases used during the drilling process and which potentially came into direct contact with the core samples were previously examined as potential sources of organic molecule contaminants (Hickok et al., 2018). Here, we report an investigation of potential microbial contamination in these same greases and oils, as measured by DNA sequencing.

2   Methods

2.1   Sample collection and processing

Drill core and seawater samples were collected during IODP Exp. 357 and are described in detail in Motamedi et al. (2020). Briefly, core subsamples identified for microbiological analyses were immediately retrieved from the drill upon its return to the ship deck, wrapped in acid-washed and autoclaved teflon, and stored at $-80\,°C$. Core samples were then shipped to the Kochi Core Center (Japan) for further processing and subsampling under sterile conditions (Früh-Green et al., 2017b; Orcutt et al., 2017). Please see Früh-Green et al. (2017a, 2018) for more details on lithology and other details of the recovered cores.

Prior to the deployment of the drill at each site, the ship's conductivity, temperature, and depth (CTD) Niskin bottle rosette was cast to collect a water-column profile, with six 10 L bottles being triggered approximately 2–3 m above the seafloor and three 10 L bottles collected at even intervals throughout the water column (Früh-Green et al., 2017b). Additionally, a 4 L bucket was used to collect surface seawater

surrounding the ship. Ten-liter Niskin bottles were also attached to each drill and were used to collect bottom seawater during and immediately after drilling. A total of 109 seawater samples were collected during IODP Exp. 357. All seawater samples were filtered with a peristaltic pump through $0.22\,\mu m$ Sterivex™ filters onboard the ship and stored at $-80\,°C$ until DNA extraction (Motamedi et al., 2020).

The drill grease and oil samples were collected in sterile 15 mL tubes directly from their original product packaging. Additionally, one methanol-soaked filter used to wipe down a stainless-steel core liner, plastic shards shaved from a plastic core liner, and samples of spray paint that were used on the drill were collected. These samples were all stored at $-80\,°C$ until extraction. Two sets of these samples were collected, one for testing of organic chemical contamination (Hickok et al., 2018) and the other for microbial contamination testing, described here. All grease/oil extractions took place in a HEPA-filtered room using an aseptic technique. The lab bench was wiped down with 80 % ethanol prior to each set of extractions. Lab air samples were collected by filtering air through 0.1 μm Puradisc 25 mm PTFE syringe filters (GE Healthcare Whatman, Pittsburgh, Pennsylavania, USA) by a dual-head Air Cadet Model 420-2901-00FK (Thermo Fisher Scientific, Waltham, Massachusetts, USA). The lab air was vacuumed through a total of three different filters for 9 h each and was combined during DNA extraction. DNA extraction and purification were performed using the same protocols and reagents as outlined in Motamedi et al. (2020).

2.2   DNA extraction and purification

Test DNA extractions were performed to determine the best protocol for use on the industrial grease and oil samples. For the test samples, LMX "Red" Grease (Plews & Edelmann, IL, USA), WD-40 spray (CA, USA), and mineral oil were selected for their accessibility and similarity to industrial grade oils and greases used during IODP Exp. 357. The quality and quantity of extracted DNA from six different protocols were evaluated (Table 1). Two sets of extractions were performed: the first set were unaltered test samples and the second set were spiked with 10 μL of a turbid suspension of *E. coli* cells to assess DNA recovery. Once the samples were extracted, both sample sets underwent DNA purification via 2x SPRI beads (Rohland et al., 2012). After each step in the purification process, the samples were quantified with a Qubit fluorometer (Invitrogen, CA, detection limit of $50\,ng\,mL^{-1}$) and NanoDrop spectrophotometer (Thermo Fisher Scientific, MA) to assess DNA quantity and quality (Table 1). Of the six DNA-extraction methods, the FastDNA® SPIN Kit (Qbiogene Inc., CA) was the only method to yield DNA from all three test samples.

DNA was isolated from the Exp. 357 grease and oil samples using the FastDNA® SPIN Kit according to manufacturer recommendations, except that a Mini-Beadbeater-16 (Biospec Products, OK) was used in place of the FastPrep®

Table 1. Comparison of DNA-extraction methods with three test samples. Six DNA-extraction methods were compared on three test samples (WD-40, mineral oil, and LMX "Red" grease), chosen for their similar properties to industrial grade lubricants. The test samples were spiked with *E. coli* cells. All DNA yields from un-spiked test samples were below the detection limit (BDL). Each column shows the total amount of DNA extracted (ng).

Extraction method	WD-40	Mineral oil	LMX "Red" Grease
	Total ng	Total ng	Total ng
MP FastDNA® SPIN Kit	7.1	5.8	6.2
MoBio PowerLyzer	BDL	BDL	BDL
MoBio PowerSoil	BDL	10.5	BDL
Wizard® Magnetic DNA Purification system for food	6.5	5.5	BDL
Phenol: chloroform (Brazelton et al., 2017)	8.6	15.5	BDL
ZR Fecal DNA MiniPrep	BDL	BDL	BDL

instrument. The quantity of starting material for the extraction ranged from 0.25 to 1.0 g (Table 2). Extracted DNA was purified via 2x SPRI beads (Rohland et al., 2012). If replicate extractions of the same sample were possible, the extracted DNA from those replicates was pooled together during the DNA purification step. Additionally, six blank samples of Invitrogen UltraPure™ distilled water were extracted alongside the grease and oil samples as an additional precaution to test for kit contamination, potential contamination introduced during the extraction process, and sequencing contamination (Salter et al., 2014). The extraction of DNA from rock core, seawater, and laboratory air samples was previously described in detail in Motamedi et al. (2020).

2.3 Sequencing and analysis of 16S rRNA genes

Purified DNA preparations from IODP Exp. 357 rock cores, seawater, laboratory air, and greases and oils were sent to the Michigan State University Research and Technology Support Facility Genomics Core for sequencing of the V4 region of the 16S rRNA gene using the duel-indexed Illumina fusion primers 515F-806R (Kozich et al., 2013). All grease and oil samples were submitted for sequencing twice (i.e., sequencing replicates), and the results from both replicates are included in our analysis, with the exception of a single sample, GREd003, one replicate of which was determined to have been compromised during sequencing. Sequences from seawater and rock core samples were previously reported in Motamedi et al. (2020). Analysis of the 16S rRNA gene amplicon sequences from the greases and oils, rock cores, seawater, laboratory air, and extraction blanks was conducted with the mothur (v.1.39.5) software platform (Schloss et al.,

2009). Sequences with > 8 homopolymers and > 0 ambiguous bases were removed from downstream analyses, and the sequences were then pre-clustered with the mothur command pre.cluster (diffs $= 1$) to remove rare sequences most likely created by sequencing errors (Schloss et al., 2011). Operational taxonomic units (OTUs) were formed with a 97 % similarity threshold using the VSEARCH DGC clustering algorithm (Rognes et al., 2016) in mothur. Of the 31 406 783 paired sequences, 75 189 OTUs were identified among the greases and oils, seawater, rock cores, laboratory air, and extraction blanks. Taxonomic classification of all OTUs was performed with mothur using the SILVA reference alignment (SSURefv132) and taxonomy outline (Pruesse et al., 2012). The proportion of contamination from seawater, laboratory air, or industrial grease and oil into each rock core sample was estimated using SourceTracker2 v.2.0.1 (Knights et al., 2011). All sequence data are available via NCBI SRA Bio-Project PRJNA575221.

3 Results and discussion

3.1 DNA-extraction tests for industrial greases and oils

To our knowledge, the extraction of DNA from industrial greases and oils has not been previously published, either in the context of scientific drilling projects or in other uses of industrial lubricants. DNA-extraction protocols have been published for testing the integrity of food oils such as olive oil (Busconi, et al., 2003; Consolandi, et al., 2008; Testolin and Lain, 2005) and soybean oil (Pauli et al., 1998), but not industrial oils. Multiple DNA-extraction protocols were evaluated for this study using three test samples (LMX "Red" Grease, WD-40 spray, and mineral oil) that were spiked with *E. coli* cells before DNA extraction. The MPBio FastDNA® SPIN Kit (Qbiogene, Inc., CA) was the only method able to extract detectable DNA from all three of the test samples (Table 1). Extractions from these test samples highlighted viscosity as a key challenge for adapting extraction protocols for greases and oils. In general, less viscous oils were easier to extract than the more viscous grease samples due to difficulties in implementing the physical lysing of thick greases. 16S rRNA gene amplicon sequencing of the spiked test samples confirmed that the recovered DNA was dominated by *E. coli* (data not shown).

3.2 Microbial composition of grease and oil samples

To assess the potential of drilling equipment to introduce contamination into drill core samples, we collected 20 samples of greases, oils, plastic shards, spray paint, and a cotton filter that wiped a stainless-steel core liner, all of which were used during IODP Exp. 357 (Table 2). All materials that were sampled had some interaction with the drills and introduced a potential for contamination into the rock cores. Six samples of Invitrogen UltraPure™ distilled water were extracted

Table 2. Description and DNA concentration of drill-associated samples. Twenty samples were taken during the duration of the cruise, including grease, oil, plastic shards, spray paint, and a cotton filter liner. Total DNA (ng) values represent measurements post DNA purification.

Sample name	Sample type	Drill	Purpose/location on drill	Amount extracted	DNA (ng)
0GREd001	Atlantis 22 hydraulic oil	RD2	Hydraulic oil used in both MeBo and RD2 drills	1.0 g	BDL
0GREd002	MeBo transformer fluid	MeBo	Used on MeBo drill	1.0 g	BDL
0GREd003	Loclite 638	RD2	Used on the threads of the drill rods	1.0 g	BDL
0GREd004	K Nate BGS drill	RD2	On bolts and drill rods	0.50 g	BDL
0GREd005	B30 transformer oil	RD2	Used on RD2 drill	1.0 g	BDL
0GREd006	Contact grease	RD2	Located on electrical connections	1.0 g	BDL
0GREd007	MeBo Anti-Seize	MeBo	Greases threads at the top of the core barrel	1.0 g	6.25
0GREd008	MeBo Aqua Shield	MeBo	Greases threads at the top of the core barrel	0.50 g	5.25
0GREd009	RD2 grease	RD2	Used on RD2 drill	0.25 g	BDL
0GREd010	Fincox GC Mei Belpask	MeBo	Greased threads of the rods	1.0 g	7.55
0GREd011	Tuflube	RD2	Launch and recovery system on drill	0.75 g	5.35
0GREd012	Saphire Aqua 2	RD2	Launch and recovery system on drill	0.75 g	3.18
0GREd013	MeBo seawater grease	MeBo	Used on core lifter case and core breaker	0.75 g	2.56
0GREd014	Brit Lube	RD2	Drill rods, packers	0.75 g	1.72
0GREd015	Umbilical cord grease	RD2	Used to lubricate umbilical cord for RD2 drill	0.50 g	40.4
0GREd016	Atlantis 22 hydraulic oil	MeBo	Hydraulic oil used in both drills	1.0 g	5.4
0GREd017	Panolin hydraulic oil	MeBo	Used on MeBo drill	1.0 g	6.3
0GREd018	Plastic shard liner	Cut from core liner	Shards from the plastic core liners	3 thin strips	BDL
0GREd019	Split cotton liner	MeBo	Wiped down core liner with methanol-soaked filter	One liner	BDL
0GREd020	Spray paint	RD2	Dried spray paint located on drill and flaked off	0.25 g	BDL

alongside the grease and oil samples to account for any possible contamination introduced from the DNA-extraction kit or during the extraction and sequencing process.

From these 26 samples, we obtained a total of 4 339 588 paired sequences of 16S rRNA gene amplicons, which were clustered into 5629 OTUs at a 97 % sequence similarity threshold. Any OTUs detected in the DNA-extraction blank samples were removed from the dataset, leaving 4694 OTUs (Table S1 in the Supplement). Gammaproteobacteria constituted the highest percentage of taxa in the oil and grease samples (32 % of total sequences; Fig. 1), and the most abundant Gammaproteobacteria OTUs could not be classified below the class level (Table S1). Alphaproteobacteria (17 % of total sequences) were primarily represented by Sphingomonadaceae, Rhodobacteraceae, and Acetobacteraceae. Bacteroidia (10 % of total sequences) were primarily represented by Flavobacteriaceae, Spirosomaceae, and Hymenobacteraceae. Betaproteobacteriales (4 % of total sequences, but note that Betaproteobacteriales are classified as an order within class Gamamproteobacteria in the SILVA taxonomy) were dominated by various genera of the Burkholderiaceae.

DNA sequences in the oils and greases had high similarity to sequences from a wide range of environments, including soil (e.g., NCBI accessions HM104622, MG716681, AM940870, KP786168, NR_163645), glaciers (HQ333317, MN880348), lake sediments (MT067094), a geothermal plant (KY077452), a shallow marine hydrothermal vent (GU369930), and seawater (JN233022, KX177824). Se-
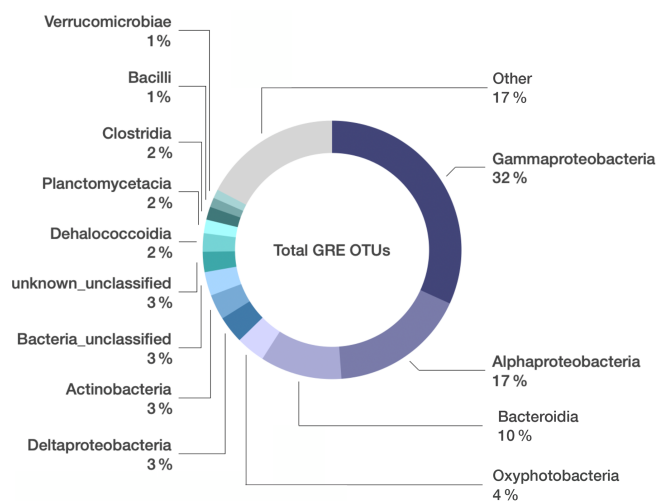

Figure 1. Microbial composition unique to grease and oil samples used on seafloor drills. Relative abundance of bacterial classes identified in grease and oil samples. Sequences that were also present in the controls (extraction kit blank, lab air, and MilliQ water) were manually removed from the dataset. "Other" includes 95 additional classes whose relative abundance was < 1 % of the total community composition.

quences associated with petroleum-contaminated environments were also identified (EU328045, KY190357). Many of the matching sequences were associated with drilling projects, such as an IODP borehole (KR072759), marine

sediments (CP004387, MF977474), a continental borehole (KP901594), and groundwater wells (KC606558). A few OTUs obtained from a swipe of a core liner barrel matched those from continental subsurface studies (MT067098, HM185963, HM641526). Notably, several OTUs that were abundant in the grease that is used on RD2's umbilical cord were nearly identical to clones from a deep-sea drilling and coring contamination study (Yanagawa et al., 2013), notably including those recovered from the drilling fluid in that study (e.g., AB824901). A summary of best sequence matches is provided in the Supplement (Table S2).

3.3 Potential oil and grease contamination of seawater samples

All of the most abundant grease/oil OTUs were also identified in samples of seawater collected during the expedition. Because the greases and oils were sampled directly from their commercial product packages (except for the core liner swab and paint chips), contamination from seawater into the grease/oil samples seems unlikely. The grease/oil OTUs that are most abundant in seawater samples were almost exclusively derived from GREd008 (AquaShield, lubrication for MeBo core barrel threads) and GREd015 (RD2 umbilical cord grease). Furthermore, seawater samples collected with Niskin bottles mounted on MeBo and RD2 were especially likely to contain OTUs from the AquaShield grease (Table S1). However, overall, these potential grease/oil contaminants represent a small fraction of the total sequence dataset from seawater (< 1 % of all sequence counts).

3.4 Minimal oil and grease contamination of rock cores

The rock core samples collected during IODP Exp. 357 were exposed to potential contamination sources before, during, and after drilling (Fig. 2). The extent of DNA contamination from seawater into the rock cores was investigated by Motamedi et al. (2020), and here, we extend that analysis to include grease and oil samples as additional potential sources of contamination.

Of the 4694 OTUs identified in all grease and oil samples, 565 OTUs were also identified in at least one rock core sample from IODP Exp. 357 (Table S3). However, 86 of these OTUs were also identified in samples of the ambient lab air, suggesting that some of these sequences represent general contamination from dust particles during laboratory handling. In addition, the taxonomic classifications of many of these OTUs suggest that they are derived from commercial reagents (e.g., Burkholderia) or the human microbiota (e.g., Enterobacteriaceae), based on previous studies (Sheik et al., 2018; Salter et al., 2014), even though they were not detected in the extraction blanks or ambient lab air during our study. OTUs that are suspected to be contaminants on the basis of their taxonomic classification are highlighted in (but not removed from) the tables in the Supplement.
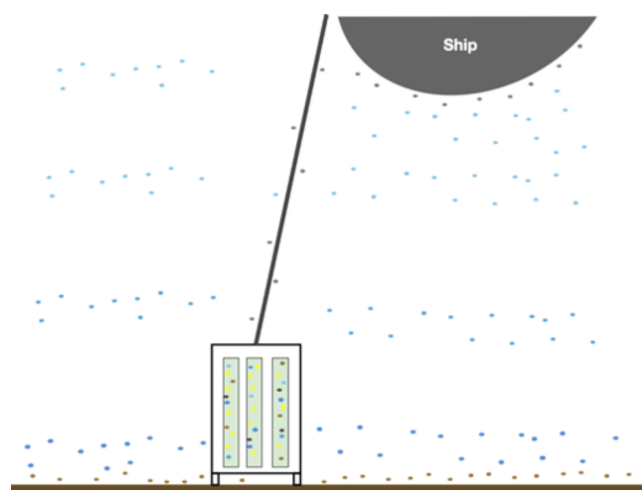

Figure 2. Illustration of various microbial communities present in the sampling environment. The different colored dots represent microbes from varying depth ranges in the water column (shades of blue) as well as microbes surrounding the ship, drill, and drill line (grey), microbes at the water–sediment interface, and the actual subsurface microbes (yellow) that live in the rock cores. The blue, grey, and brown dots represent the potential for contamination to the subsurface rock cores and illustrate the need for rigorous contamination testing.

The remaining 479 OTUs that represent potential grease/oil contaminants of the rocks (Table S3) comprise 16 % of the total OTUs and 24 % of the total sequence counts in the rock core samples. However, most (90 %) of these sequence counts in rocks are contributed by OTUs that were found in low abundance in our samples of greases and oils (< 100 total counts across all GRE samples), casting doubt that the greases and oils were the source of most of these contaminants into the rock cores. Abundant OTUs from greases and oils were generally very rare in the rock cores.

We estimated the proportion of DNA sequences from each rock core sample that could be attributed to each potential source of contamination (i.e., seawater, laboratory air, or drill grease and oil) using SourceTracker2 (Fig. 3). OTUs with "unknown" sources could not be assigned to a single contamination source and may represent true inhabitants of the rock cores. Lab air was the largest source of contamination into the rock cores, and contamination from other sources was minimal. Greases and oils were estimated to contribute at most a few percent of the sequences in each rock core sample, and their contribution was nearly zero in many of the samples. Nevertheless, the detectable levels of contamination from grease/oil and seawater are notable, considering the extensive precautions employed during handling and processing of the rock core samples (Früh-Green et al., 2017a, 2018; Hickok et al., 2018; Motamedi et al., 2020). These precautions (including the use of bottom seawater as the drilling fluid, immediate freezing of core samples, and shaving of

Table 3. Condensed phylogenetic table of S4 showing the 27 most likely contaminant OTUs from the grease and oil samples.

| Phylum	Class	Order	Family	Genus	Most abundant in sample of
Acidobacteria	Blastocatellia_(Subgroup_4)	Blastocatellales	Blastocatellaceae	Blastocatellaceae_unclassified	Umbilical cord grease
Actinobacteria	Actinobacteria	Corynebacteriales	Corynebacteriaceae	Turicella	Panolin hydraulic oil
Chloroflexi	Chloroflexia	Thermomicrobiales	JG30-KF-CM45	JG30-KF-CM45_ge	Umbilical cord grease
Cyanobacteria	Oxyphotobacteria	Nostocales	Nostocales_unclassified	Nostocales_unclassified	B30 transformer oil
Cyanobacteria	Oxyphotobacteria	Oxyphotobacteria_Incertae_Sedis	Unknown_Family	Calothrix_KVSF5	MeBo seawater grease
Firmicutes	Bacilli	Bacillales	Planococcaceae	Planococcaceae_unclassified	Loclite 638
Firmicutes	Clostridia	Clostridiales	Clostridiaceae_1	Clostridium_sensu_stricto_1	Atlantis 22 hydraulic oil
Firmicutes	Clostridia	Clostridiales	Family_XI	Anaerococcus	MeBo transformer fluid
Firmicutes	Clostridia	Clostridiales	Lachnospiraceae	Lachnospiraceae_unclassified	Atlantis 22 hydraulic oil
Firmicutes	Clostridia	Clostridiales	Lachnospiraceae	Tyzzerella_3	Contact grease
Firmicutes	Clostridia	Clostridiales	Peptostrepto-coccaceae	Romboutsia	Atlantis 22 hydraulic oil
Firmicutes	Clostridia	Clostridiales	Ruminococcaceae	Ruminococcaceae_unclassified	MeBo transformer fluid
Firmicutes	Clostridia	Clostridiales	Ruminococcaceae	Ruminococcaceae_unclassified	MeBo seawater grease
Proteobacteria	Alphaproteobacteria	Rhizobiales	Xanthobacteraceae	Xanthobacteraceae_unclassified	MeBo Anti-Seize
Proteobacteria	Alphaproteobacteria	Rhodobacterales	Rhodobacteraceae	Rhodobacter	Spray paint
Proteobacteria	Gammaproteobacteria	Betaproteobacteriales	Nitrosomonadaceae	DSSD61	Atlantis 22 hydraulic oil
Proteobacteria	Gammaproteobacteria	Nitrosococcales	Nitrosococcaceae	wb1-P19	MeBo Aqua Shield
Proteobacteria	Gammaproteobacteria	Oceanospirillales	Alcanivoracaceae	Alcanivorax	Atlantis 22 hydraulic oil
Proteobacteria	Gammaproteobacteria	Pseudomonadales	Moraxellaceae	Alkanindiges	MeBo Aqua Shield
Proteobacteria	Gammaproteobacteria	Xanthomonadales	Xanthomonadaceae	Pseudoxanthomonas	K Nate BGS drill
Proteobacteria	Gammaproteobacteria	Xanthomonadales	Xanthomonadaceae	Pseudoxanthomonas	Plastic shard liner
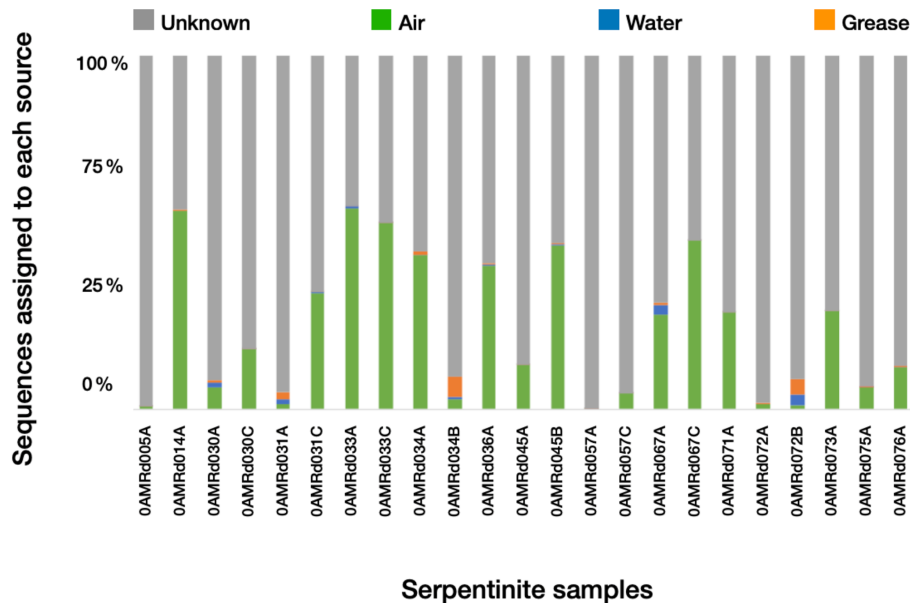
Figure 3. Estimated sources of DNA sequences into rock core samples. SourceTracker2 (Knights et al., 2011) was used to identify the most likely source of OTUs into the rock cores. Possible sources were laboratory air (green), seawater (blue), or drilling grease or oil (orange). OTUs with an "unknown" source could not be assigned to a single source and may represent rock-hosted microbes.

core exteriors with a sterile rock saw in a dedicated facility) are not practical for many drilling projects, suggesting that these contamination levels may be higher in other studies.

We assembled a final list of 27 likely contaminant OTUs from greases and oils (Table S4 and summarized in Table 3) based on their absence in extraction blanks and lab air and their much higher abundance in greases and oils compared to seawater (i.e., $> 5 \times$ greater abundance and > 500 total counts in greases and oils; see Table S3 for numbers). These likely contaminants were mostly derived from GREd001 (hydraulic oil used on both RD2 and MeBo) and GREd015 (RD2 umbilical cord grease) and were also moderately abundant in GREd004 (K Nate grease), GREd006 (electrical contact grease), and GREd008 (AquaShield grease). They represent 8 phyla and 10 classes, with Clostridia the most frequently appearing. As noted in Sect. 3.2, the most abundant of these sequences had high similarity to database sequences reported from a wide range of environments.

4   Conclusions

The possibility of contaminant DNA introduced by greases and oils associated with drilling equipment had not been previously explored. We have demonstrated that DNA can be detected in industrial greases and oils and that these same DNA sequences can also be found at low levels in low-biomass rock cores and in seawater samples. Nevertheless, our results indicate that, for our study, contamination from greases and oils was much less prevalent compared to contamination during laboratory handling, as measured by DNA extracted

from dust particles in ambient lab air. Even though we do not expect greases and oils to be the most important source of contamination in most studies, levels of contamination from different sources will vary according to the particular circumstances of each project. Therefore, we recommend that future studies should monitor potential contamination from greases and oils associated with drilling and sampling equipment.

References

Brazelton, W. J., Thornton, C. N., Hyer, A., Twing, K. I., Longino, A. A., Lang, S. Q., Lilley, M. D., Früh-Green, G. L., and Schrenk, M. O.: Metagenomic identification of active methanogens and methanotrophs in serpentinite springs of the Voltri Massif, Italy, PeerJ, 5, e2945, https://doi.org/10.7717/peerj.2945, 2017.

Busconi, M., Foroni, C., Corradi, M., Bongiorni, C., Cattapan, F., and Fogher, C.: DNA extraction from olive oil and its use in the identification of the production cultivar, Food Chem., 83, 127–134, https://doi.org/10.1016/S0308-8146(03)00218-8, 2003.

Consolandi, C., Palmieri, L., Severgnini, M., Maestri, E., Marmiroli, N., Agrimonti, C., Baldoni, L., Donini, P., De Bellis, G., and Castiglioni, B.: A procedure for olive oil traceability and authenticity: DNA extraction, multiplex PCR and LDR – universal array analysis, Eur. Food Res. Technol., 227, 1429–1438, https://doi.org/10.1007/s00217-008-0863-5, 2008.

Freudenthal, T. and Wefer, G.: Scientific Drilling with the Sea Floor Drill Rig MeBo, Sci. Dril., 5, 63–66, https://doi.org/10.2204/iodp.sd.5.11.2007, 2007.

Friese, A., Kallmeyer, J., Kitte, J. A., Martínez, I. M., Bijaksana, S., and Wagner, D.: A simple and inexpensive technique for assessing contamination during drilling operations, Limnol. Oceanogr.-Meth., 15, 200–211, https://doi.org/10.1002/lom3.10159, 2017.

Früh-Green, G. L., Orcutt, B. N., Green, S. L., Cotterill, C., Morgan, S., Akizawa, N., Bayrakci, G., Behrmann, J.-H., Boschi, C., Brazelton, W. J., Cannat, M., Dunkel, K. G., Escartin, J., Harris, M., Herrero-Bervera, E., Hesse, K., John, B. E., Lang, S. Q., Lilley, M. D., Liu, H.-Q., Mayhew, L. E., McCaig, A. M., Menez, B., Morono, Y., Quéméneur, M., Rouméjon, S., Sandaruwan Ratnayake, A., Schrenk, M. O., Schwarzenbach, E. M., Twing, K. I., Weis, D., Whattam, S. A., Williams, M., and Zhao, R.: Expedition 357 summary, in: Proceedings of the International Ocean Discovery Program Volume 357, edited by: Früh-Green, G. L., Orcutt, B. N., Green, S. L., Cotterill, C., and the Expedition 357 Scientists, International Ocean Discovery Program Publications, College Station, TX, USA, https://doi.org/10.14379/iodp.proc.357.101.2017, 2017a.

Früh-Green, G. L., Orcutt, B. N., Green, S. L., Cotterill, C., Morgan, S., Akizawa, N., Bayrakci, G., Behrmann, J.-H., Boschi, C., Brazelton, W. J., Cannat, M., Dunkel, K. G., Escartin, J., Harris, M., Herrero-Bervera, E., Hesse, K., John, B. E., Lang, S. Q., Lilley, M. D., Liu, H.-Q., Mayhew, L. E., McCaig, A. M., Menez, B., Morono, Y., Quéméneur, M., Rouméjon, S., Sandaruwan Ratnayake, A., Schrenk, M. O., Schwarzenbach, E. M., Twing, K. I., Weis, D., Whattam, S. A., Williams, M., and Zhao, R.: Expedition 357 methods, in: Proceedings of the International Ocean Discovery Program, 357, edited by: Früh-Green, G. L., Orcutt, B. N., Green, S. L., Cotterill, C., and the Expedition 357 Scientists, International Ocean Discovery Program Publications, College Station, TX, USA, https://doi.org/10.14379/iodp.proc.357.102.2017, 2017b.

Früh-Green, G. L., Orcutt, B. N., Rouméjon, S., Lilley, M. D., Morono, Y., Cotterill, C., Green, S., Escartin, J., John, B. E., McCaig, A. M., Cannat, M., Ménez, B., Schwarzenbach, E. M., Williams, M. J., Morgan, S., Lang, S. Q., Schrenk, M. O., Brazelton, W. J., Akizawa, N., Boschi, C., Dunkel, K. G., Quéméneur, M., Whattam, S. A., Mayhew, L., Harris, M., Bayrakci, G., Behrmann, J.-H., Herrero-Bervera, E., Hesse, K., Liu, H.-Q., Ratnayake, A. S., Twing, K., Weis, D., Zhao, R., and Bilenker, L.: Magmatism, serpentinization and life: Insights through drilling the Atlantis Massif (IODP Expedition 357), Lithos, 323, 137–155, https://doi.org/10.1016/j.lithos.2018.09.012, 2018.

Hickok, K. A., Nguyen, T. B., and Lang, S. Q.: Assessment of apolar lipids in subseafloor rocks and potential contaminants from the Atlantis Massif (IODP Expedition 357), Org. Geochem., 122, 68–77, https://doi.org/10.1016/j.orggeochem.2018.05.003, 2018.

Kallmeyer, J.: Contamination Control for Scientific Drilling Operations, Adv. Appl. Microbiol., 98, 61–91, https://doi.org/10.1016/bs.aambs.2016.09.003, 2017.

Kallmeyer, J., Mangelsdorf, K., Cragg, B., and Horsfield, B.: Techniques for Contamination Assessment During Drilling for Terrestrial Subsurface Sediments, Geomicrobiol. J., 23, 227–239, https://doi.org/10.1080/01490450600724258, 2006.

Kelley, D. S., Karson, J. A., Früh-Green, G. L., Yoerger, D. R., Shank, T. M., Butterfield, D. A., Hayes, J. M., Schrenk, M. O., Olson, E. J., Proskurowski, G., Jakuba, M., Bradley, A., Larson, B., Ludwig, K., Glickson, D., Buckman, K., Bradley, A. S., Brazelton, W. J., Roe, K., Elend, M. J., Delacour, A., Bernasconi, S. M., Lilley, M. D., Baross, J. A., Summons, R. E., and Sylva, S. P.: A Serpentinite-Hosted Ecosystem: The Lost City Hydrothermal Field, Science, 307, 1428–1434, https://doi.org/10.1126/science.1102556, 2005.

Knights, D., Kuczynski, J., Charlson, E. S., Zaneveld, J., Mozer, M. C., Collman, R. G., Bushman, F. D., Knight, R., and Kelley, S. T.: Bayesian community-wide culture-

independent microbial source tracking, Nat. Methods, 8, 761–763, https://doi.org/10.1038/nmeth.1650, 2011.

Kozich, J. J., Westcott, S. L., Baxter, N. T., Highlander, S. K., and Schloss, P. D.: Development of a Dual-Index Sequencing Strategy and Curation Pipeline for Analyzing Amplicon Sequence Data on the MiSeq Illumina Sequencing Platform, Appl. Environ. Microbiol., 79, 5112–5120, https://doi.org/10.1128/AEM.01043-13, 2013.

Lang, S. Q. and Brazelton, W. J.: Habitability of the marine serpentinite subsurface: a case study of the Lost City hydrothermal field, Philos. T. R. Soc. A, 378, 20180429, https://doi.org/10.1098/rsta.2018.0429, 2020.

Lever, M. A., Alperin, M., Engelen, B., Inagaki, F., Nakagawa, S., Steinsbu, B. O., and Teske, A.: Trends in Basalt and Sediment Core Contamination During IODP Expedition 301, Geomicrobiol. J., 23, 517–530, https://doi.org/10.1080/01490450600897245, 2006.

Motamedi, S., Orcutt, B. N., Früh-Green, G. L., Twing, K. I., Pendleton, H. L., and Brazelton, W. J.: Microbial Residents of the Atlantis Massif's Shallow Serpentinite Subsurface, Appl. Environ. Microbiol., 86, e00356-20, https://doi.org/10.1128/AEM.00356-20, 2020.

Orcutt, B. N., Bergenthal, M., Freudenthal, T., Smith, D., Lilley, M. D., Schnieders, L., Green, S., and Früh-Green, G. L.: Contamination tracer testing with seabed drills: IODP Expedition 357, Sci. Dril., 23, 39–46, https://doi.org/10.5194/sd-23-39-2017, 2017.

Pauli, U., Liniger, M., and Zimmermann, A.: Detection of DNA in soybean oil, Z. Lebensm. Unters. Forsch., 207, 264–267, https://doi.org/10.1007/s002170050330, 1998.

Pruesse, E., Peplies, J., and Glöckner, F. O.: SINA: Accurate high-throughput multiple sequence alignment of ribosomal RNA genes, Bioinformatics, 28, 1823–1829, https://doi.org/10.1093/bioinformatics/bts252, 2012.

Rognes, T., Flouri, T., Nichols, B., Quince, C., and Mahé, F.: VSEARCH: a versatile open source tool for metagenomics, PeerJ, 4, e2584, https://doi.org/10.7717/peerj.2584, 2016.

Rohland, N. and Reich, D.: Cost-effective, high-throughput DNA sequencing libraries for multiplexed target capture, Genome Res., 22, 939–946, https://doi.org/10.1101/gr.128124.111, 2012.

Salter, S. J., Cox, M. J., Turek, E. M., Calus, S. T., Cookson, W. O., Moffatt, M. F., Turner, P., Parkhill, J., Loman, N. J., and Walker, A. W.: Reagent and laboratory contamination can critically impact sequence-based microbiome analyses, BMC Biol., 12, 87, https://doi.org/10.1186/s12915-014-0087-z, 2014.

Santelli, C. M., Banerjee, N., Bach, W., and Edwards, K. J.: Tapping the Subsurface Ocean Crust Biosphere: Low Biomass and Drilling-Related Contamination Calls for Improved Quality Controls, Geomicrobiol. J., 27, 158–169, https://doi.org/10.1080/01490450903456780, 2010.

Schloss, P. D., Westcott, S. L., Ryabin, T., Hall, J. R., Hartmann, M., Hollister, E. B., Lesniewski, R. A., Oakley, B. B., Parks, D. H., Robinson, C. J., Sahl, J. W., Stres, B., Thallinger, G. G., Horn, D. J. V., and Weber, C. F.: Introducing mothur: Open-Source, Platform-Independent, Community-Supported Software for Describing and Comparing Microbial Communities, Appl. Environ. Microbiol., 75, 7537–7541, https://doi.org/10.1128/AEM.01541-09, 2009.

Schloss, P. D., Gevers, D., and Westcott, S. L.: Reducing the Effects of PCR Amplification and Sequencing Artifacts on 16S rRNA-Based Studies, PLOS ONE, 6, e27310, https://doi.org/10.1371/journal.pone.0027310, 2011.

Sheik, C. S., Reese, B. K., Twing, K. I., Sylvan, J. B., Grim, S. L., Schrenk, M. O., Sogin, M. L., and Colwell, F. S.: Identification and Removal of Contaminant Sequences From Ribosomal Gene Databases: Lessons From the Census of Deep Life, Front. Microbiol., 9, 840, https://doi.org/10.3389/fmicb.2018.00840, 2018.

Smith, D. C., Spivack, A. J., Fisk, M. R., Haveman, S. A., Staudigel, H., and the Leg 185 Shipboard Scientific Party: Methods for quantifying potential microbial contamination during deep ocean coring, ODP Tech. Note, Ocean Drilling Program, 28, https://doi.org/10.2973/odp.tn.28.2000, 2000a.

Smith, D. C., Staudigel, H., Spivack, A. J., Fisk, M. R., and Haveman, S. A.: Tracer-Based Estimates of Drilling-Induced Microbial Contamination of Deep Sea Crust, Geomicrobiol. J., 17, 207–219, https://doi.org/10.1080/01490450050121170, 2000b.

Testolin, R. and Lain, O.: DNA Extraction from Olive Oil and PCR Amplification of Microsatellite Markers, J. Food Sci., 70, 108–112, https://doi.org/10.1111/j.1365-2621.2005.tb09011.x, 2005.

Wilkins, M. J., Daly, R., Mouser, P. J., Trexler, R., Wrighton, K. C., Sharma, S., Cole, D. R., Biddle, J. F., Denis, E., Fredrickson, J. K., Kieft, T. L., Onstott, T. C., Petersen, L., Pfiffner, S. M., Phelps, T. J., and Schrenk, M. O.: Trends and Future Challenges in Sampling the Deep Terrestrial Biosphere, Front. Microbiol., 5, 481, https://doi.org/10.3389/fmicb.2014.00481, 2014.

Yanagawa, K., Nunoura, T., McAllister, S., Hirai, M., Breuker, A., Brandt, L., House, C., Moyer, C. L., Birrien, J.-L., Aoike, K., Sunamura, M., Urabe, T., Mottl, M., and Takai, K.: The first microbiological contamination assessment by deep-sea drilling and coring by the D/V Chikyu at the Iheya North hydrothermal field in the Mid-Okinawa Trough (IODP Expedition 331), Front. Microbiol., 4, 327, https://doi.org/10.3389/fmicb.2013.00327, 2013.

Scientific Drilling
Open Access

Tools for pressure core sub-coring and pore-scale micro-CT (computed tomography) scans

Yongkoo Seol[1], Liang Lei[1,a], Karl Jarvis[1,2], Daniel Hill[1,3], Jeong-Hoon Choi[1,2], Taehyung Park[1], Xuerui Gai[1], Greg Wunderlich[4], Bill Grey[4], and Chris McArdle[4]

[1]National Energy Technology Laboratory, U.S. Department of Energy, Morgantown, West Virginia 26507, USA
[2]Leidos Research Support Team, Morgantown, West Virginia 26507, USA
[3]AMENTUN, Morgantown, West Virginia 26507, USA
[4]AMENTUM, Greenwood Village, Colorado 80111, USA
[a]now at: School of Engineering, Westlake University, Hangzhou, Zhejiang 310024, China

Correspondence: Liang Lei (leiliang@westlake.edu.cn)

Abstract. The pore habits of gas hydrate in natural sediment matrices provide essential clues for understanding physical (mechanical, thermal, hydraulic, and electrical) properties of hydrate-bearing sediments, yet there are no tools that can directly visualize the pore habits of natural gas hydrate other than indirect interpretation based on core-scale or field-scale observations. A significant challenge is to obtain a mini-core from pressure cores retrieved from natural reservoirs for high-resolution micro-CT (computed tomography) scans while maintaining pressure and temperature conditions required for stability of gas hydrate during all operational steps including manipulation, cutting, transferring, sub-coring and CT scanning. We present a new set of tools for pore-scale micro-CT imaging of natural hydrate-bearing sediments while maintaining pressure and temperature control. The tests with laboratory-prepared cores and pressure cores successfully demonstrate the capability of this set of tools to subsample a mini-core from pressure cores, transfer the mini-core to an X-ray transparent core holder, and conduct micro-CT scans. Successfully obtained CT images prove the functionality of this set of tools.

1 Introduction

Physical properties of deep marine gas hydrate-bearing sediments draw growing attention as they are a critical input for predicting energy extraction efficiency, seafloor settlement and wellbore stability. Due to high pressure in typical energy-enriched environments, gas bubbles as well as the dissolved gas in the fluid can expand drastically when depressurized. Gas hydrate in solid crystalline form can release gas with ~ 164 times the hydrate volume under standard conditions (Boswell and Collett, 2011). High pressure and low temperature are required to maintain the stability of gas hydrate (Makogon, 1997; Sloan and Koh, 2007). If the fluid pressure is not maintained during the coring process, the gas contained in the sediment pores, in the form of free gas, dissolved gas or solid gas hydrate, could expand drastically and potentially destroy the initial fabric of the sediments. Physi-

cal properties such as permeability and mechanical strength are directly affected by the sediment fabric. Maintaining the original sediment fabric, therefore, is of critical importance for the characterization of these sediments. Additionally, the study of hydrate-bearing sediments requires the preservation of hydrate and its pore habits in natural environments, which is of special interest because gas hydrate as a solid is a part of the sediment skeleton that affects both the mechanical and hydrological behaviors of the sediments (Boswell, 2009; Boswell and Collett, 2011).

A pressure-coring technique, which preserves the fluid pressure of the sample during the coring process (Amann et al., 1997; Dickens et al., 2003; Kvenvolden et al., 1983; Pettigrew, 1992; Qin et al., 2005; Dai et al., 2012; Schultheiss et al., 2009), is maturing rapidly with gas hydrate exploration activities in Japan, South Korea, India, China, and recently the US (Collett et al., 2019; Flemings et al., 2018; Ya-

mamoto, 2015; Yun et al., 2011; Zhang et al., 2014). The physical properties of pressure cores have been measured at core scale with specially developed tools (Fang et al., 2020; Priest et al., 2019; Santamarina et al., 2015; Yoneda et al., 2018; Yoneda et al., 2019; Yun et al., 2011), covering mechanical, thermal, hydraulic and electric properties. Interpretations of the results are largely based on idealized pore habits: grain coating, cementing and pore filling (Dai et al., 2012; Waite et al., 2009; Yun et al., 2007). Defining the real distribution and morphology of hydrate within the sediment matrix is critical for understanding the sediment physical properties and resulting interpretations. However, there are no tools that allow for direct visualization of pore-scale behaviors of natural hydrate-bearing sediments to date.

A micro-CT (computed tomography) technique utilizing phase contrast has been developed to obtain the pore-scale structure of laboratory-synthesized methane hydrate-bearing sediments (Lei et al., 2018), but the core size must be less than 10 mm in order to achieve high-resolution scans. The diameter of whole-round pressure core samples from currently available pressure core drilling tools is > 50 mm (Schultheiss et al., 2009). Therefore, a toolset is essential to enable the retrieval of a mini-core from a larger pressure core while maintaining the pressure and temperature of the hydrate-bearing sediments under in situ conditions during the whole process. Sub-coring tools have been developed for this specific purpose (Jin et al., 2014; Schultheiss et al., 2009; Parkes et al., 2009), but they have not been applied to pressure cores for pore-scale micro-CT scanning.

This work presents a set of tools that can subsample a mini-core from pressure cores and transfer it into an X-ray transparent core holder under in situ conditions. The mini-core is then scanned with a micro-CT scanner with a resolution of 2 μm. Mini-core sub-coring and transferring processes are presented together with basic operations on full-size pressure cores including grabbing, manipulation, and cutting. Details on CT scan configuration and the X-ray transparent core holder are covered in Lei et al. (2018) and Seol et al. (2019).

2 Concept of design and operation procedure

This section describes the concept design and operational sequence to achieve the desired functionality. The requirement is to drill a mini-core (9.5 mm in diameter) out of the original pressure core (50 mm in diameter) and transfer the mini-core into the attached micro-CT scanning assembly. Temperature is maintained inside an environmental chamber at $6 \pm 0.5\,°C$ where drilling and transfer of the mini-core occur. The fluid pressure is maintained by ISCO high-pressure syringe pumps at 24.1 MPa (3500 psi). The pressure rating of this system is 34.5 MPa (5000 psi). Due to the pressures required for such a process, this set of tools is designed to ASME B31.3 and ASME BVPC Section VIII, Div 1, where required. The mini-

core together with its hosting micro-CT scanning assembly is then covered in thermal insulation and relocated to the micro-CT scanner for 3D pore-scale scanning. Figure 1 shows the key components that enable this capability: (a, b) the manipulator and cutter used for general pressure core manipulation, temporary storage and cutting; (c, d) the sub-coring tool to drill a mini-core; and (e, f) the sub-coring chamber where the mini-core drilling occurs and the attached micro-CT scanning assembly to receive and scan the mini-core with X-ray CT. The functions of each component will be described in the following sections.

2.1 General operations for pressure cores

The pressure core is retrieved from the Gulf of Mexico during the University of Texas (UT) Hydrate Pressure Coring Expedition 1 (UT-GOM2-1), at the well in Green Canyon Block 955 (GC 955). The core is from the hydrate reservoir between 425 and 428 m below the sea floor, and the reservoir is composed of fine sands interbedded with clays according to the LWD log characterization (Fang et al., 2020; Boswell et al., 2012).

Pressure cores are initially held under pressure in specially designed transport chambers. A series of operations are required to manipulate and cut the pressure core into proper lengths before they get transferred into various function modules, such as a cutter or a CT scanning chamber, for specialized characterization. There is literature available (Santamarina et al., 2012; Schultheiss et al., 2009) describing the general concept of pressure core manipulation. Figure 2 shows the cross-section view of a typical pressure core transfer process: (a) pressurize the temporary storage chamber and the space between two ball valves with deionized water to the same pressure as that in the transportation chamber; (b) open the two ball valves and use the grabber to grab the core sleeve in the function module (transportation chamber as an example here); note that the friction between the pressure core and the sleeve binds them together; (c) transfer the pressure core to the temporary storage chamber by retrieving the grabber and close the left ball valve. The key component of pressure core handling is the manipulator module (Fig. 1a and b). It consists of a manipulator that pushes or pulls pressure cores inside core sleeves with a sleeve grabber, a temporary storage chamber, and a ball valve (components A, B and C in Fig. 2). Two viewports are installed on the temporary storage chamber to visually check the position and quality of the pressure core. The pressure core is retrieved from a function module with the procedure displayed in Fig. 2. A similar approach is used to insert the pressure core into other function modules. Note that the function module could be a cutter (Fig. 1a), storage chamber, sub-coring chamber (Fig. 1e and f), or any other stand-alone modules built for specific purposes.
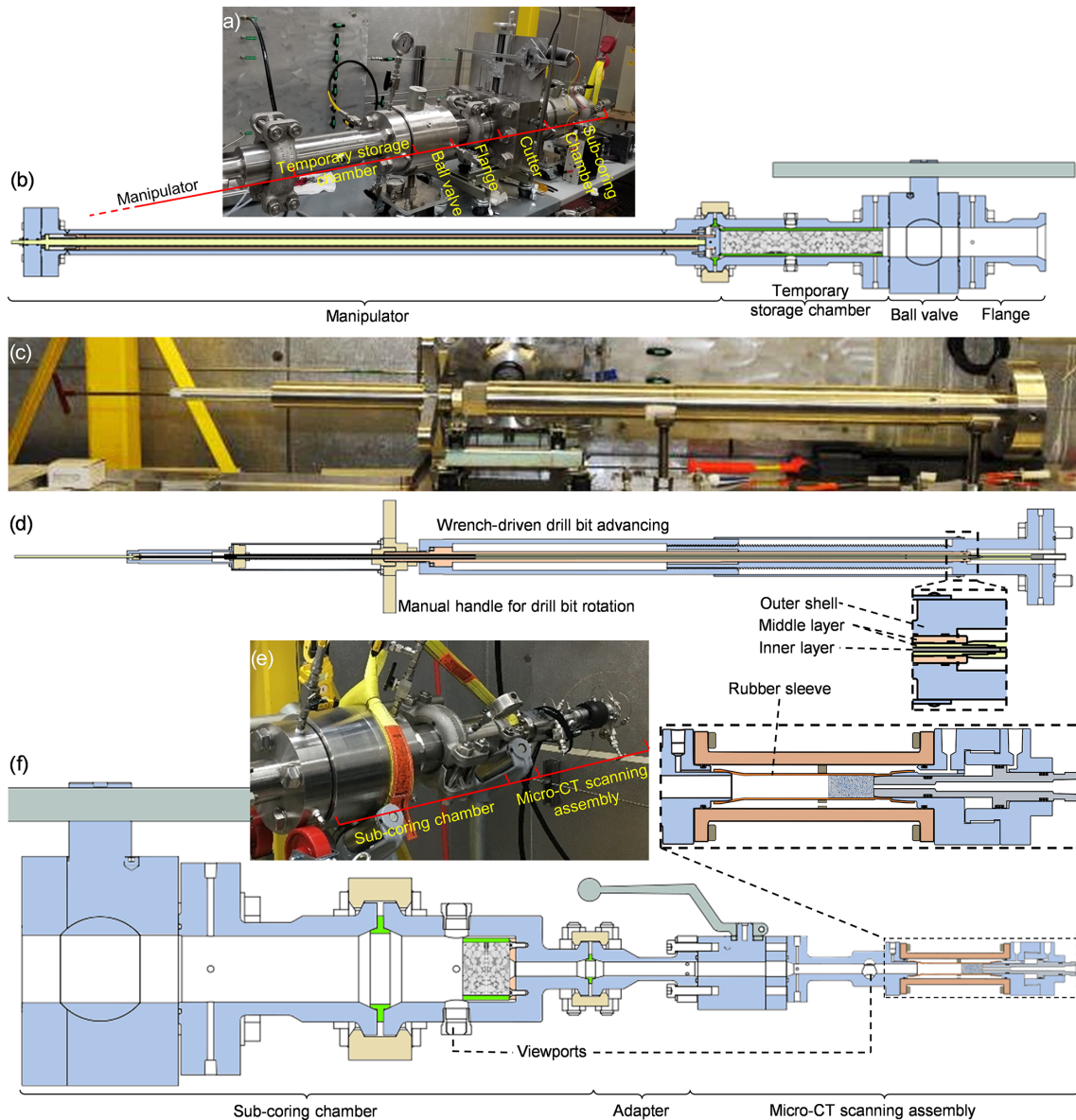
Figure 1. Pressure core Characterization and X-ray visualization Tool (PCXT) components. **(a)** Manipulator module and automated cutter, **(b)** section view of the manipulator module, **(c)** sub-coring tool, **(d)** section view of the sub-coring tool, **(e)** sub-coring chamber and micro-CT scanning assembly that includes a small ball valve, core holder adapter and beryllium core holder, and **(f)** section view of the sub-coring chamber and micro-CT scanning assembly.

2.2 Pre-operations before sub-coring

Core-scale CT scans that provide the overview of the whole core could help verify the status and quality of the pressure core before any further operation, since the pressure core degrades during transportation and long-term storage, due to the lack of effective stress-caused core expansion and hydrate dissolution into surrounding water (Dai and Santamarina, 2014; Jang et al., 2019a). A pressure core initially stored in a transportation chamber is transferred into the CT scanning chamber for the core-scale overview scan first. After the core-scale CT scan, the pressure core is transferred from

the CT scan chamber into the manipulator. Then the pressure core is pushed into the automated cutter, placed at a predetermined location, cut into appropriate lengths, and pushed further into the position for the sub-coring process (Fig. 3). The residual pressure core is pulled back to the temporary storage chamber for other purposes.

2.3 Sub-coring and mini-core transfer

Once the sub-coring chamber is detached from the cutting assembly and attached to the sub-coring tool, the cut pressure
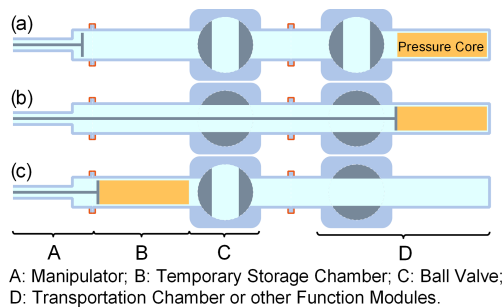
A: Manipulator; B: Temporary Storage Chamber; C: Ball Valve;
D: Transportation Chamber or other Function Modules.

Figure 2. General operations for pressure core manipulation (modified from Santamarina et al., 2012). The manipulator module includes manipulator, temporary storage chamber and ball valve.
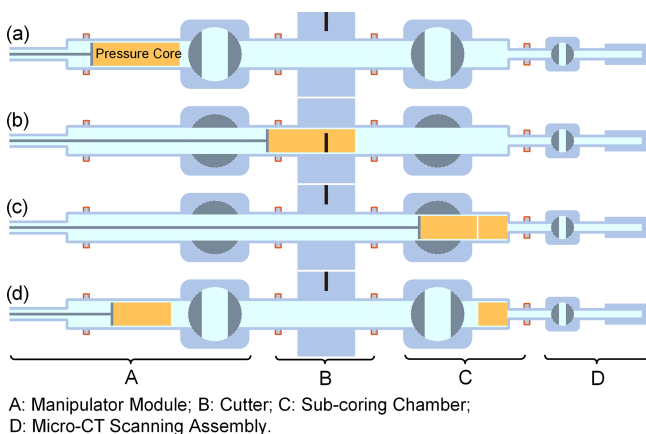

A: Manipulator Module; B: Cutter; C: Sub-coring Chamber;
D: Micro-CT Scanning Assembly.

Figure 3. Pressure cores being cut to appropriate lengths and transferred into the sub-coring chamber. **(a)** Equilibrate the pressure in all the components; **(b)** push the pressure core to the predetermined position and cut it; **(c)** push the pressure core to the sub-coring chamber; **(d)** retrieve the remaining pressure core into the temporary storage chamber.

core inside the sub-coring chamber is ready for sub-coring (Fig. 4a). The sub-coring tool consists of three main layers: the outer shell that holds the pressure, the middle layer and connected drill bit to drill a mini-core from the pressure core, and the inner layer that pushes the drilled mini-core into the micro-CT scanning assembly. The standard drill bit is designed to cut hard cores and made of 316 stainless steel, with an ID of 9.35 mm (0.368 in), OD of 12.7 mm (0.5 in) and depth of 163.8 mm (6.45 in). The OD of the drill bit tip (63.5 mm or 2.5 in, longer than the expected mini-core) can reduce to eliminate sample disturbance in softer cores, e.g., 10.57 mm (0.416 in) when pushing through hydrate-bearing pressure cores. Note that the advancing and rotating of the drill bit are independent in this design, driven by specially designed wrenches and manually operated handles (Fig. 1c and d).

The drill bit is first pushed against the core without being rotated, which can also be observed from the viewport on the sides (Fig. 1f). The viewports (Encole LLC, NPT 3/4) are
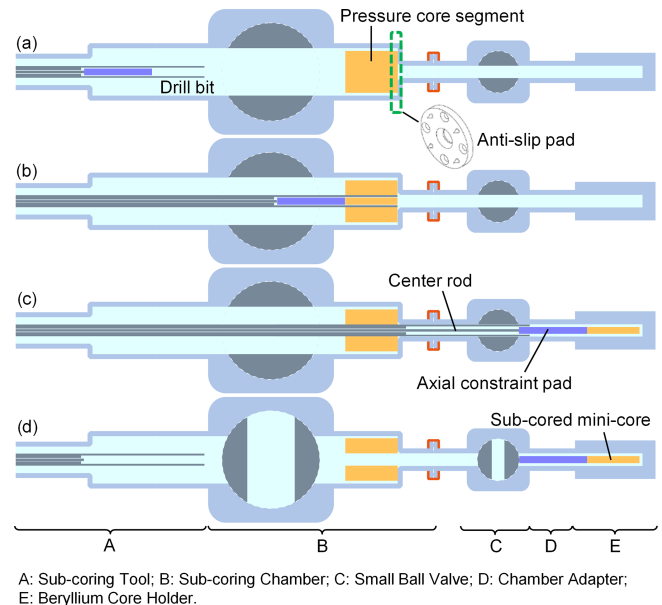

A: Sub-coring Tool; B: Sub-coring Chamber; C: Small Ball Valve; D: Chamber Adapter;
E: Beryllium Core Holder.

Figure 4. Sub-coring of cut pressure core and mini-core transfer into micro-CT scanning assembly that includes small ball valve, chamber adapter, and beryllium core holder. **(a)** Assemble the sub-coring components and attach them to the chamber that contains the cut pressure core; **(b)** open the ball valve and advance and drill through the pressure core; **(c)** advance the drill bit now containing the mini-core to pass the small ball valve and use the center rod in the inner layer to push the mini-core out of the drill bit towards the end of the beryllium core holder; **(d)** retract the drill back to its original position. Note the anti-slip pad and its location in the sub-coring chamber (green frame in panel **a**).

rated up to 6170 psi with the diameter of window 14.0 mm (0.55 in). There is an anti-slip pad with teeth of sharpened screws in a radial pattern outside the center sampling area penetrating the pressure core and resisting the rotation of the core while drilling. To subsample the pressure core, the rotating and pushing of the drill bit occur simultaneously with different combinations according to the properties of the core. For a hard core such as sandstone, a higher rotation-to-advance ratio is recommended. For soft sediments, the drill bit can be punched through the sediment without rotation. After the drill bit cuts through the core (Fig. 4b), the drill bit continues to advance through the small ball valve with the mini-core in it. Then the center rod pushes the axial constraint pad against the mini-core to send the mini-core to the beryllium core holder (Fig. 4c). The axial constraint pad is left inside the micro-CT scanning assembly to provide axial support for the mini-core during hydrological–mechanical testing, and its length is pre-determined according to the length of the obtained mini-core. Both the center rod and the drill bit are retracted from the small ball valve so that the small ball valve can be closed to secure the pressure inside the micro-CT scanning assembly (Fig. 4d). The pressure in
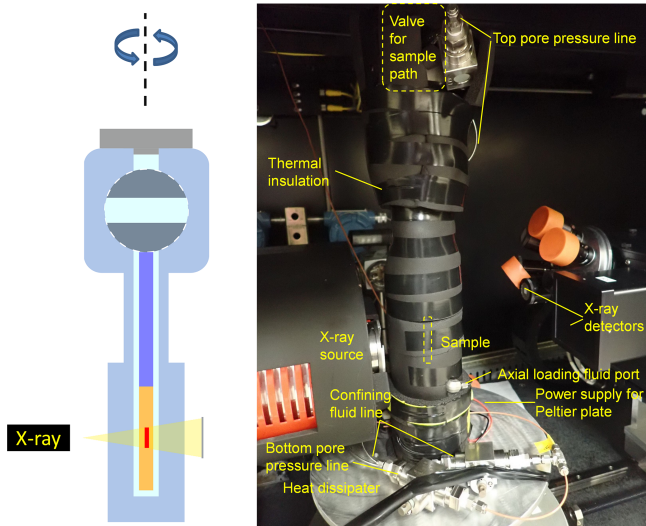
Figure 5. Micro-CT scan of a mini-core under pressure and temperature control.

Figure 6. Mini-cores drilled under pressure with this set of tools. **(a)** Two mini-cores at the top show the capability of this tool to drill through hard sandstones. **(b)** Mini-core sampled by drilling through a segment of the pressure core.

the sub-coring chamber can be released to dissociate hydrate in the residual pressure core after sub-coring.

The micro-CT scanning assembly is designed to conduct triaxial testing; therefore, the axial support of the mini-core against the pushing pad is critical. Note that the other end of the pushing pad is against the ball of the small ball valve. Therefore, the main body and tail of the pushing pad are made of aluminum and a thin layer of Teflon (1/16 in or 1.6 mm) to increase the stiffness of the pushing pad and prevent scratching of the ball valve surface.

2.4 Micro-CT scan of mini-cores

The micro-CT scanning assembly containing the mini-core is detached from the sub-coring tool (Fig. 5a) before it is transferred and mounted on the rotary stage in the micro-CT scanner (Fig. 5b). Temperature and pressure controls are required to maintain the stability of gas hydrate in the mini-core. A Peltier plate is used to control the temperature during CT scanning by transferring heat from the micro-CT scanning chamber and dissipating the heat into the environment. The plate should be turned on at least 1 h before the mini-core transfer so that the rotary stage is pre-chilled to reduce temperature disturbance to the mini-core. One ISCO high-pressure syringe pump is connected to both the top pore pressure line and confining fluid line to maintain the fluid pressure. Such a configuration does not apply any effective stress on the core. Micro-CT scans are conducted to obtain 3D structures of the mini-core. Note that the pressure line and power cables for the Peltier plate are all flexible to allow the rotation of the micro-CT scanning assembly during CT scans.

Detailed CT scan configuration and image processing are covered in Lei et al. (2018). Previous results of hydrate
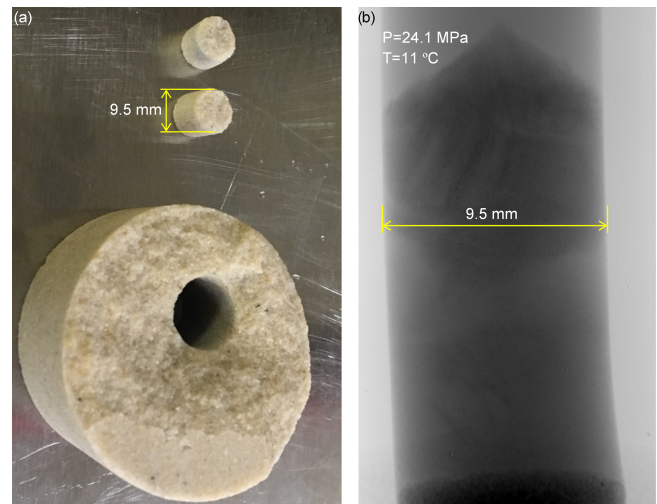
formation, dissociation and mechanical testing on hydrate-bearing sediments with laboratory-synthesized cores can be found in Lei and Seol (2020) and Lei et al. (2019a, b).

3 Results

3.1 Sub-coring under pressure

Sub-coring was successful on both hard sandstone and soft hydrate-bearing sediments under targeted pressure and temperature conditions (Fig. 6), which demonstrates the capability of this set of tools. When drilling through a hard sandstone core, the mini-core broke into two segments during drilling due to shear-induced cracks (Fig. 6a), but this would not affect the micro-CT scanning as a piece of intact sample larger than 3 mm^3 is sufficient for a pore-scale micro-CT scan. As for natural hydrate-bearing sediments, the original pressure core degraded during the long-term ($\sim$ 2 years) storage and recent manipulations before the sub-coring. Therefore, the drill bit was pushed through the pressure core without any rotation, and the obtained mini-core did not have a perfect column shape (Fig. 6b), but there are intact blocks of hydrate-bearing sediments in this mini-core, which is large enough to capture the stratigraphic features in the radiographic image, proving its sub-coring capability.

3.2 Pore-scale imaging of hydrate-bearing sediments

Figure 7 shows 3D high-resolution micro-CT images of a mini-core from natural gas hydrate-bearing sediments. Three different phases including sediment particles, pore fluid and natural gas hydrate can be identified at pore scale. The voxel size is 2.3 µm, and sediment particle sizes range from 20 to
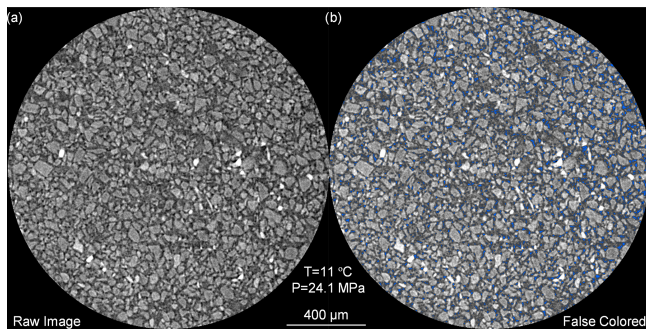
Figure 7. One slice of the 3D image obtained from the micro-CT scan of subsampled natural hydrate-bearing sediments: **(a)** raw image and **(b)** false-colored image (hydrate in blue; note that the noise in the raw image is preserved).

50 μm. Note that the pore fluid contains some sodium iodide (NaI) salt. The fluid in the core space of the micro-CT scanning chamber contained 7 wt % of KI initially before the core holder received the mini-core, and this salt concentration is higher than the 5 wt % in our previous publication (Lei et al., 2018). This 7 wt % of salt concentration was selected considering fluid mixing with the original pore fluid in the sediment and fluid exchange with the sub-coring chamber filled with deionized water so that the salt concentration of the pore fluid decreases when the system reaches equilibrium. According to the attenuation coefficient analysis based on the effective X-ray spectrum, the brightness of sediment particles, pore fluid and gas hydrate decreases in that order; therefore, the darkest spot in the raw CT image is gas hydrate.

4 Discussion

4.1 Sample disturbance

Sample disturbance is present in any sampling technique, as the sampling process is inherently associated with different sources of disturbance, including change in effective stress and pore fluid pressure, sample transportation and storage, sample manipulation before testing and so forth (Baligh et al., 1987; Rochelle et al., 1981; Sheng and Carlos, 2014). In the two sub-coring practices with this toolset, there is clear evidence of sample disturbance. When the hard sandstone is used, the drilled mini-core breaks into two segments, as shown in Fig. 6a. This is very likely due to the friction between the drill bit and the mini-core, and the mini-core breaks when the drilling torque exceeds the lateral shear strength of the mini-core. Similar phenomena are often seen in pressure cores (Dai and Santamarina, 2014; Jang et al., 2019b; Fang et al., 2020). Meanwhile, the four teeth on the anti-slip pad damage the surface of the sandstone, but the damage occurs on the outer residual portion of the sample and therefore does not affect the quality of the mini-core taken from the center. As for the soft sediments, the four teeth

can easily penetrate the core but do not affect the mini-core quality. When the drill bit is punched through the pressure core, we risk both compression against the core and shear at the side of the mini-core, which is challenging to analyze. Sample disturbance is unavoidable during the coring process. However, for the purpose of visualization of pore-scale hydrate distribution, a small piece of the well-preserved core as seen in both mini-cores in Fig. 6 is sufficient, proving the toolset successfully serves its designated purpose.

4.2 Toolset features

This set of tools has several features that facilitate the pore-scale micro-CT scanning.

1. Small mini-core diameter (9.5 mm). This core diameter enables high-resolution micro-CT scanning with a resolution of 2 μm, therefore allowing for natural gas hydrate identification in pore sizes of 20 μm.

2. Applicable on a wide range of cores. As demonstrated, this tool can subsample mini-cores from both hard and soft cores.

3. Simple and robust core transfer mechanism. The drilling and pushing of the mini-core with this set of tools are along a straight line and only involve the drill bit advancing to deliver the mini-core to the micro-CT scanning assembly.

4. Manual handles in the drilling process. Manual controls on drill rotation and advancement during the sub-coring process allow operators to get a direct sense of stress and resistance, thus reducing the likelihood of damage/breakage of the mini-core and original pressure core.

5. Anti-slip pad during sub-coring. The teeth sticking into the pressure core during the drilling process can fix the position of the original pressure core while the drill bit rotates. This approach utilizes the compression between the drill bit and the core and therefore requires no additional pressure core-grabbing mechanism.

6. No additional cutting on the mini-core is required after the drilling process when compared with the tools reported in Parkes et al. (2009).

7. Drilling through the center of the pressure core. An alternative strategy is to drill through the side of the pressure core, which involves drilling through the plastic core sleeve outside the pressure core. There would be a piece of plastic at the end of the mini-core, which prevents axial permeability measurements. Furthermore, to conduct a permeability test, the alternative strategy needs a mechanism to remove the plastic liner from the mini-core end.

8. Precise control of the mini-core position after core transfer. All the other existing techniques simply push the mini-core into the next testing chamber (Jin et al., 2014; Parkes et al., 2009; Schultheiss et al., 2009), therefore not having control of the mini-core position. The procedure in this study pushes the mini-core into the rubber sleeve which is at the center of the micro-CT scanning assembly.

9. Permeability and mechanical testing of the mini-core are achievable. The micro-CT scanning assembly has a rubber sleeve (Fig. 1f) separating the mini-core and confining fluid to enable the application of lateral confining pressure and a functional end piece that can hydraulically drive a piston to apply axial pressure. Influent and effluent ports allow for flowing fluid through the mini-core (further details in Seol et al., 2019). This permits hydrological and mechanical testing of the mini-core, although these tests were not conducted in this study due to the quality of the degraded pressure core.

4.3   Potential applications

Direct application. Gas hydrate in nature contains a large amount of natural gas (Boswell and Collett, 2011; Milkov, 2004). Therefore, if commercial gas production is achieved, gas hydrate has the potential to expand the worldwide energy supply. Pore habits within single pores and inter-pore distribution of gas hydrate in sediments reflect formation histories (Lei et al., 2019a); therefore, they can vary in different reservoirs. Major energy consumers and importers such as the US, China, Japan and India are investing extensively in hydrate pressure core research, targeting commercial gas production. This set of tools provides pore-scale insight into the reservoir, which helps us to understand the behavior of hydrate during formation, evolution and production. Physical properties such as permeability, thermal conductivity, mechanical stiffness and strength are highly dependent on the pore habits and distribution of gas hydrate in the sediment matrix. These properties are key input parameters to predict gas production rates and evaluate the cost–benefit ratio through reservoir simulations. Therefore, this sub-coring process and the subsequent micro-CT studies it enables are needed prior to pursuing direct field tests for gas production, especially when offshore operations are involved. Such pore-scale 3D studies help to reveal the interactive nature of hydrate crystals with sediment matrices and their mechanical integrity as well as to acquire reliable quantitative prediction of reservoir productivity.

The tools, used together with the micro-CT scanner, enable monitoring of the multiphase fluid's behaviors in a porous medium as the physicochemical substances change in a chamber. Direct observations of dynamic flow patterns of immiscible fluids, such as oil and brine or CO_2 with brine, are attainable through micro-CT analysis in responses to ad-

sorption, complexation, and dissolution reactions of the components. Those observations can also be applicable to conventional energy-related fields such as oil recovery, geologic carbon storage and diverse environmental remedial technologies.

Indirect applications. Any applications that require sub-coring processes within an isolated environment could use the procedure described here. Since the chamber used in this application could be a barrier for pressure, heat, electrical current or any other physical, chemical or biological changes, the procedure described herein could be used with minor modifications.

5   Conclusions

This work presents a series of tools that enable the manipulation, transfer, cutting, sub-coring and CT scanning at both core and pore scale of pressure cores while maintaining pressure and temperature controls. The mini-cores created demonstrate that the sub-coring tool can drill through both hard and soft sediments under pressure and provide adequate samples with intact segments. This set of tools along with the testing procedure allows for the investigation of pore habits of natural gas hydrate within the sediment matrix. Furthermore, this set of tools can be used for other potential operations that require environmental controls throughout all steps of operation.

References

Amann, H., Hohnberg, H.-J., and Reinelt, R.: HYACE – A novel autoclave coring equipment for systematic offshore gas hydrate sampling, Gas Hydrates: Problems Substance/Resource, Clausthal-Zellerfeld (Harz), Germany, 1997.

Baligh, M. M., Azzouz, A. S., and Chin, C. T.: Disturbances Due to "Ideal" Tube Sampling, J. Geotech. Eng., 113, 739–757, https://doi.org/10.1061/(ASCE)0733-9410(1987)113:7(739), 1987.

Boswell, R.: Is gas hydrate energy within reach?, Science, 325, 957–958, https://doi.org/10.1126/science.1175074, 2009.

Boswell, R. and Collett, T. S.: Current perspectives on gas hydrate resources, Energy Environ. Sci., 4, 1206–1215, https://doi.org/10.1039/C0EE00203H, 2011.

Boswell, R., Frye, M., Shelander, D., Shedd, W., McConnell, D. R., and Cook, A.: Architecture of gas-hydrate-bearing sands from Walker Ridge 313, Green Canyon 955, and Alaminos Canyon 21: Northern deepwater Gulf of Mexico, Mar. Pet. Geol., 34, 134–149, https://doi.org/10.1016/j.marpetgeo.2011.08.010, 2012.

Collett, T. S., Kumar, P., Boswell, R., and Waite, W. F.: Preface: Marine gas hydrate reservoir systems along the Eastern Continental Margin of India: Results of the National Gas Hydrate Program Expedition 02, Mar. Pet. Geol., 108, 1–2, https://doi.org/10.1016/j.marpetgeo.2019.03.005, 2019.

Dai, S. and Santamarina, J. C.: Sampling disturbance in hydrate-bearing sediment pressure cores: NGHP-01 expedition, Krishna–Godavari Basin example, Mar. Pet. Geol., 58, 178–186, https://doi.org/10.1016/j.marpetgeo.2014.07.013, 2014.

Dai, S., Santamarina, J. C., Waite, W. F., and Kneafsey, T. J.: Hydrate morphology: Physical properties of sands with patchy hydrate saturation, J. Geophys. Res.-Sol. Ea., 117, B11205, https://doi.org/10.1029/2012JB009667, 2012.

Dickens, G. R., Schroeder, D. K., Hinrichs, U., and the Leg 201 Scientific Party: The pressure core sampler (PCS) on ODP Leg201: General operations and gas release, in: Proc.ODP, Init. Repts., College Station, TX (Ocean Drilling Program), edited by: D'Hondt, S. L., Jøgensen, B. B., Miller, D. J., et al., 201, 1–22, https://doi.org/10.2973/odp.proc.ir.201.103.2003, 2003.

Fang, Y., Flemings, P. B., Daigle, H., Phillips, S. C., Meazell, P. K., and You, K.: Petrophysical properties of the GC 955 hydrate reservoir inferred from reconstituted sediments: Implications for hydrate formation and production, AAPG Bull., 104, 1997–2028, https://doi.org/10.1306/01062019165, 2020.

Flemings, P. B., Phillips, S. C., Collett, T., Cook, A., Boswell, R., and the UT-GOM2-1 Expedition Scientists: UT-GOM2-1 Hydrate Pressure Coring Expedition Summary, University of Texas Institute for Geophysics, Austin, TX, USA, 2018.

Jang, J., Waite, W. F., Stern, L. A., Collett, T. S., and Kumar, P.: Physical property characteristics of gas hydrate-bearing reservoir and associated seal sediments collected during NGHP-02 in the Krishna-Godavari Basin, in the offshore of India, Mar. Pet. Geol., 108, 249–271, https://doi.org/10.1016/j.marpetgeo.2018.09.027, 2019a.

Jang, J., Dai, S., Yoneda, J., Waite, W. F., Stern, L. A., Boze, L.-G., Collett, T. S., and Kumar, P.: Pressure core analysis of geomechanical and fluid flow properties of seals associated with gas hydrate-bearing reservoirs in the Krishna-Godavari Basin, offshore India, Mar. Pet. Geol., 108, 537–550, https://doi.org/10.1016/j.marpetgeo.2018.08.015, 2019b.

Jin, Y., Konno, Y., and Nagao, J.: Pressurized subsampling system for pressured gas-hydrate-bearing sediment: Microscale imaging using X-ray computed tomography, Rev. Sci. Instrum., 85, 094502, https://doi.org/10.1063/1.4896354, 2014.

Kvenvolden, K. A., Barnard, L. A., and Cameron, D. H.: Pressure core barrel: Application to the study of gas hydrates, Deep Sea Drilling Project Site 533, Leg 76, Washington, D.C., USA, 367–375, 1983.

Lei, L. and Seol, Y.: Pore-scale investigation of methane hydrate-bearing sediments under triaxial condition, Geophys. Res. Lett., 47, e2019GL086448, https://doi.org/10.1029/2019GL086448, 2020.

Lei, L., Seol, Y., and Jarvis, K.: Pore-scale visualization of methane hydrate-bearing sediments with micro-CT, Geophys. Res. Lett., 45, 5417–5426, https://doi.org/10.1029/2018GL078507, 2018.

Lei, L., Seol, Y., Choi, J.-H., and Kneafsey, T. J.: Pore habit of methane hydrate and its evolution in sediment matrix – Laboratory visualization with phase-contrast micro-CT, Mar. Pet. Geol., 104, 451–467, https://doi.org/10.1016/j.marpetgeo.2019.04.004, 2019a.

Lei, L., Seol, Y., and Myshakin, E. M.: Methane hydrate film thickening in porous media, Geophys. Res. Lett., 46, 11091–11099, https://doi.org/10.1029/2019GL084450, 2019b.

Makogon, Y. F.: Hydrates of hydrocarbons, Pennwell Books, PennWell Publishing Company, Tulsa, Oklahoma, USA, 1997.

Milkov, A. V.: Global estimates of hydrate-bound gas in marine sediments: how much is really out there?, Earth-Sci. Rev., 66, 183–197, https://doi.org/10.1016/j.earscirev.2003.11.002, 2004.

Parkes, R. J., Sellek, G., Webster, G., Martin, D., Anders, E., Weightman, A. J., and Sass, H.: Culturable prokaryotic diversity of deep, gas hydrate sediments: first use of a continuous high-pressure, anaerobic, enrichment and isolation system for subseafloor sediments (DeepIsoBUG), Environ. Microbiol., 11, 3140–3153, https://doi.org/10.1111/j.1462-2920.2009.02018.x, 2009.

Pettigrew, T. L.: Design and operation of a wireline Presure Core Sampler (PCS), Texas A&M University, College Station, Texas, USA, 1992.

Priest, J. A., Hayley, J. L., Smith, W. E., Schultheiss, P., and Roberts, J.: PCATS triaxial testing: Geomechanical properties of sediments from pressure cores recovered from the Bay of Bengal during expedition NGHP-02, Mar. Pet. Geol., 108, 424–438, https://doi.org/10.1016/j.marpetgeo.2018.07.005, 2019.

Qin, H., Gu, L., Li, S., Zhu, L., and Chen, Y.: Pressure tight piston corer – A new approach on gas hydrate investigation, China Ocean Eng., 19, 121–128, https://doi.org/10.3321/j.issn:0890-5487.2005.01.011, 2005.

Rochelle, P. L., Sarrailh, J., Tavenas, F., Roy, M., and Leroueil, S.: Causes of sampling disturbance and design of a new sampler for sensitive soils, Can. Geotech. J., 18, 52–66, https://doi.org/10.1139/t81-006, 1981.

Santamarina, J. C., Dai, S., Jang, J., and Terzariol, M.: Pressure Core Characterization Tools for Hydrate-Bearing Sediments, Sci. Dril., 14, 44–48, https://doi.org/10.2204/iodp.sd.14.06.2012, 2012.

Santamarina, J. C., Dai, S., Terzariol, M., Jang, J., Waite, W. F., Winters, W. J., Nagao, J., Yoneda, J., Konno, Y., Fujii, T., and Suzuki, K.: Hydro-bio-geomechanical properties of hydrate-bearing sediments from Nankai Trough, Mar. Pet. Geol., 66, 434–450, https://doi.org/10.1016/j.marpetgeo.2015.02.033, 2015.

Schultheiss, P., Holland, M., and Humphrey, G.: Wireline Coring and Analysis under Pressure: Recent Use and Future Developments of the HYACINTH System, Sci. Dril., 7, 44–50, https://doi.org/10.2204/iodp.sd.7.07.2009, 2009.

Seol, Y., Lei, L., Choi, J.-H., Jarvis, K., and Hill, D.: Integration of triaxial testing and pore-scale visualization of methane hydrate bearing sediments, Rev. Sci. Instrum., 90, 124504, https://doi.org/10.1063/1.5125445, 2019.

Sheng, D. J. and Carlos, S.: Sampling disturbance in hydrate-bearing sediment pressure cores: NGHP-01 expedition, Krishna–Godavari Basin example, Mar. Pet. Geol., 58, 178–186, https://doi.org/10.1016/j.marpetgeo.2014.07.013, 2014.

Sloan, E. D. and Koh, C. A.: Clathrate hydrates of natural gases (Third edition), edited by: Speight, J. G., CRC Press, Boca Raton, FL, USA, 752 pp., 2007.

Waite, W. F., Santamarina, J. C., Cortes, D. D., Dugan, B., Espinoza, D. N., Germaine, J., Jang, J., Jung, J. W., Kneafsey, T. J., Shin, H., Soga, K., Winters, W. J., and Yun, T. S.: Physical properties of hydrate-bearing sediments, Rev. Geophys., 47, RG4003, https://doi.org/10.1029/2008RG000279, 2009.

Yamamoto, K.: Overview and introduction: Pressure core-sampling and analyses in the 2012–2013 MH21 offshore test of gas production from methane hydrates in the eastern Nankai Trough, Mar. Pet. Geol., 66, 296–309, https://doi.org/10.1016/j.marpetgeo.2015.02.024, 2015.

Yoneda, J., Oshima, M., Kida, M., Kato, A., Konno, Y., Jin, Y., Jang, J., Waite, W. F., Kumar, P., and Tenma, N.: Pressure core based onshore laboratory analysis on mechanical properties of hydrate-bearing sediments recovered during India's National Gas Hydrate Program Expedition (NGHP) 02, Mar. Pet. Geol., 108, 482–501, https://doi.org/10.1016/j.marpetgeo.2018.09.005, 2018.

Yoneda, J., Oshima, M., Kida, M., Kato, A., Konno, Y., Jin, Y., Jang, J., Waite, W. F., Kumar, P., and Tenma, N.: Permeability variation and anisotropy of gas hydrate-bearing pressure-core sediments recovered from the Krishna–Godavari Basin, offshore India, Mar. Pet. Geol., 108, 524–536, https://doi.org/10.1016/j.marpetgeo.2018.07.006, 2019.

Yun, T. S., Santamarina, J. C., and Ruppel, C.: Mechanical properties of sand, silt, and clay containing tetrahydrofuran hydrate, J. Geophys. Res.-Sol. Ea., 112, B04106, https://doi.org/10.1029/2006JB004484, 2007.

Yun, T. S., Lee, C., Lee, J.-S., Bahk, J. J., and Santamarina, J. C.: A pressure core based characterization of hydrate-bearing sediments in the Ulleung Basin, Sea of Japan (East Sea), J. Geophys. Res.-Sol. Ea., 116, B02204, https://doi.org/10.1029/2010JB007468, 2011.

Zhang, G., Yang, S., Zhang, M., Liang, J., Lu, J., Holland, M., and Schultheiss, P.: GMGS2 expedition investigates rich and complex gas hydrate environment in the South China Sea, Fire in the Ice, 14, 1–5, 2014.

Scientific Drilling
Open Access

Workshop report: Exploring deep oceanic crust off Hawai‘i

Susumu Umino[1], Gregory F. Moore[2], Brian Boston[3], Rosalind Coggon[4], Laura Crispini[5],
Steven D'Hondt[6], Michael O. Garcia[2], Takeshi Hanyu[7], Frieder Klein[8], Nobukazu Seama[9],
Damon A. H. Teagle[4], Masako Tominaga[10], Mikiya Yamashita[7,11], Michelle Harris[12], Benoit Ildefonse[13],
Ikuo Katayama[14], Yuki Kusano[15], Yohey Suzuki[16], Elizabeth Trembath-Reichert[17], Yasuhiro Yamada[18],
Natsue Abe[18], Nan Xiao[18], and Fumio Inagaki[18]

[1]School of Geosciences and Civil Engineering, College of Science and Engineering,
Kanazawa University, Kanazawa 920-1192, Japan
[2]Department of Earth Sciences, University of Hawai‘i at Mānoa, Honolulu, HI 96822, USA
[3]Lamont-Doherty Earth Observatory, Columbia University, Palisades, NY 10964, USA
[4]School of Ocean and Earth Science, National Oceanography Centre Southampton,
University of Southampton, Southampton SO14 3ZH, UK
[5]Department of Earth, Environment and Life Sciences, University of Genoa, 16126 Genoa, Italy
[6]Graduate School of Oceanography, University of Rhode Island, Narragansett, RI 02882, USA
[7]Research Institute for Marine Geodynamics, Japan Agency for Marine-Earth Science and Technology
(JAMSTEC), Yokosuka 237-0061, Japan
[8]Department of Marine Chemistry and Geochemistry, Woods Hole Oceanographic Institution,
Woods Hole, MA 02543, USA
[9]Department of Planetology, Graduate School of Science, Kobe Ocean-Bottom Exploration Center (KOBEC),
Kobe University, Kobe 657-8501, Japan
[10]Department of Geology and Geophysics, Woods Hole Oceanographic Institution,
Woods Hole, MA 02543, USA
[11]Institute of Geology and Geoinformation, National Institute of Advanced Industrial Science and
Technology (AIST), Tsukuba 305-8567, Japan
[12]School of Geography, Earth and Environmental Sciences, University of Plymouth, Plymouth PL4 8AA, UK
[13]Geosciences Montpellier, University of Montpellier, CNRS, Montpellier, France
[14]Department of Earth and Planetary System Sciences, Hiroshima University,
Higashi-Hiroshima 739-8526, Japan
[15]Research Institute of Earthquake and Volcano Geology, AIST, Tsukuba 305-8567, Japan
[16]Department of Earth and Planetary Science, The University of Tokyo, Tokyo 113-0033, Japan
[17]School of Earth and Space Exploration, Arizona State University, Tempe, AZ 85287-6004, USA
[18]Mantle Drilling Promotion Office, Institute for Marine-Earth Exploration and Engineering (MarE3),
JAMSTEC, Yokohama 236-0001, Japan

Correspondence: Susumu Umino (sesumin@staff.kanazawa-u.ac.jp)
and Fumio Inagaki (inagaki@jamstec.go.jp)

Abstract. For more than half a century, exploring a complete sequence of the oceanic crust from the seafloor through the Mohorovičić discontinuity (Moho) and into the uppermost mantle has been one of the most challenging missions of scientific ocean drilling. Such a scientific and technological achievement would provide humankind with profound insights into the largest realm of our planet and expand our fundamental understanding of Earth's deep interior and its geodynamic behavior. The formation of new oceanic crust at mid-ocean ridges and its subsequent aging over millions of years, leading to subduction, arc volcanism, and recycling of some

components into the mantle, comprise the dominant geological cycle of matter and energy on Earth. Although previous scientific ocean drilling has cored some drill holes into old (> 110 Ma) and young (< 20 Ma) ocean crust, our sampling remains relatively shallow (< 2 km into intact crust) and unrepresentative of average oceanic crust. To date, no hole penetrates more than 100 m into intact average-aged oceanic crust that records the long-term history of seawater–basalt exchange (60 to 90 Myr). In addition, the nature, extent, and evolution of the deep subseafloor biosphere within oceanic crust remains poorly known. To address these fundamentally significant scientific issues, an international workshop "Exploring Deep Oceanic Crust off Hawai'i" brought together 106 scientists and engineers from 16 countries that represented the entire spectrum of disciplines, including petrologists, geophysicists, geochemists, microbiologists, geodynamic modelers, and drilling/logging engineers. The aim of the workshop was to develop a full International Ocean Discovery Program (IODP) proposal to drill a 2.5 km deep hole into oceanic crust on the North Arch off Hawai'i with the drilling research vessel *Chikyu*. This drill hole would provide samples down to cumulate gabbros of mature (~ 80 Ma) oceanic crust formed at a half spreading rate of ~ 3.5 cm a^{-1}. A Moho reflection has been observed at ~ 5.5 km below the seafloor at this site, and the workshop concluded that the proposed 2.5 km deep scientific drilling on the North Arch off Hawai'i would provide an essential "pilot hole" to inform the design of future mantle drilling.

1   Introduction

Sampling a complete section of the oceanic crust and upper mantle has been a primary goal of scientific ocean drilling since its inception with Project MoHole (National Research Council, 1957; Teagle and Ildefonse, 2011). However, despite more than a half century's effort, we have not yet managed to reach kilometers below the seafloor to the Mohorovičić discontinuity (Moho) and the underlying mantle. One of the technical difficulties of establishing a drill hole several kilometers deep is collapse of an uncased borehole, due to substantial lithostatic load and increasing temperatures. To prevent borehole collapse, riser-drilling technology is required for deep drilling to stabilize the borehole and remove cuttings. In 2005, the riser-drilling research vessel *Chikyu* was commissioned with the expressed ultimate goal of exploring the upper mantle (Umino et al., 2013). After 15 years of riser operations by the *Chikyu*, mantle drilling now comes into the realm of technical feasibility.

To accomplish arguably the most ambitious mission ever proposed in Earth sciences, we must appreciate two significant constraints: the capabilities of the riser-drilling system on the *Chikyu* and the lifetime of the vessel. The current *Chikyu* riser system using a blow-out preventer (BOP) and 21 in. standard riser pipes can be deployed at a maximum of 2500 m below sea level (m b.s.l.). Recent, albeit untested, technical investigations indicate that by using slimline, 16 in. riser pipes, riser operations could be extended to ~ 4300 m b.s.l. The *Chikyu* is now 15 years into its operational life of 25 to 30 years. Consequently, it is imperative that the foundational steps for upper mantle drilling be initiated in the foreseeable future, such that drilling through the oceanic crust and into the upper mantle can be attempted during the operational lifetime of *Chikyu*.

Previous workshops have identified a limited number of sites globally where drilling intact ocean crust down into the mantle may be possible (Teagle and Ildefonse, 2011; Ildefonse et al., 2010); these include a relatively old site on the North Arch of the Hawaiian Islands. A seismic survey in support of future mantle drilling was conducted around the North Arch candidate site in 2017 through collaboration between the Japan Agency for Marine-Earth Science and Technology (JAMSTEC) and the University of Hawai'i (Fig. 1). This survey revealed undistorted primary structures of the Moho and the uppermost mantle around the proposed North Arch drill sites (Ohira et al., 2018). The SAKIGAKE-Japan Geoscience Union (JpGU) Hard Rock Drilling Focus Group Workshop was held in November 2018, Kanazawa, Japan, with participants from Japan, the USA, France, and Germany, to discuss the scientific rewards of drilling a complete section of upper oceanic crust on the North Arch of the Hawaiian Islands (Morishita et al., 2019).

IODP 951-Pre proposal "Drilling Middle Aged Oceanic Crust on North Arch off Hawai'i" was submitted in April 2019 and reviewed by the IODP Science Evaluation Panel (SEP) in June 2019. IODP 951-Pre proposal proposed to drill a complete upper crustal section to the uppermost gabbros in ~ 80 Ma crust spread at 7–8 cm a^{-1} on the North Arch off Hawai'i, where flexure of oceanic lithosphere due to loading of the Hawaiian Islands has raised the seafloor to ~ 4300 m b.s.l. due to the massive Hawaiian volcanoes (6–13 km tall) (Watts et al., 1985). The key advantages of this region relative to other MoHole candidates are its age and low heat flow (~ 55 mW m^{-2}) that predict relatively low temperatures at depth, and its relatively shallow Moho depth (~ 5.5 to 6 km below seafloor). The estimated crustal temperatures (< 50 °C at 2 km and < 150 °C at Moho depth) should diminish drilling and thermal stress-induced fracturing that has inhibited drilling in other deep holes (e.g., 5.9 Ma at Hole 504B and 15 Ma at Hole 1256D).

In December 2019, an ancillary workshop "Scientific Ocean Drilling Off Hawai'i with *Chikyu*" was held in San
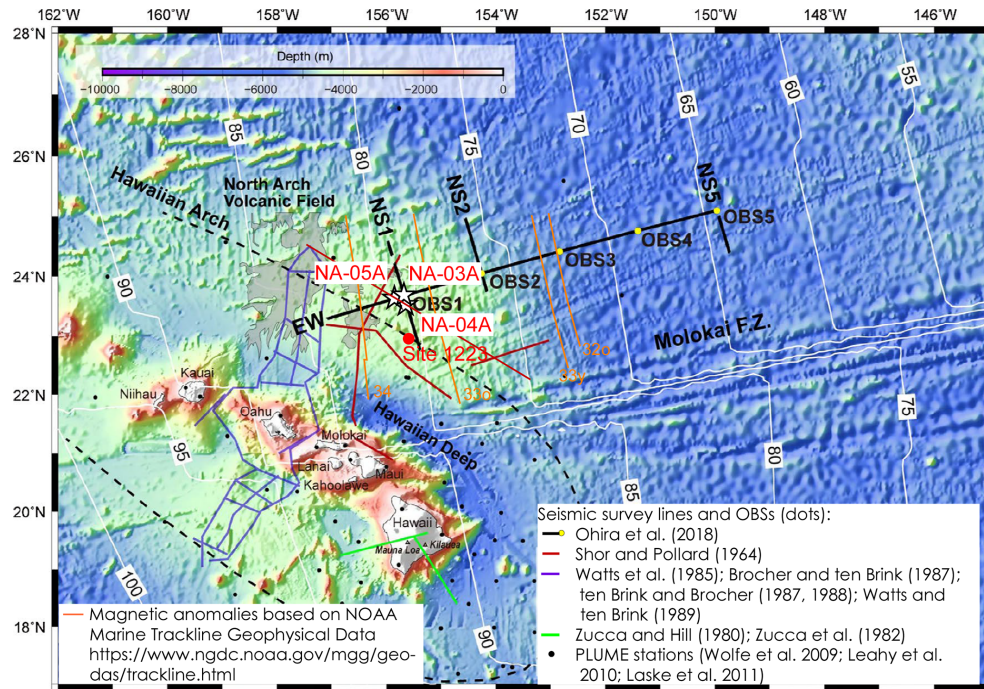
Figure 1. Proposed drill sites (primary site: NA-03A; alternative sites: NA-04A and NA-05A) and the bathymetry of the North Arch Volcanic Field (after Ohira et al., 2018). White lines with numbers are seafloor age (Ma) after Müller et al. (2008).

Francisco during the American Geophysical Union (AGU) Fall Meeting, where the updated information of the seismic analysis and other technological information related to the deep drilling off Hawaiʻi were discussed. Given the discussion at the AGU ancillary workshop and SEP recommendation, the "Exploring Deep Oceanic Crust off Hawaiʻi" workshop was organized to develop a 951-Full proposal in anticipation of future mantle drilling with *Chikyu*.

2 Workshop structure

The COVID-19 pandemic curtailed our initial plans for an early summer 2020 workshop in Honolulu, Hawaiʻi. Instead, "Exploring Deep Oceanic Crust off Hawaiʻi" was held online from 29 June to 1 July 2020. This 4 d virtual workshop engaged 106 registered participants from 16 countries (Fig. 2), following widespread advertisement through the Japan Drilling Earth Science Consortium (J-DESC), the U.S. Science Support Program (USSSP), the European Consortium for Ocean Research Drilling (ECORD) Science Operator (ESO), the Australian and New Zealand International Ocean Discovery Program Consortium (ANZIC), and JAMSTEC.

To take the time difference between participants in different parts of the world into account, each workshop day was subdivided into two 2 h sessions that covered different topics each day. A 2.5 h wrap-up plenary session was held on the final day. A web-based communication site was also

established, where all participants could upload/download all of the workshop-relevant files. The breakout sessions on days 1, 2, and 3 were focused on the following respective themes: "Crustal Evolution: Alteration & Aging" – discussion leaders: Takeshi Hanyu (JAMSTEC) and Damon Teagle (Univ. Southampton); "Crustal Architecture: Formation & Deformation" – discussion leaders: Michael Garcia (Univ. Hawaiʻi) and Laura Crispini (Univ. Genoa); and "Water & Deep Life" – discussion leaders: Fumio Inagaki (JAMSTEC) and Steven D'Hondt (Univ. Rhode Island). In each session, the discussion leader made a brief introduction, followed by a few invited presentations, flash-talks, and discussions of questions (Q), hypotheses (H), and approaches (A) appropriate to the session theme. On Day 4, the discussion leaders summarized the discussions, and the workshop co-chairs, Susumu Umino (Kanazawa Univ.) and Greg Moore (Univ. Hawaiʻi), summarized the outcomes and proposed consensus and action items towards building a compelling full proposal.

3 Oceanic crustal architecture

The formation of new oceanic crust at mid-ocean ridges, its subsequent aging and transformation over tens of million years, its eventual destruction in subduction zones, and its recycling through the Earth's mantle comprise the largest cycling of matter and energy on Earth. However, we are only beginning to comprehend the full diversity of oceanic crust; how it accretes along the $\sim 60\,000$ km of mid-ocean ridges;
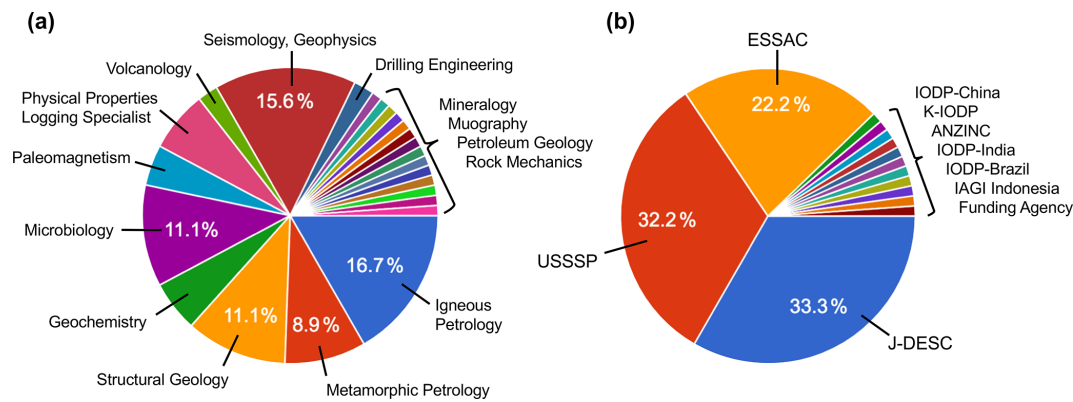
Figure 2. Statistics of the workshop participants. **(a)** Expertise of participants. **(b)** Locations of participants (based on the IODP Project Management Office and other information). The total number of registered participants was 106 from 16 nations.

in what manner it is chemically, physically, and biologically altered as it matures; and what fractions may be recycled in arcs or returned into the mantle.

Oceanic crust under the North Arch is a good candidate for understanding the physical, chemical, and biological evolution of mature oceanic lithosphere, as well as the effects of intraplate volcanism, and the regional history of hazardous landslides. Geological information from intact normal oceanic crust spread at 7–10 cm a^{-1} is key to understanding the changes in style of upper crustal extension from fast to intermediate spreading rates. Scientific ocean drilling on the North Arch off Hawai'i will help us to decipher the relationships between extension style, crustal architecture, deformation, and hydrothermal history of the crust. Drilling a 2.5 km deep pilot hole project using *Chikyu* will be the first tangible step toward achieving the ultimate goal of reaching the Moho.

Basic observations regarding the architecture of in situ present-day oceanic crust, including rock types, geochemistry, and thicknesses of the volcanic, dike, and plutonic sections, are yet to be made. It is a fundamental weakness of our knowledge of oceanic crust that we cannot yet relate seismic and magnetic imaging of the oceanic crust and geochemical inferences to basic geologic observations. We do not have a predictive understanding of the factors controlling thicknesses of seismic and geological layers in oceanic crust. This greatly precludes our ability to geologically interpret geophysical data or relate observations from drill holes to wider regional contexts.

The thickness of Layer 2 and the depth of axial magma chambers (AMC) show gradual increases with decreasing spreading rate from 22 to 10 cm a^{-1}. However, both parameters show very large ranges for spreading rates < 7 cm a^{-1} (Christeson et al., 2019), indicating that crustal architecture fundamentally changes between spreading rates of 10 and 7 cm a^{-1}. The crust north of Hawai'i spreads at ∼ 7 cm a^{-1}, which is at the lower end of this critical spreading rate interval. From available seismic data and current understand-

ing, we predict a Layer 2 thickness at the proposed site of ∼ 1700 to 2500 m. Similarly, mapping of ridge-axis lava morphology also changes across this spreading rate interval. For crust spread at rates above 10 cm a^{-1}, the extrusive sequence is more than 70 % sheet flows, whereas pillow lava dominates extrusives deposited at spreading rates below 7 cm a^{-1} (see Morishita et al., 2019). Lava morphology is also affected by extrusion rate and basement slopes (Gregg and Fink, 1995; Umino et al., 2003). The profound change in dominant lava morphology at 7–10 cm a^{-1} suggests that major changes in magma plumbing system and topography arise from changes in crustal architecture at the transition from fast- to intermediate-spreading rates. The spreading rate relationship predicts almost equal proportions of pillow and sheet flows among extrusive layers in the North Arch crust.

The geological meaning and physical causes of the transition from seismic Layer 2 to Layer 3 velocities remain poorly understood. In Hole 504B, the only place where the Layer 2–3 transition has been penetrated in situ, this transition occurs near the middle of the ∼ 1 km thick sheeted dike complex. The transition to gabbroic rocks is at least 600 m deeper in the crust (Alt et al., 1993; Detrick et al., 1994). At Site 504, velocity gradient changes appear related to changes in the secondary hydrothermal mineralogy (Alt et al., 1996) and/or crack porosity (Carlson, 2010). The wider applicability of observations from intermediate-spreading-rate crust sampled in Hole 504B is yet to be tested. However, Hole 1256D reached gabbroic rocks, albeit at shallower levels, but still clearly within seismic Layer 2 (Gilbert and Salisbury, 2011).

The large (800 m) uncertainty in Layer 2 thickness (1700–2500 m) off Hawai'i spans the ranges of the East Pacific Rise (EPR) and the Galapagos Spreading Center (GSC), precluding explicit conclusions. Considering the range in spreading rate (4.9–7.2 cm a^{-1}) along the entire GSC system, we may assume that the crust north of Hawai'i follows the GSC trend. Consequently, we predict ∼ 780 ± 45 m thick extrusive sequence and 1320 ± 440 m thick sheeted dikes, assuming the Layer 2A–2B boundary matches the extrusive-sheeted dike
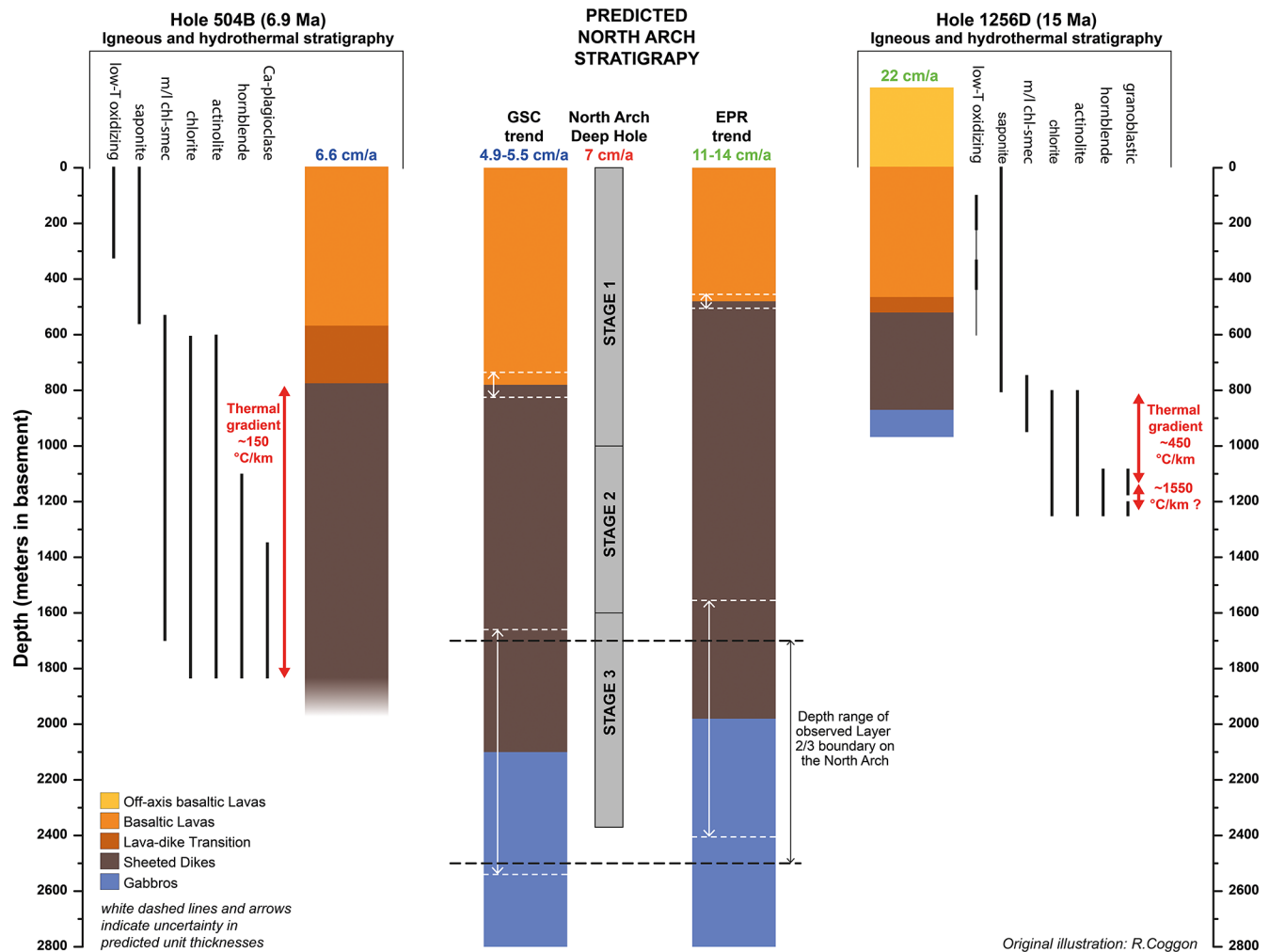
Figure 3. Holes 504B and 1256D rock type hydrothermal stratigraphies, and the predicted North Arch rock type stratigraphy (Phipps Morgan and Chen, 1993). The significantly different sheeted dike thicknesses at holes 504B and 1256D resulted in their dramatically different thermal regimes. The North Arch is located on crust formed at a spreading rate intermediate between 504B (6.6 cm a^{-1}) and 1256D (22 cm a^{-1}). Distinct ocean crustal architectures are predicted on the basis of seismic observations from the Galapagos Spreading Center (GSC) and the East Pacific Rise (EPR). Given the North Arch spreading rate of ~ 7 cm a^{-1}, we hypothesize that the crustal architecture will be similar to that predicted from the GSC trend. Holes 504B and 1256D stratigraphies and mineral distributions after Teagle et al. (2006).

transition (Fig. 3). The architecture of oceanic crust under the North Arch will be investigated by integrating wire-line logging and core observations to determine the stratigraphic variation of lithology and structures.

Primary hypothesis. The North Arch oceanic crust, formed at an intermediate spreading rate, comprises an intact 740–820 m thick sequence of about 50 : 50 pillow and sheet flows overlying a robust 880–1770 m thick sheeted dike complex.

The 2.5 km deep crustal drilling on the North Arch will drill though three major lithologic zones of the oceanic crust underlying ~ 130 m thick sediments: basaltic lava, sheeted dike complex, and gabbros (Fig. 3). Core descriptions; detailed petrological, geochemical, 2D- and 3D-microstructural

investigations; and wire-line logging observations will allow us to map hydrothermal pathways and fluid–rock exchanges through the crust, to examine the interactions between hydrothermal, magmatic, and tectonic processes that influence the architecture of the crust.

Drilling on the North Arch will allow us to evaluate the role that axial hydrothermal processes related to initial cooling and magma crystallization play in controlling melt distribution and tectonic deformation and, hence, oceanic crustal architecture. Importantly, hydrothermal alteration impacts the physical properties of oceanic crust and, therefore, complicates interpretation of regional geophysical data. Critically, understanding on/near-axis hydrothermal circulation requires a better knowledge of whether fluid flow on recharge and discharge paths is pervasive (grain boundary or small

fractures) or is channeled by larger features (faults, pipes, or dikes) that concentrate thermal and chemical hydrothermal exchange. Thus, the following questions need to be answered:

- What is the role of lateral and vertical channeling on fluid flow and hydrothermal exchange?

- Is fluid flow focused by features such as boundaries between rock types, deformation zones, flow tops, and faults?

- What are the differences between measured permeability (porosity) and paleo-permeabilities (-porosities) and how would they affect fluid flow modeling?

4 Hydrothermal alteration of mature oceanic crust

The chemical and isotopic composition of seawater reflects the dynamic balance between riverine inputs from continents, burial of marine sediment, and hydrothermal exchanges with oceanic crust. Compared with continental crust, oceanic crust is young and chemically relatively homogeneous, and chemical exchanges with seawater are limited to a relatively few well-known reactions. Consequently, hydrothermal contributions to ocean chemistry are simpler to reconstruct than riverine inputs (Bickle and Teagle, 1992; Coogan, 2008; Coggon et al, 2010; Coggon and Teagle, 2011; Davis et al. 2003; Vance et al., 2009). Knowledge of the rates, depths, and magnitudes of low-temperature hydrothermal exchanges in aging oceanic crust would help us to decipher the changing global conditions responsible for past variations in seawater chemistry. Addressing these issues requires recovery of oceanic crust of different ages, from ridge flanks with different spreading and hydrogeologic histories.

Hydrothermally altered oceanic crust provides a record of geochemical exchange with seawater through changes in its chemical and isotopic composition, mineral assemblages, and physical properties (e.g., porosity, permeability, and seismic velocities). The intensity of this exchange reflects the complex interplay of seawater chemistry; the crust's age, spreading rate, thermal history, and accretion style; and the nature of the volcanic stratigraphy, availability of fluid pathways, basement topography and proximity of seamounts, as well as the sediment type, thickness, and accumulation rates that reflect the crust's journey across the seafloor. The recovered cores will improve our knowledge of the temporal and depth limits of chemical exchange across the aging ridge flanks. The analyses of cores will allow us to develop a more complete record of hydrothermal exchange between the ocean and oceanic crust and to better quantify the influence of the life cycle of tectonic plates on long-term biogeochemical cycling of key chemicals, including volatile species, such as noble gases, H_2O, CO_2, N_2, S, B, and Li, that we use to trace the evolution of our planet (e.g., Kendrick et al., 2017).

Extensive high-temperature hydrothermal exchanges ($> 350\,°C$) are necessarily associated with cooling and crystallization of magma at mid-ocean ridges, due to the great energy requirements for heating seawater to near critical-point temperatures or beyond. However, low- to moderate-temperature reactions are common, and they are principally driven by conductive heat from cooling of oceanic lithosphere and hydrological heads established by interaction of basement topography, relatively permeable zones within oceanic basement, and the extent and style of sediment cover. Whether these reactions continue throughout maturation of oceanic crust or are episodic remains poorly constrained. There is a discernible conductive heat flow anomaly out to an average of $\sim 65\,Ma$ (Stein and Stein, 1994), suggesting active advection of heat by fluid flow to this age. However, dating of secondary minerals recovered from oceanic crust suggests that most secondary minerals form within 20 Myr of crustal formation (e.g., Coggon et al., 2010; Coogan et al., 2016). The question then arises as to whether heat could be advected by basement fluids without leaving a discernible chemical or mineralogical trace of this fluid flow?

The perception that secondary mineral formation is completed at relatively young crustal age, before the crust is thermally sealed, may reflect our sampling bias toward heavily sedimented crust. The proposed primary site is covered by only $\sim 110\,m$ of sediment, $\sim 1\sigma$ below the global average sediment thickness for $\sim 80\,Ma$ crust ($350 \pm 250\,m$; Spinelli et al., 2004). The North Arch site provides a unique opportunity to investigate the timing and duration of ridge flank hydrothermal exchanges.

The importance of these issues is well illustrated by uncertainties regarding the uptake of CO_2 by the oceanic crust (e.g., Alt and Teagle, 1999; Staudigel et al., 1989). Due to these uncertainties, it is unclear whether oceanic crust is a source or sink of CO_2 in global geochemical cycles (Berner et al., 1983). Observations of oceanic crust sampled by drilling indicate that old crust ($> 110\,Ma$) has a much higher carbonate content than young crust ($< 15\,Ma$; see Alt and Teagle, 1999; Fig. 4). Is this difference related to progressive carbonization with age or the fact that carbonate uptake was relatively rapid in the Cretaceous and Paleogene reflecting seawater chemistry and conditions at the time of crustal formation? To answer this critical question, we must recover intermediate-age crust to determine its carbonate content, and when it was added to the crust. To address these scientific problems, we will deploy a combination of petrological and geochemical analyses, radiometric dating, and quantitative core-wire-line log integration of rock types, alteration features, and veins.

The second obstacle to developing a comprehensive record of hydrothermal exchange between the ocean and oceanic crust is our complete lack of samples from which to quantify the role of chemical exchange in deep oceanic crust older than 15 Ma. Previous models of the mantle volatile
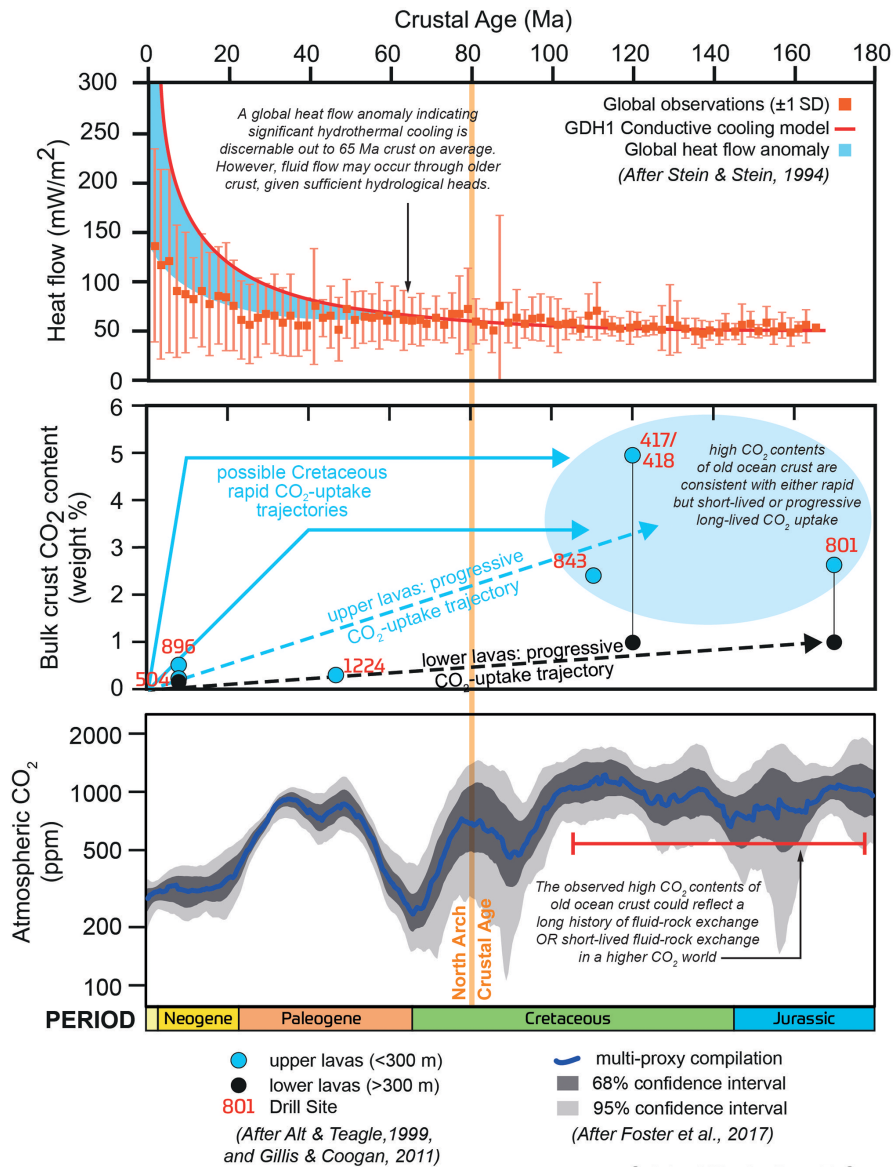
Figure 4. Drilling into the ∼ 80 Ma oceanic crust on the North Arch will allow us to determine what controls the duration and rate of CO_2 uptake by the oceanic crust and to quantify the role of hydrothermal aging in the long-term global carbon cycle.

cycle assume low volatile concentrations in lower oceanic crust relative to upper crust (e.g., Dasgupta and Hirschmann, 2010). However, the concentrations of some important elements (e.g., B; see Sano et al., 2008) are much higher in the Hole 1256D dikes and gabbros than previously estimated, indicating deeper exchange with seawater-derived hydrothermal fluids.

Much of our current knowledge comes from ophiolites, which are ancient blocks of oceanic crust preserved on land (e.g., Gregory and Taylor, 1981; Coggon et al., 2016). However, many of the best studied ophiolite massifs, such as Troodos or Oman, formed in complex supra-subduction zone settings. Consequently, observations from ophiolites remain

controversial and poorly tested by observations from intact oceanic crust. Where dikes and gabbros are exposed in ophiolites they commonly display abundant veining and bulk-rock alteration to sub-greenschist and zeolite facies assemblages (e.g., prehnite, quartz, chlorite-smectite, laumontite, and other zeolites ± carbonates; see Kelemen et al., 2020). These assemblages overprint higher temperature background and channeled hydrothermal alteration (e.g., amphibole and epidote veins) that relate to active hydrothermal circulation, but their absolute timing is difficult to determine. Consequently, whether these phases record deep, off-axis hydrothermal exchanges or fluid–rock reactions specific to emplacement of the ophiolite remains unresolved.

The sub-greenschist to zeolite assemblages in the dikes and gabbros from holes 504B and 1256D are not present to the same extents/styles as in ophiolites. It is most commonly assumed that high-temperature mineral precipitation in dikes and gabbros restricts off-axis fluid flow to more fractured and/or brecciated zones within the volcanic series, with fluid flow driven by heat conduction from the lithosphere below. However, deep off-axis penetration of seawater-derived hydrothermal fluid is possible, either pervasively or, more likely, channeled along specific conduits such as faults. These hypothetical reactions may occur between deep, relatively fresh diabase and gabbro at low to moderate temperatures ($< 150\,°C$) and could provide energy and nutrients for hitherto unrecognized deep microbial communities and additional unquantified fluid–rock exchanges between seawater and oceanic crust. The deep (~ 2500 m subbasement) hole on the North Arch will complement observations from the younger holes 504B and 1256D and test the applicability of ideas and quantifications developed from ophiolites.

Primary hypothesis. Hydrothermal exchanges between the oceanic crust and seawater are episodic, not continuous. Consequently, the extent of fluid–rock exchange does not just depend on age of the oceanic crust but also depends on external factors that enhance fluid flow and reaction. As a result, there may not be simple relationships between crustal age, fluid flow, thermal and chemical exchange, and biological activity.

The proposed North Arch drilling project will recover, for the first time, sheeted dikes and upper gabbros in mature crust (> 15 Ma) that has experienced the full range of fluid–rock exchanges that occur over a significant period that would be representative of typical oceanic crust before it is subducted in the western Pacific. These observations will provide a unique opportunity to develop a more complete record of hydrothermal exchange between the ocean and oceanic crust.

5   Nature and extent of life in the oceanic crust

The samples and data from the drilling project on the North Arch will address the physical and chemical limits of subseafloor life. This project will determine the extents to which microbial communities colonize and persist in successively deeper layers of volcanic extrusive rocks, dikes, and upper gabbroic basement in oceanic crust, and in complex transition zones between these layers. The frequency of encountering microbial communities within the recovered rock will illuminate the ease by which they disperse and find new resources. The project will identify the diversity and compositions of these communities; it will illuminate their origin by testing their phylogenetic relationships to microbes in the overlying sediment and in the surface world; and it will ad-

vance understanding of the mechanisms that they use to generate energy and fix carbon far from the influence of Earth's surface (photosynthetic) environments. The expected results will clarify their global significance by examining relationships between their capabilities and the alteration histories of their habitats.

Previous scientific ocean drilling has demonstrated that bacteria, archaea, fungi, and viruses inhabit marine sediment (D'Hondt et al., 2004; Inagaki et al., 2006, 2015; Orsi et al., 2013; Engelhardt et al., 2014; Liu et al., 2017; Hoshino et al., 2020) and the shallow basaltic aquifer that underlies marine sediment (Cowen et al., 2003; Lever et al., 2013; Ivarsson et al., 2016; Jørgensen and Zhao, 2016; Nigro et al., 2017; Quemener et al., 2020; Suzuki et al., 2020). A few studies have reported evidence of microbial communities in North Atlantic gabbroic lower crust exposed by faulting (Alt et al., 2007; Mason et al., 2010; Li et al., 2020). As there are no studies of microbial communities from gabbros in intact crust overlain by extrusive and dike sequences, it is not clear if these fault-exposed communities are indigenous to normal lower crust or were locally introduced from the ocean via fluid circulation in faulted near-seafloor sequences.

Secondary mineralization is ubiquitous in oceanic crust. Different minerals precipitate at different stages in crustal evolution, as temperature declines and fluid-flow paths evolve and become restricted. For example, celadonite and iron oxyhydroxides precipitate at low temperatures in young crust, whereas calcite and zeolite tend to precipitate relatively late in the alteration sequence (Alt, 1995; Alt and Teagle, 1999). Temperature typically decreases with crustal age but increases with depth in crust. As a result, secondary minerals at greater crustal depths (e.g., albite, chlorite, and epidote in the sheeted dikes) precipitate at much higher temperatures than the minerals at shallow depths (in the extrusive volcanics) (Alt, 1995). As crust cools with age, the zone of low-temperature mineralization may migrate downward to depths previously characterized by high-temperature mineralization. However, this has not yet been tested in mature intact oceanic crust.

Recent studies reported that microbes are abundant in specific secondary minerals in shallow cores (< 100 m) into old (33.5–104 Ma), cold crust of the South Pacific (Suzuki et al., 2020) (Fig. 5). The microbes are associated with iron-rich smectite at interfaces between basalt wall-rocks and celadonite $+$ iron oxyhydroxide veins. The microbe-bearing smectites are late-stage secondary minerals associated closely with early-stage minerals (celadonite, iron oxyhydroxide). The crust age of the oldest South Pacific samples (104 Ma) is ~ 24 Ma older than the drill site on the North Arch, underscoring the potential for direct detection of microbes in mineral-filled veins in deeper realms. Coring the successive layers of upper oceanic crust at the North Arch site (extrusives, dikes, upper gabbro) will provide a unique opportunity to determine how deeply microbial communities penetrate into mature oceanic crust.
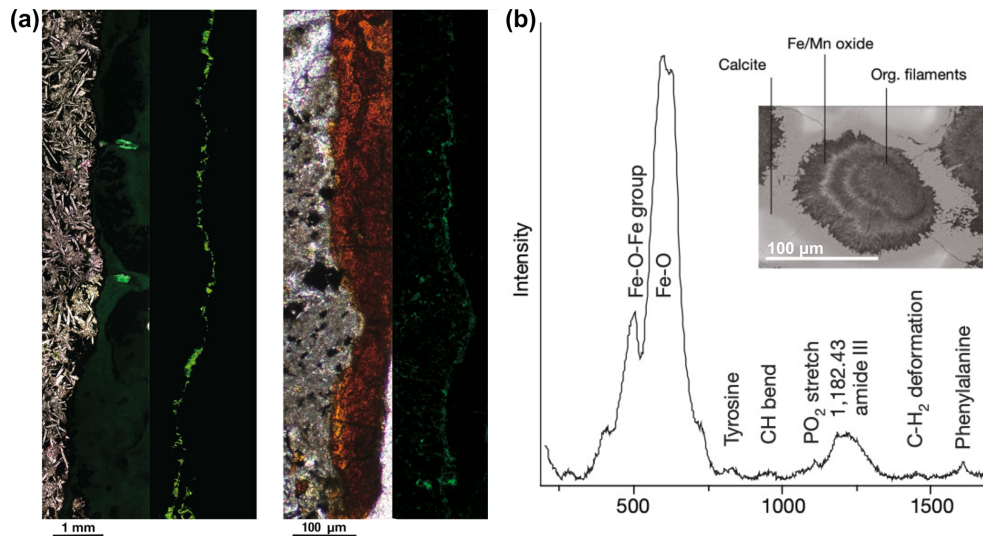
Figure 5. (a) Abundant microbes in secondary minerals (smectite) at basalt–mineral interfaces from IODP Hole U1365E. Light and fluorescence microscopy images of SYBR Green I-stained microbial cells in a fracture filled with celadonite from U1365E-8R4 and a vein filled with iron oxyhydroxides from Site U1365E-12R2 (Suzuki et al., 2020). **(b)** Confocal Raman analysis of organic inclusions in calcite from Atlantis Bank (fault-exhumed lower crust), IODP Hole 1473A (Li et al., 2020).

The distributions, compositions, activities, and biogeochemical consequences of microbial communities in oceanic crust are largely unknown. It is not known if microbial colonies persist on the basement surface after burial by sediment. Most importantly, nothing is known about the presence or absence, environmental associations, characteristics, or consequences of microbial communities in the intrusive dikes or gabbroic crust beneath intact extrusive sequences. Relationships of habitats and communities in the shallow extrusive sequence to habitats and communities (if present) in the deeper volcanic rocks, the underlying dikes, and the gabbros below are completely unknown.

Relationships between microbes in the extrusive crust and microbes in the overlying sediment are poorly understood (Labonté et al., 2017). Associations between minerals and microbial occurrences in subseafloor sediment are unexamined. Thus, this poses the following question: are similar microbes associated with similar minerals in both crust and sediment? In both sediment and crust, whether the habitat is oxic or anoxic appears to set a fundamental constraint on both community composition and dominant microbial activities. Anoxic environments are characterized by anaerobic communities and activities, whereas oxic subseafloor environments are characterized by aerobic communities and activities (Cowen et al., 2003; Huber et al., 2006; Meyer et al., 2016; Tully et al., 2018).

The metabolic activities that sustain microbial communities in shallow crust are poorly constrained. Potential consequences of those activities include chemical alteration of the crust, precipitation of secondary minerals, and microbially induced fracture filling. To the extent that they mediate these processes, crustal communities shape the chemical composition of the ocean and crust, as well as the physical structure of the crust (Thorseth et al., 1995; Bach and Edwards, 2003; D'Hondt et al., 2019).

Processes that might support life in oceanic crust include oxidation of (i) reduced elements in the crust, (ii) dissolved organic matter (DOM) that enters with seawater (Shah-Walter et al., 2018), abiotic organic matter and/or H_2 from serpentinization (Klein et al., 2015; Ménez et al., 2018; Majumdar et al., 2020), (iii) fault-induced (mechanically produced) H_2 production, and (iv) H_2 from in situ water radiolysis (D'Hondt et al., 2019). All of these processes require oxidants, which can be dissolved chemicals (O_2, NO_3^-, SO_4^{2-}) carried by diffusion or flow of seawater into the subseafloor, oxidized elements in minerals, and oxidants created by water radiolysis (e.g., H_2O_2) (D'Hondt et al., 2019).

It seems likely, although untested, that the metabolic importance of these processes changes with crust depth; seawater DOM is likely to disappear with increasing depth, whereas H_2 and CH_4 produced by serpentinization (Majumdar et al., 2020; Klein et al., 2019) and transported from greater depth may appear with increasing depth. Radiolytic H_2 and radiolytic oxidants (Dzaugis et al., 2016) may increase in metabolic importance as fluxes of DOM and oxidants from seawater decrease with increasing depth. The relative importance of these processes is likely to depend on crust permeability and void connectivity; deep off-axis penetration of seawater-derived hydrothermal fluid could be pervasive or channeled along faults. Resultant oxidation of diabase, gabbro, and mineral-bound abiotic organic matter at low temperatures ($< 150\,°C$) could help to sustain microbial

communities in the dikes and gabbroic crust deep beneath the ocean.

Primary hypothesis. In mature oceanic crust cooler than the thermal limit to life, water–rock interactions sustain microbial life as deeply as seawater-derived fluid penetrates.

Coring the successive layers of sediment and upper oceanic crust to gabbro at the North Arch site will provide a unique opportunity to determine how compositions and activities of microbial communities change with depth in mature oceanic crust, in response to lithologic boundaries, and/or physical and chemical conditions. Because contamination of rock surfaces by microbes is ubiquitous in hard-rock drilling, we will particularly focus on searching for microbial communities and biosignatures within vein-filling minerals (e.g., Suzuki et al., 2020).

6   Conclusion

During the virtual workshop "Exploring Deep Oceanic Crust off Hawai'i", we discussed how, through scientific drilling, we would investigate the physical, chemical, and biological architecture and evolution of the ocean crust to test three major hypotheses: (1) the North Arch crust spread at an intermediate rate will comprise an intact 500–800 m thick extrusive sequence with equal proportions of pillow and sheet flows, overlying a thick (1300–1600 m) sheeted dike complex; (2) hydrothermal exchanges between the ocean crust and seawater are episodic, and the extent of fluid–rock exchange does not just reflect the age of the crust but external factors that enhance fluid flow and reaction; and (3) in ocean crust cooler than the thermal limit to life, water–rock interactions sustain microbial life as deeply as seawater-derived fluid penetrates. In addition, scientific drilling will provide insights into North Arch volcanism and hazardous giant landslides from the Hawaiian volcanoes. Consequently, the major objectives during the 2.5 km deep crustal drilling on the North Arch will be to

- determine the structure and petrology of the extrusive lavas, sheeted dike complex, upper gabbros, and their correlations with seismic layers, specifically the nature of the Layer 2–3 transition;

- investigate the history of deformation and its relationships to spreading, and hydrothermal fluid-flow;

- evaluate the nature of the conductive thermal boundary layer between the axial magmatic chamber and the overlying sheeted dikes and make the first direct observations of the uppermost cumulate rocks;

- evaluate the extent and mode of tectonic disturbance and geochemical alteration by flexure of mature Pacific lithosphere and North Arch volcanism;

- determine a longer-term sedimentary record of giant landslides;

- compare hydrothermal alteration of mature (~ 80 Ma) intact ocean crust with younger (e.g., holes 504B, 1256D) and older (e.g., Hole 801C), and slow-spreading crust (e.g., IODP Expeditions 390/393 South Atlantic Transect);

- determine the nature, relative timing and absolute ages, and formation temperatures of successive alteration minerals, and quantify the extents of hydrothermal exchanges for fluid-mobile elements and volatiles;

- determine the depth limit of low-temperature hydrothermal alteration and quantify the associated chemical exchange;

- investigate the compositions and the extent of microbial communities in vein-filling secondary minerals in the deeper crust and their phylogenetic relationships to microbes in the overlying sediment and in the surface world;

- identify relationships between in situ metabolic gene expression, microbial capabilities under experimental conditions, alteration history, and physical/chemical gradients from the sediment–crust interface to the upper gabbros.

These overarching scientific objectives are strongly connected, and progress on each objective is tightly related to progress on the others.

During this workshop, the participants agreed that the 2.5 km deep drilling project on the North Arch off Hawai'i should be placed as a "pilot hole" to inform the design of a future MoHole and gain experience in deep hard-rock drilling with *Chikyu*. Participants also agreed that the action will be a cornerstone project that contributes to the Flagship Initiatives "2. Probing the Deep Earth" and "5. Exploring Life and Its Origins" in the 2050 Science Framework (Koppers and Coggon, 2020).

Author contributions. SU and GFM co-chaired the workshop. NA, NX, YY, and FI organized the workshop. LC, SD'H, MOG, TH, DAHT, and FI led breakout sessions as the discussion leaders. SU, GFM, BB, RC, LC, SD'H, MOG, TH, FK, NS, DAHT, MT, MY, MH, BI, IK, YK, YS, ETR, and YY contributed to IODP 951-Full proposal development as the proponent. SU, GFM, RC, LC, SD'H, MOG, TH, NS, DAHT, NX, YY, and FI co-wrote the paper with input from all co-authors.

References

Alt, J. C. and Teagle, D. A. H.: The uptake of carbon during alteration of ocean crust, Geochim. Cosmochim. Ac., 63, 1527–1535, https://doi.org/10.1016/S0016-7037(99)00123-4, 1999.

Alt, J. C.: Subseafloor Processes in Mid-Ocean Ridge Hydrothennal Systems, Seafloor Hydrothermal Systems: Physical, Chemical, Biological, and Geological Interactions, 91, 85–114, https://doi.org/10.1029/GM091p0085, 1995.

Alt, J. C., Kinoshita, H., Stokking, L. B., and Shipboad Scientific Party: Initial Reports, College Station, TX (Ocean Drilling Program), Proc. ODP, Init. Repts., 148, https://doi.org/10.2973/odp.proc.ir.148.1993, 1993.

Alt, J. C., Kinoshita, H., Stokking, L. B., and Michael, P. J. (Eds.): Scientific Results, College Station, TX (Ocean Drilling Program), Proc. ODP, Sci. Results, 148, https://doi.org/10.2973/odp.proc.sr.148.1996, 1996.

Alt, J. C., Shanks, W. C., Bach, W., Holger, P., Garrido, C. J., and Beaudoin, G.: Hydrothermal alteration and microbial sulfate reduction in peridotite and gabbro exposed by detachment faulting at the Mid-Atlantic Ridge, 15°20′ N (ODP Leg 209): A sulfur and oxygen isotope study, Geochem. Geophy. Geosy., 8, Q08002, https://doi.org/10.1029/2007GC001617, 2007.

Bach, W. and Edwards, K. J.: Iron and sulfide oxidation within the basaltic ocean crust: implications for chemolithoautotrophic microbial biomass production, Geochim. Cosmochim. Ac., 67, 3871–3887, https://doi.org/10.1016/S0016-7037(03)00304-1, 2003.

Berner, R. A., Lasaga, A. C., and Garrels, R. M.: The carbonate-silicate geochemical cycle and its effect on atmospheric carbon dioxide over the past 100 million years, Am. J. Sci., 283, 641–683, https://doi.org/10.2475/ajs.283.7.641, 1983.

Bickle, M. J. and Teagle, D. A. H.: Strontium alteration in the Troodos ophiolite: implications for fluid fluxes and geochemical transport in mid-ocean ridge hydrothermal systems, Earth Planet. Sc. Lett., 113, 219–237, https://doi.org/10.1016/0012-821X(92)90221-G, 1992.

Brocher, T. M. and ten Brink, U. S.: Variations in oceanic layer 2 elastic velocities near Hawaii and their correlation to lithospheric flexure, J. Geophys. Res.-Atmos., 92, 2647–2661, https://doi.org/10.1029/JB092iB03p02647, 1987.

Carlson, R. L.: How crack porosity and shape control seismic velocities in the upper oceanic crust: Modeling downhole logs from Holes 504B and 1256D, Geochem. Geophy. Geosy., 11, Q04007, https://doi.org/10.1029/2009GC002955, 2010.

Christeson, G. L., Goff, J. A., and Reece, R. S.: Synthesis of oceanic crustal structure from two-dimensional seismic profiles, Rev. Geophys., 57, 504–529, https://doi.org/10.1029/2019RG000641, 2019.

Coggon, R. M. and Teagle, D. A. H.: Hydrothermal calcium-carbonate veins reveal past ocean chemistry, TrAC-Trend. Anal. Chem., 30, 1252–1268, https://doi.org/10.1016/j.trac.2011.02.011, 2011.

Coggon, R. M., Teagle, D. A. H., Smith-Duque, C. E., Alt, J. C., and Cooper, M. J.: Reconstructing past seawater Mg/Ca and Sr/Ca from mid-ocean ridge flank calcium carbonate veins, Science, 327, 1114–1117, https://doi.org/10.1126/science.1182252, 2010.

Coggon, R. M., Teagle, D. A. H., Harris, M., Davidson, G. J., Alt, J. C., and Brewer, T. S.: Hydrothermal contributions to global biogeochemical cycles: Insights from the Macquarie Island ophiolite, Lithos, 264, 329–347, https://doi.org/10.1016/j.lithos.2016.08.024, 2016.

Coogan, L. A.: Reconciling temperatures of metamorphism, fluid fluxes, and heat transport in the upper crust at intermediate to fast spreading mid-ocean ridges, Geochem. Geophy. Geosy., 9 Q02013, https://doi.org/10.1029/2007GC001787, 2008.

Coogan, L. A., Parrish, R. R., and Roberts, N. M. W.: Early hydrothermal carbon uptake by the upper oceanic crust: Insight from in situ U-Pb dating, Geology, 44, 147–150, https://doi.org/10.1130/G37212.1, 2016.

Cowen, J. P., Giovannoni, S. J., Kenig, F., Johnson, H. P., Butterfield, D., Rappé, M. S., Hutnak, M., and Lam, P.: Fluids from aging ocean crust that support microbial life, Science, 299, 120–123, https://doi.org/10.1126/science.1075653, 2003.

Dasgupta, R. and Hirschmann, M. M.: The deep carbon cycle and melting in Earth's interior, Earth Planet. Sc. Lett., 298, 1–13, https://doi.org/10.1016/j.epsl.2010.06.039, 2010.

Davis, A. C., Bickle, M. J., and Teagle, D. A. H.: Imbalance in the oceanic strontium budget, Earth Planet. Sci. Lett., 211, 173–187, https://doi.org/10.1016/S0012-821X(03)00191-2, 2003.

Detrick, R., Collins, J., Stephen, R., and Swift, S.: In situ evidence for the nature of the seismic layer 2/3 boundary in oceanic crust, Nature, 370, 288–290, https://doi.org/10.1038/370288a0, 1994.

D'Hondt, S., Jørgensen, B. B., Miller, D. J., Batzke, A., Blake, R., Cragg, B. A., Cypionka, H., Dickens, G. R., Ferdelman, T., Hinrichs, K-U., Holm, N. G., Mitterer, R., Spivack, A., Wang, G., Bekins, B., Engelen, B., Ford, K., Gettemy, G., Rutherford, S. D., Sass, H., Skilbeck, C. G., Aiello, I. W., Guerin, G., House, C., Inagaki, F., Meister, P., Naehr, T., Niitsuma, S., Parkes, R. J., Schippers, A., Smith, D. C., Teske, A., Wiegel, J., Padilla, C. N., and Acosta, J. L. S.: Distributions of metabolic activities in deep subseafloor sediments, Science, 306, 2216–2201, https://doi.org/10.1126/science.1101155, 2004.

D'Hondt, S., Pockalny, R., Fulfer, V. M., and Spivack, A. J.: Subseafloor life and its biogeochemical impacts, Nat. Commun., 10, 3519, https://doi.org/10.1038/s41467-019-11450-z, 2019.

Dzaugis, M. E., Spivack, A. J., Dunlea, A. G., Murray, R. W., and D'Hondt, S.: Radiolytic hydrogen production in the subseafloor basaltic aquifer, Front. Microbiol., 7, 76, https://doi.org/10.3389/fmicb.2016.00076, 2016.

Engelhardt, T., Kallmeyer, J., Cypionka, H., and Engelen, B.: High virus-to-cell ratios indicate ongoing production of

viruses in deep subsurface sediments, ISME J,, 8, 1503–1509, https://doi.org/10.1038/ismej.2013.245, 2014.

Gilbert, L. A. and Salisbury, M. H.: Oceanic crustal velocities from laboratory and logging measurements of Integrated Ocean Drilling Program Hole 1256D, Geochem. Geophy. Geosy., 12, Q09001, https://doi.org/10.1029/2011GC003750, 2011.

Gregg, T. K. P. and Fink, J. H.: Quantification of submarine lava-flow morphology through analog experiments, Geology, 23, 73–76, https://doi.org/10.1130/0091-7613(1995)023<0073:QOSLFM>2.3.CO;2, 1995.

Gregory, R. T. and Taylor, H. P.: An oxygen isotope profile in a section of Cretaceous oceanic crust, Samail Ophiolite, Oman: Evidence for $\delta^{18}O$ buffering of the oceans by deep (> 5 km) seawater-hydrothermal circulation at mid-ocean ridges, J. Geophys. Res.-Sol. Ea., 86, 2737–2755, https://doi.org/10.1029/JB086iB04p02737, 1981.

Hoshino, T., Doi, H., Uramoto, G.-I., Wömer, L., Adhikari, R. R., Xiao, N., Morono, Y., D'Hondt, S., Hinrichs, K.-U., and Inagaki, F.: Global diversity of microbial communities in marine sediment, P. Natl. Acad. Sci. USA, 117, 27587–27597, https://doi.org/10.1073/pnas.1919139117, 2020.

Huber, J. A., Johnson, H. P., Butterfield, D. A., and Baross, J. A.: Microbial life in ridge flank crustal fluids, Environ. Microbiol., 8, 88–99, https://doi.org/10.1111/j.1462-2920.2005.00872.x, 2006.

Ildefonse, B., Abe, N., Blackman, D. K., Pablo Canales, J., Isozaki, Y., Kodaira, S., Myers, G., Nakamura, K., Nedimovic, M., Skinner, A. C., Seama, N., Takazawa, E., Teagle, D. A. H., Tominaga, M., Umino, S., Wilson, D. S., and Yamao, M.: The MoHole: A Crustal Journey and Mantle Quest, Workshop in Kanazawa, Japan, 3–5 June 2010, Sci. Dril., 10, 56–63, https://doi.org/10.2204/iodp.sd.10.07.2010, 2010.

Inagaki, F., Nunoura, T., Nakagawa, S., Teske, A., Lever, M., Lauer, A., Suzuki, M., Takai, K., Delwiche, M., Colwell, F. S., Nealson, K. H., Horikoshi, K., D'Hondt, S., and Jørgensen, B. B.: Biogeographical distribution and diversity of microbes in methane hydrate-bearing deep marine sediments on the Pacific Ocean Margin, P. Natl. Acad. Sci. USA, 103, 2815–2820, https://doi.org/10.1073/pnas.0511033103, 2006.

Inagaki, F., Hinrichs, K.-U., Kubo, Y., Bowles, M. W., Heuer, V. B., Hong, W.-L., Hoshino, T., Ijiri, A., Imachi, H., Ito, M., Kaneko, M., Lever, M. A., Lin, Y.-S., Methé, B. A., Morita, S., Morono, Y., Tanikawa, W., Bihan, M., Bowden, S. A., Elvert, M., Glombitza, C., Gross, D., Harrington, G. J., Hori, T., Li, K., Limmer, D., Liu, C.-H., Murayama, M., Ohkouchi, N., Ono, S., Park, Y.-S., Phillips, S. C., Prieto-Mollar, X., Purkey, M., Riedinger, N., Sanada, Y., Sauvage, J., Snyder, G., Susilawati, R., Takano, Y., Tasumi, E., Terada, T., Tomaru, H., Trembath-Reichert, E., Wang, D. T., and Yamada, Y.: Exploring deep microbial life down to ∼ 2.5 km below the ocean floor, Science, 349, 420–424, https://doi.org/10.1126/science.aaa6882, 2015.

Ivarsson, M., Bengtson, S., and Neubeck, A.: The igneous oceanic crust – Earth's largest fungal habitat?, Fungal Ecol., 20, 249–255, https://doi.org/10.1016/j.funeco.2016.01.009, 2016.

Jørgensen, S. L. and Zhao, R.: Microbial inventory of deeply buried oceanic crust from a young ridge flank, Front. Microbiol., 7, 820, https://doi.org/10.3389/fmicb.2016.00820, 2016.

Kelemen, P. B., Matter, J. M., Teagle, D. A. H., Coggon, J. A., and the Oman Drilling Project Science Team: College Station, TX (International Ocean Discovery Program), Proceedings of the Oman Drilling Project, https://doi.org/10.14379/OmanDP.proc.2020, 2020.

Kendrick, M. A., Hemond, C., Kamenetsky, V. S., Danyushevsky, L., Devey, C. W., Rodemann, T., Jackson, M. G., and Perfit, M. R.: Seawater cycled throughout Earth's mantle in partially serpentinized lithosphere, Nat. Geosci., 10, 222–228, https://doi.org/10.1038/ngeo2902, 2017.

Klein, F., Humphris, S. E., Guo, W., Schubotz, F., Schwarzenbach, E. M., and Orsi W. D.: Fluid mixing and the deep biosphere of a fossil Lost City-type hydrothermal system at the Iberia Margin, P. Natl. Acad. Sci. USA, 112, 12036–12041, https://doi.org/10.1073/pnas.1504674112, 2015.

Klein, F., Grozeva, N. G., and Seewald, J. S.: Abiotic methane synthesis and serpentinization in olivine-hosted fluid inclusions, P. Natl. Acad. Sci. USA, 116, 17666–17672, https://doi.org/10.1073/pnas.1907871116, 2019.

Koppers, A. A. P. and Coggon, R. (Eds): Exploring Earth by Scientific Ocean Drilling: 2050 Science Framework, 124 pp., https://doi.org/10.6075/J0W66J9H, 2020.

Labonté, J. M., Lever, M. A., Edwards, K. J., and Orcutt, B. N.: Influence of igneous basement on deep sediment microbial diversity on the eastern Juan de Fuca ridge flank, Front. Microbiol., 8, 1434, https://doi.org/10.3389/fmicb.2017.01434, 2017.

Laske, G., Markee, A., Orcutt, J. A., Wolfe, C. J., Collins, J. A., Solomon, S. C., Detrick, R. S., Bercovici, D., and Hauri, E. H.: Asymmetric shallow mantle structure beneath the Hawaiian Swell-evidence from Rayleigh waves recorded by the PLUME network, Geophys. J. Int., 187, 1725–1742, https://doi.org/10.1111/j.1365-246X.2011.05238.x, 2011.

Leahy, G. M., Collins, J. A., Wolfe, C. J., Laske, G., and Solomon, S. C.: Underplating of the Hawaiian Swell: evidence from teleseismic receiver functions, Geophys. J. Int., 183, 313–329, https://doi.org/10.1111/j.1365-246X.2010.04720.x, 2010.

Lever, M. A., Rouxel, O. J., Alt, J., Shimizu, N., Ono, S., Coggon, R. M., Shanks III, W. C., Lapham, L., Elvert, M., Prieto-Mollar, X., Hinrichs, K.-U., Inagaki, F., and Teske, A.: Evidence for microbial carbon and sulfur cycling in deeply buried ridge flank basalt, Science, 339, 1305–1308, https://doi.org/10.1126/science.1229240, 2013.

Li, J., Paraskevi, M., Schubotz, F., Sylvan, J. B., Burgaud, G., Klein, F., Beaudoin, D., Wee, S. Y., Dick, H. J. B., Lott, S., Cox, R., Meyer, L. A. E., Quemener, M., Blackman, D. K., and Edgcomb, V. P.: Recycling and metabolic flexibility dictate life in the lower oceanic crust, Nature, 579, 250–255, https://doi.org/10.1038/s41586-020-2075-5, 2020.

Liu, C.-H., Huang, X., Xie, T.-N., Duan, N., Xue, Y.-R., Zhao, T.-X., Lever, M. A., Hinrichs, K.-U., and Inagaki, F.: Exploration of cultivable fungal communities in deep coal-bearing sediments from ∼ 1.3 to 2.5 km below the ocean floor, Environ. Microbiol., 19, 803–818, https://doi.org/10.1111/1462-2920.13653, 2017.

Majumdar, A. S., Ray, D., and Shukla, A. D.: Serpentinization of olivine–gabbro in Central Indian ridge: Insights into H_2 production during alteration in lower oceanic crust and sustenance of life at slow–spreading ridges, Lithos, 374–375, 105730, https://doi.org/10.1016/j.lithos.2020.105730, 2020.

Mason, O. U., Nakagawa, T., Rosner, M., Van Nostrand, J. D., Zhou, J., Maruyama, A., Fisk, M. R., and Giovannoni, S. J.: First investigation of the microbiology of

the deepest layer of ocean crust, PLoS One, 5, e15399, https://doi.org/10.1371/journal.pone.0015399, 2010.

Ménez, B., Pisapia, C., Andreani, M., Jamme, F., Vanbellingen, Q. P., Brunelle, A., Richard, L., Dumas, P., and Réfrégiers, M.: Abiotic synthesis of amino acids in the recesses of the oceanic lithosphere, Nature, 564, 59–63, https://doi.org/10.1038/s41586-018-0684-z, 2018.

Meyer, J. L., Jaekel, U., Tully, B. J., Glazer, B. T., Wheat, C. G., Lin, H.-T., Hsieh, C.-C., Cowen, J. P., Hulme, S. M., Girguis, P. R., and Huber, J. A.: A distinct and active bacterial community in cold oxygenated fluids circulating beneath the western flank of the Mid-Atlantic ridge, Sci. Rep., 6, 22541, https://doi.org/10.1038/srep22541, 2016.

Morishita, T., Umino, S., Kimura, J.-I., Yamashita, M., Ono, S., Michibayashi, K., Tominaga, M., Klein, F., and Garcia, M. O.: Workshop report on hard-rock drilling into mid-Cretaceous Pacific oceanic crust on the Hawaiian North Arch, Sci. Dril., 26, 47–58, https://doi.org/10.5194/sd-26-47-2019, 2019.

Müller, R. D., Sdrolias, M., Gaina, C., and Roest, W. R.: Age, spreading rates, and spreading asymmetry of the world's ocean crust, Geochem. Geophy. Geosy., 9, Q04006, https://doi.org/10.1029/2007GC001743, 2008.

National Research Council: The AMSOC Project to Drill a Hole to the Mohorovicic Discontinuity, Prepared for the AMSOC committee by H. H. Hess, Division of Earth Sciences, Washington, D.C., USA, 5 pp., 1957.

Nigro, O. D., Jungbluth, S. P., Lin, H.-T., Hsieh, C.-C., Miranda, J. A., Schvarcz, C. R., Rappé, M. S., and Steward, G. F.: Viruses in the oceanic basement, mBio, 8, e02129-16, https://doi.org/10.1128/mBio.02129-16, 2017.

Ohira, A., Kodaira, S., Moore, G. F., Yamashita, M., Fujiwara, T., Kaiho, Y., Miura, S., and Fujie, G.: Active-source seismic survey on the northeastern Hawaiian Arch: insights into crustal structure and mantle reflectors, Earth Planets Space, 70, 121, https://doi.org/10.1186/s40623-018-0891-8, 2018.

Orsi, W. D., Edgcomb, V. P., Christman, G. D., and Biddle, J. F.: Gene expression in the deep biosphere, Nature, 499, 205–208, https://doi.org/10.1038/nature12230, 2013.

Phipps Morgan, J. and Chen, Y. J.: The genesis of oceanic crust: magma injection, hydrothermal circulation, and crustal flow, J. Geophys. Res.-Sol. Ea., 98, 6283–6297, https://doi.org/10.1029/92JB02650, 1993.

Quemener, M., Mara, P., Schubotz, F., Beaudoin, D., Li, W., Pachiadaki, M., Sehein, T. R., Sylvan, J. B., Li, J., Barbier, G., Edgcomb, V., and Burgaud, G.: Meta-omics highlights the diversity, activity and adaptations of fungi in deep oceanic crust, Environ. Microbiol., 22, 3950–3967, https://doi.org/10.1111/1462-2920.15181, 2020.

Sano, T., Miyoshi, M., Ingle, S., Banerjee, N. R., Ishimoto, M., and Fukuoka, T.: Boron and chlorine contents of upper oceanic crust: Basement samples from IODP Hole 1256D, Geochem. Geophy. Geosy., 9, Q12O15, https://doi.org/10.1029/2008GC002182, 2008.

Shah-Walter, S. R., Jaekel, U., Osterholz, H., Fisher, A. T., Huber, J. A., Pearson, A., Dittmar, T., and Girguis, P. R.: Microbial decomposition of marine dissolved organic matter in cool oceanic crust, Nat. Geosci., 11, 334–339, https://doi.org/10.1038/s41561-018-0109-5, 2018.

Shor, G. G. and Pollard, D. D.: Mohole site selection studies north of Maui, J. Geophys. Res., 69, 1627–1637, https://doi.org/10.1029/JZ069i008p01627, 1964.

Spinelli, G. A., Giambalvo, E. R., and Fisher, A. F.: Sediment permeability, distribution, and influence on fluxes in oceanic basement, in: Hydrogeology of the Oceanic Lithosphere, edited by: Davis, E. E. and Elderfield, H., Cambridge Univ. Press, New York, USA, 151–188, 2004.

Staudigel, H., Hart, S. R., Schmincke, H.-U., and Smith, B. M.: Cretaceous ocean crust at DSDP sites 417 and 418: carbon uptake from weathering versus loss by magmatic outgassing, Geochim. Cosmochim. Ac., 53, 3091–3094, https://doi.org/10.1016/0016-7037(89)90189-0, 1989.

Stein, C. A. and Stein, S.: Constraints on hydrothermal heat flux through the oceanic lithosphere from global heat flow, J. Geophys. Res.-Sol. Ea., 99, 3081–3095, https://doi.org/10.1029/93JB02222, 1994.

Suzuki, Y., Yamashita, S., Kouduka, M., Ao, Y., Mukai, H., Mitsunobu, S., Kagi, H., D'Hondt, S., Inagaki, F., Morono, Y., Hoshino, T., Tomioka, N., and Ito, M.: Deep microbial proliferation at the basalt interface in aged oceanic crust, Communications Biology, 3, 136, https://doi.org/10.1038/s42003-020-0860-1, 2020.

Teagle, D. and Ildefonse, B.: Journey to the mantle of the Earth, Nature, 471, 437–439, https://doi.org/10.1038/471437a, 2011.

Teagle, D. A. H., Alt, J. C., Umino, S., Miyashita, S., Banerjee, N. R., Wilson, D. S., and the Expedition 309/312 Scientists: Proc. IODP, 309/312, Washington, DC (Integrated Ocean Drilling Program Management International, Inc.), https://doi.org/10.2204/iodp.pr.312.2006, 2006.

Ten Brink, U. S. and Brocher, T. M.: Multichannel seismic evidence for a subcrustal intrusive complex under Oahu and a model for Hawaiian volcanism, J. Geophys. Res., 92, 13687–13707, https://doi.org/10.1029/JB092iB13p13687, 1987.

Ten Brink, U. S. and Brocher, T. M.: Multichannel seismic evidence for variations in crustal thickness across the Molokai Fracture Zone in the Mid-Pacific, J. Geophys. Res., 93, 1119–1130, https://doi.org/10.1029/JB093iB02p01119, 1988.

Thorseth, I. H., Torsvik, T., Furnes, H., and Muehlenbachs, K.: Microbes play an important role in the alteration of oceanic crust, Chem. Geol., 126, 137–146, https://doi.org/10.1016/0009-2541(95)00114-8, 1995.

Tully, B. J., Wheat, C. G., Glazer, B. T., and Huber, J. A.: A dynamic microbial community with high functional redundancy inhabits the cold, oxic subseafloor aquifer, ISME J., 12, 1–16, https://doi.org/10.1038/ismej.2017.187, 2018.

Umino, S., Miyashita, S., Hotta, F., and Adachi, Y.: Along-strike variation of the sheeted dike complex in the Oman Ophiolite: Insights into subaxial ridge segment structures and the magma plumbing system, Geochem. Geophy. Geosy., 4, 8618, https://doi.org/10.1029/2001GC000233, 2003.

Umino, S., Nealson, K., and Wood, B.: Drilling to Earth's mantle, Phys. Today, 66, 36–41, https://doi.org/10.1063/PT.3.2082, 2013.

Vance, D., Teagle, D. A. H., and Foster, G. L.: Variable Quaternary chemical weathering fluxes and imbalances in marine geochemical budgets, Nature, 458, 493–496, https://doi.org/10.1038/?nature07828, 2009.

Watts, A. B. and ten Brink, U. S.: Crustal structure, flexure, and subsidence history of the Hawaiian Islands, J. Geophys. Res.-Sol. Ea., 94, 10473–10500, https://doi.org/10.1029/JB094iB08p10473, 1989.

Watts, A. B., ten Brink, U. S., Buhl, P., and Brocher, T. M.: A Multichannel seismic study of lithospheric flexure across the Hawaiian-Emperor Seamount Chain, Nature, 315, 105–111, https://doi.org/10.1038/315105a0, 1985.

Wolfe, C. J., Solomon, S. C., Laske, G., Collins, J. A., Detrick, R. S., Orcutt, J. A., Bercovici, D., and Hauri, E. H.: Mantle shear-wave velocity structure beneath the Hawaiian hot spot, Science, 326, 1388–1390, https://doi.org/10.1126/science.1180165, 2009.

Zucca, J. J. and Hill, D. P.: Crustal structure of the southeast flank of Kilauea volcano, Hawaii, from seismic refraction measurements, B. Seismol. Soc. Am., 70, 1149–1159, 1980.

Zucca, J. J., Hill, D. P., and Kovach, R. L.: Crustal structure of Mauna Loa volcano, Hawaii, from seismic refraction and gravity data, B. Seismol. Soc. Am., 72, 1535–1550, 1982.

IODP Expedition 386: Japan Trench Paleoseismology

IODP Expedition 386 (Co-chief Scientists: M. Strasser, ECORD-Austria and Ken Ikehara, Japan) aims at reconstructing the Late Pleistocene-Holocene history of giant earthquakes, which are major geological events with catastrophic societal consequences.

This expedition is jointly implemented by the ECORD Science Operator (ESO), and the Institute for Marine-Earth Exploration and Engineering (MarE3) within the Japan Agency for Marine-Earth Science and Technology (JAMSTEC). Expedition 386 is the first IODP expedition since January 2020 and the break in operations due to the pandemic. The offshore phase, conducted with the JAMSTEC-operated research vessel Kaimei, initially planned in spring 2020, has started on 13 April 2021 and should end on 1 June 2021. The Onshore Science Party will be conducted in fall 2021 on board Chikyu docked in Shimizu, as an alternative to the Bremen Core Repository.

This expedition ushers cross collaboration and operational knowledge exchange between IODP operators for the implementation of IODP expeditions. Direct collaboration between two IODP platform providers and the provision of in-kind contributions (IKC) may serve as a model for the implementation of future IODP expeditions, especially MSP expeditions.

https://www.ecord.org/expedition386/

IODP Education and Outreach workshop series

Plans are underway for a series of online workshops focusing on implementation of Enabling Element #1, Broader Impacts and Outreach, as described in the IODP 2050 Science Framework. Organized by USSSP in partnership with the Science Education Resource Center (SERC) and spearheaded by a steering committee of community members and staff, the workshops are planned for Spring/Summer 2021. There will be three two-part online workshops, focused on three sub-topics: Public Engagement (June 22 and 24), Policy (July 19 and 21), and Training the Next Generation (Aug. 2 and 4). Applications for each of these workshops will be available soon on the SERC website at https://serc.carleton.edu/IODP/index. html. Following the on-line workshops, and using the results of the preliminary on-line gatherings, the plan is to hold an in-person workshop in Fall 2021. The results of these workshops will inform a white paper outlining science communication and broader impacts for scientific ocean drilling projects into the future, with a special emphasis on broadening participation and diversity. They will also substantially influence the strategic communications plan developed by USSSP to deliver activities under Enabling Element 1.

For more information, please contact Sharon Cooper: scooper@ldeo.columbia.edu.

Schedules

Due to the Corona pandemic situation, several expeditions and drilling projects are postponed until further notice.

IODP – Expedition schedule http://www.iodp.org/expeditions/

| USIO operations	Platform	Dates	Port of origin
1 Exp 395E: Complete South Atlantic Transect Reentry Installations	JOIDES Resolution	Apr 6–June 6, 2021	Cape Town
2 Exp 386: Japan Trench Paleoseismology	Kaimei & Chikyu	Apr 13–Jun 1, 2021	Yokusuka
3 Exp 395C: Reykjanes Mantle Convection and Climate	JOIDES Resolution	Jun 6–Aug 6, 2021	Reykjavik
4 Exp 396: Mid-Norwegian Continental Margin Magmatism	JOIDES Resolution	Aug 6–Oct 6, 2021	Reykjavik
5 Exp 396T: Hole U1309D Remediation and Engineering Testing	JOIDES Resolution	Oct 6–Dec 6, 2021	Kristiansand

ICDP – Project schedule http://www.icdp-online.org/projects/

ICDP project	Drilling dates	Location
1 Drilling Overdeepened Alpine Valleys (DOVE)	Apr–Jun 2021	Germany, Switzerland
2 A Strainmeter Array Along the Alto Tiberina Fault System (STAR)	Jul 2021	Central Apennines (Italy)
3 Barberton Archean Surface Environments (BASE), Moodies Group	Fall 2021	South Africa
4 Geological Research through Integrated Neoproterozoic Drilling (GRIND)	Fall 2021	Namibia, Brazil
5 Trans-Amazon Drilling Project	Fall 2021	Brazil (multiple locations)

Locations
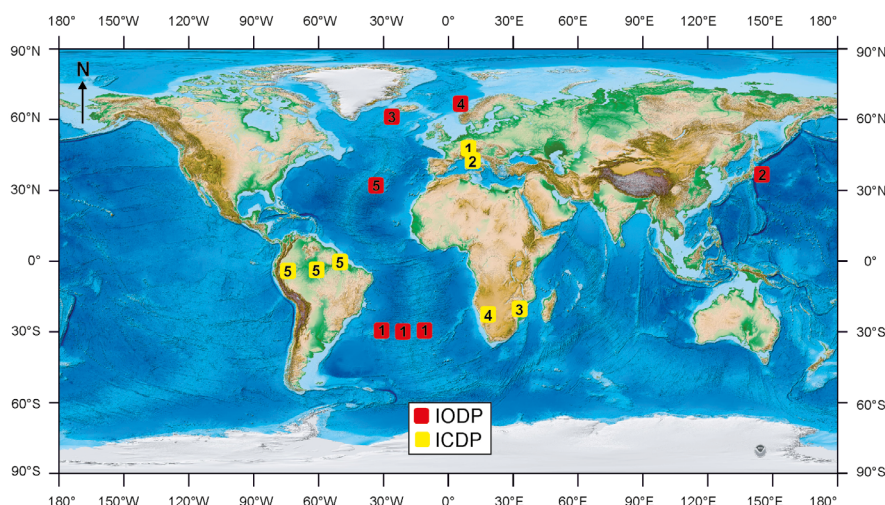
Topographic/bathymetric maps courtesy of NOAA (Amante, C. and B.W. Eakins, 2009. ETOPO1 1 Arc-Minute Global Relief Model: Procedures, Data Sources and Analysis. NOAA Technical Memorandum NESDIS NGDC-24. National Geophysical Data Center, NOAA. doi:10.7289/V5C8276M).